

HADRONIC VECTOR BOSON DECAY AND THE
ART OF CALORIMETER CALIBRATION

by

OLGA LOBBAN, B.S.

A DISSERTATION

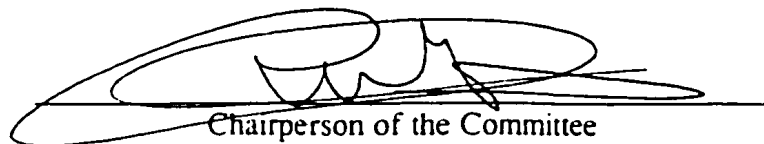
IN

PHYSICS

Submitted to the Graduate Faculty
of Texas Tech University in
Partial Fulfillment of
the Requirements for
the Degree of

DOCTOR OF PHILOSOPHY

Approved



Chairperson of the Committee

Walter L. Borst

V. Papadimitiou

Accepted



Dean of the Graduate School

December, 2002

ACKNOWLEDGEMENTS

My advisor was one of the best I could have chosen anywhere. He always looked out for my interests and made sure that I was not only learning and making progress, but also enjoying my work and having a good time. He is a great physicist, a superb teacher and a joy to work for. Thanks also to his wife for her wonderful cooking, hospitality and movie talk!

When we moved to Fermilab, I never, ever, *ever* thought I would end up liking it so much. I had so much fun here. A big part of that was the group of incredible friends I found here. Kirsten, Sarah, Dan, Sondra, The Dude, Daniel, Kirby, Florencia, Amy, Hung Chung, JJ, Jack and the whole dinner club. All of these people meant more to me than they know.

To my grandparents, Papi and Lita.

To Olene.

To my incredible brother who is the true talent of the family. He has done so much for me, in so many ways. In high school, he drove us to school while I sat in the passenger seat doing my homework. He has always been supportive, inspiring, and a best friend. Thanks, Kid.

To my amazing mom. I don't know if I could ever do what she has done. Knowing that I have some of my mom in me, gives me courage to do anything. She is the smartest and bravest woman I know.

To my amazing dad. He is full of unique ideas, and he has always inspired me and encouraged me to do great things. I am so proud to call him my dad.

To both my parents, who spent so much time, effort and money on me and my brother. Mom and Dad, I promise I'll start playing the piano again.

To my Andy, my best friend. Without my Andy, I would have quit all of this long ago. I am blessed with him, and I thank God for him everyday.

CONTENTS

| | |
|--|-----|
| ACKNOWLEDGEMENTS | ii |
| ABSTRACT | vi |
| LIST OF TABLES | vii |
| LIST OF FIGURES | ix |
| 1. INTRODUCTION | 1 |
| 2. THE STANDARD MODEL | 4 |
| 2.1 Introduction | 4 |
| 2.1.1 Quantum Electrodynamics | 5 |
| 2.1.2 Quantum Chromodynamics | 6 |
| 2.1.3 Electroweak | 7 |
| 3. EXPERIMENTAL APPARATUS | 8 |
| 3.1 The Particle Accelerator | 8 |
| 3.1.1 Protons | 8 |
| 3.1.2 Antiprotons | 11 |
| 3.1.3 Collisions | 12 |
| 3.2 The Particle Detector | 13 |
| 3.2.1 The Tracking System | 14 |
| 3.2.1.1 Silicon Vertex Detector (SVX) | 15 |
| 3.2.1.2 Vertex Tracking Chamber (VTX) | 17 |
| 3.2.1.3 Central Tracking Chamber (CTC) | 19 |
| 3.2.2 Calorimeters | 21 |
| 3.2.2.1 Central and Wall Calorimeters | 21 |
| 3.2.2.2 Plug Calorimeter | 23 |
| 3.2.3 Muon Detector | 24 |
| 3.2.3.1 Central Muon Chambers (CMU) | 24 |
| 3.2.3.2 Central Muon Upgrade (CMP) | 24 |
| 3.2.3.3 Central Muon Extension (CMX) | 25 |
| 4. CALORIMETRY | 26 |
| 4.1 What calorimeters measure | 26 |
| 4.2 Parts of a calorimeter | 26 |
| 4.3 Types of calorimeters | 27 |
| 4.4 Segmentation | 28 |
| 4.5 Electromagnetic (em) showers | 30 |
| 4.5.1 Physical size of em showers | 31 |
| 4.5.2 Resolution of em showers | 31 |
| 4.6 Hadronic showers | 32 |
| 4.6.1 Physical size of hadron showers | 33 |
| 4.6.2 Invisible energy | 33 |

| | | |
|---------|---|----|
| 4.6.3 | Electromagnetic component of hadron showers | 34 |
| 4.6.4 | Compensation and noncompensation (e/h) | 34 |
| 4.6.5 | Consequences of noncompensation | 35 |
| 4.7 | Radiation Damage Issues | 36 |
| 4.7.1 | Radiation damage studies for the CMS very forward calorimeter | 36 |
| 4.7.2 | Radiation exposure | 37 |
| 4.7.3 | Data Analysis | 38 |
| 4.7.4 | A model that reproduces data | 39 |
| 5. | CALIBRATING LONGITUDINALLY SEGMENTED CALORIMETERS | 43 |
| 5.1 | CDF Plug Upgrade Calorimeter | 43 |
| 5.2 | CDF Plug Upgrade testbeam analysis | 43 |
| 5.2.1 | The calibration methods | 44 |
| 5.2.1.1 | Electromagnetic section energy scale | 44 |
| 5.2.1.2 | Hadronic section energy scale—Method I | 45 |
| 5.2.1.3 | Hadronic section energy scale—Method II | 46 |
| 5.2.1.4 | Hadronic section energy scale—Method III | 47 |
| 5.2.2 | Experimental consequences of each method | 49 |
| 5.2.2.1 | Dependence on the starting point of the showers | 49 |
| 5.2.2.2 | Signal nonlinearity | 50 |
| 5.2.3 | Final energy reconstruction | 53 |
| 5.2.4 | Consequences for Jets | 54 |
| 5.2.5 | Conclusions | 55 |
| 5.3 | CDF Central calorimeter studies | 55 |
| 5.3.1 | Run I minimum bias data | 57 |
| 5.3.2 | Background correction | 60 |
| 5.3.3 | Comparison of calibration methods | 63 |
| 5.3.3.1 | Method I | 63 |
| 5.3.4 | Method III | 66 |
| 5.4 | Conclusions | 67 |
| 6. | JETS | 69 |
| 6.1 | Strong coupling constant | 69 |
| 6.2 | Hadronization | 70 |
| 6.3 | What is a jet? | 70 |
| 6.4 | Measuring jets in high energy collisions | 71 |
| 6.4.1 | Conclusions | 73 |
| 7. | SEARCH FOR TWO-JET DECAY OF THE W AND Z BOSONS AT THE FERMILAB TEVATRON | 75 |
| 7.1 | Introduction | 75 |
| 7.2 | UA2 Result | 76 |

| | | |
|-------|--|-----|
| 7.3 | CDF Data | 78 |
| 7.4 | Signal Expectations | 79 |
| 7.5 | Central Calorimeter Jet Corrections | 81 |
| 7.6 | Initial search procedure | 85 |
| 7.7 | Correcting for trigger inefficiencies | 86 |
| 7.8 | Results | 88 |
| 7.8.1 | Signal Properties | 88 |
| 7.8.2 | Cross section and comparison with Standard Model | 90 |
| 7.9 | Conclusions | 92 |
| 8. | SUMMARY AND CONCLUSIONS | 107 |
| | BIBLIOGRAPHY | 109 |
| A. | INTERCALIBRATION OF THE LONGITUDINAL SEGMENTS OF A CALORIMETER SYSTEM (REPRINTED WITH PERMISSION FROM NUCLEAR INSTRUMENTS AND METHODS. A487 (2002) 381) | 112 |
| B. | EFFECTS OF RADIATION AND THEIR CONSEQUENCES FOR THE PERFORMANCE OF THE FORWARD CALORIMETERS IN THE CMS EXPERIMENT (REPRINTED WITH PERMISSION FROM NUCLEAR INSTRUMENTS AND METHODS. B187 (2002) 66) | 126 |
| C. | ON THE ENERGY MEASUREMENT OF HADRON JETS (ACCEPTED FOR PUBLICATION IN NUCLEAR INSTRUMENTS AND METHODS A) | 142 |

ABSTRACT

Presented here are several studies involving the energy measurement of particles using calorimeters. The first study involves the effects of radiation damage on the response of a prototype calorimeter for the Compact Muon Solenoid experiment. We found that the effects of radiation damage on the calorimeter's response are dose dependent and that most of the damage will occur in the first year of running at the Large Hadron Collider. Another study involved the assessment of the Energy Flow Method, an algorithm which combines the information from the calorimeter system is combined with that from the tracking system in an attempt to improve the energy resolution for jet measurements. Using the Energy Flow Method, an improvement of $\sim 30\%$ is found, but this improvement decreases at high energies where the hadronic calorimeter resolution dominates the quality of the jet energy measurements.

Finally, we developed a new method to calibrate a longitudinally segmented calorimeter. This method eliminates problems with the traditional method used for the calorimeters at the Collider Detector at Fermilab. We applied this new method in the search for hadronic decays of the W and Z bosons in a sample of dijet data taken during Tevatron Run IC. A signal of $9873 \pm 3950(\text{sys}) \pm 1130$ events was found when the new calibration method was used. This corresponds to a cross section $\sigma(p\bar{p} \rightarrow W, Z) \cdot B(W, Z \rightarrow \text{jets}) = 35.6 \pm 14.2(\text{sys}) \pm 4.1(\text{stat})$ nb.

LIST OF TABLES

| | | |
|-----|---|----|
| 7.1 | Summary of efficiencies. | 81 |
| 7.2 | Fits to the trigger efficiency curve derived from a χ^2 and likelihood fit to the background region ($m_{jj} = 125 - 300 \text{ GeV}/c^2$) of the raw dijet mass spectrum (no jet energy corrections). Functions involving arctan and tanh (see Equations 7.13, 7.12) are used to fit the trigger efficiency curve, and different numbers of points on the left and right sides of the signal region are included in the fit (to the trigger efficiency curve). All entries in the table correspond to fits (to the trigger efficiency curve) which had reduced χ^2 values less than 1.1. | 89 |
| 7.3 | Fits to the trigger efficiency curve derived from a likelihood fit to the background region ($m_{jj} = 125 - 300 \text{ GeV}/c^2$) of the dijet mass spectrum in which jet energies were corrected using the method described in Section 7.5. A function involving arctan (see Equation 7.13) is used to fit the trigger efficiency curve, and different numbers of points on the left and right sides of the signal region are included in the fit (to the trigger efficiency curve). All entries in the table correspond to fits (to the trigger efficiency curve) which had reduced χ^2 values less than 1.1. | 90 |
| 7.4 | Fits to the trigger efficiency curve derived from a likelihood fit to the background region ($m_{jj} = 125 - 300 \text{ GeV}/c^2$) of the dijet mass spectrum in which jet energies were corrected using the method described in Section 7.5. A function involving tanh (see Equation 7.12) is used to fit the trigger efficiency curve, and different numbers of points on the left and right sides of the signal region are included in the fit (to the trigger efficiency curve). All entries in the table correspond to fits (to the trigger efficiency curve) which had reduced χ^2 values less than 1.1. | 91 |
| 7.5 | Fits to the trigger efficiency curve derived from a χ^2 fit to the background region ($m_{jj} = 125 - 300 \text{ GeV}/c^2$) of the dijet mass spectrum in which jet energies were corrected using the method described in Section 7.5. A function involving arctan (see Equation 7.13) is used to fit the trigger efficiency curve, and different numbers of points on the left and right sides of the signal region are included in the fit (to the trigger efficiency curve). All entries in the table correspond to fits (to the trigger efficiency curve) which had reduced χ^2 values less than 1.1. | 92 |

| | | |
|-----|---|-----|
| 7.6 | Fits to the trigger efficiency curve derived from a χ^2 fit to the background region ($m_{JJ} = 125 - 300 \text{ GeV}/c^2$) of the dijet mass spectrum in which jet energies were corrected using the method described in Section 7.5. A function involving tanh (see Equation 7.12) is used to fit the trigger efficiency curve, and different numbers of points on the left and right sides of the signal region are included in the fit (to the trigger efficiency curve). All entries in the table correspond to fits (to the trigger efficiency curve) which had reduced χ^2 values less than 1.1. | 93 |
| 7.7 | Fits to the trigger efficiency curve derived from a likelihood fit to the background region ($m_{JJ} = 125 - 300 \text{ GeV}/c^2$) of the raw dijet mass spectrum (no jet energy corrections). Functions involving arctan and tanh (see Equations 7.13, 7.12) are used to fit the trigger efficiency curve in a region where no signal is expected . $m_{JJ} = 90 - 110 \text{ GeV}/c^2$. Different numbers of points on the left and right sides of the signal region are included in the fit (to the trigger efficiency curve). All entries in the table correspond to fits (to the trigger efficiency curve) which had reduced χ^2 values less than 1.1. The mean value of the number of events for all fits is consistent with zero. | 94 |
| 7.8 | Fits to the trigger efficiency curve derived from a χ^2 fit to the background region ($m_{JJ} = 125 - 300 \text{ GeV}/c^2$) of the raw dijet mass spectrum (no jet energy corrections). Functions involving arctan and tanh (see Equations 7.13, 7.12) are used to fit the trigger efficiency curve in a region where no signal is expected . $m_{JJ} = 90 - 110 \text{ GeV}/c^2$. Different numbers of points on the left and right sides of the signal region are included in the fit (to the trigger efficiency curve). All entries in the table correspond to fits (to the trigger efficiency curve) which had reduced χ^2 values less than 1.1. The mean value of the number of events for all fits is consistent with zero. | 106 |

LIST OF FIGURES

| | | |
|-----|---|----|
| 3.1 | The Fermilab accelerator complex. From [1]. | 9 |
| 3.2 | A three-dimensional view of the CDF detector. From [1]. | 15 |
| 3.3 | A view of one quadrant of the CDF detector showing the various detector components and the CDF coordinate system. From [1]. | 16 |
| 3.4 | A three-dimensional view of an SVX barrel. From [1]. | 17 |
| 3.5 | SVX ladder. From [1]. | 18 |
| 3.6 | When a charged particle passes through the VTX, the gas is ionized. The freed electrons drift to the sense wires shown. From [1]. | 19 |
| 3.7 | CTC endplate. From [1]. | 20 |
| 3.8 | A 15° ϕ wedge of the Central calorimeter. From [1]. | 22 |
| . | | |
| 4.1 | Orientation of the quartz fiber calorimeter prototype during testbeam studies of the effects of radiation damage. The tower numbering scheme used for these studies is shown. The direction of the beam used to irradiate the module (LIL Beam) and the direction of the beam used to assess the effects of irradiation on the calorimeter's performance (H4 Beam) are shown. | 38 |
| 4.2 | The average signal in Tower 5 recorded in z -scans with electrons entering the detector in the regions $y = 0 - 5$ mm and $y = 20 - 25$ mm, respectively. | 39 |
| 4.3 | Simulated response curves based on Equation 4.4 and the dose profile $D(z)$ accumulated in the y interval 0-5 mm for $n = 0$ and different values of the parameter α . For comparison, the experimental z -response curve for $y = 0 - 5$ mm, conveniently normalized, is shown as well. See text for details. | 41 |
| 4.4 | Simulated response curves based on Equation 4.4 and the dose profile $D(z)$ accumulated in the y interval 0-5 mm for different values of the parameters n and α . For comparison, the experimentally measured curve is shown as well. See text for details. | 42 |
| . | | |
| 5.1 | The Plug Upgrade testbeam module consisted of four 15° sections, each with 20 towers. Wedge 3 was built <i>without</i> an EM section. | 45 |
| 5.2 | The energy scale for the EM calorimeter section, A , as a function of energy. | 46 |
| 5.3 | The energy scale of the hadronic section, B_I , found using Method I as a function of the energy deposited in the hadronic section of the calorimeter by penetrating pions. | 47 |
| 5.4 | The energy scale of the hadronic section, B_{II} , found using Method II as a function of the energy of the incoming electrons. | 48 |
| 5.5 | The reconstructed energy of penetrating (top) and nonpenetrating (bottom) pions when Method I is used to find the value of B | 51 |

| | | |
|------|---|----|
| 5.6 | The reconstructed energy of penetrating (top) and nonpenetrating (bottom) pions when Method III is used to find the value of B | 52 |
| 5.7 | The ratio of the reconstructed energy and the deposited energy as a function of the energy deposited by pions showering in the CDF Plug Upgrade calorimeter. Results are given for the three calibration methods discussed in the text. The curves through the points are fits to the function in Equation 5.2. | 53 |
| 5.8 | The jet energy response of the Plug Upgrade Calorimeter as found using the Monte Carlo program described in the text. The slope of the line fitting the response is larger when Method I is used than when Method III is used. | 56 |
| 5.9 | Ratio of the particle energy reconstructed by the calorimeter, E_{cal} , and the particle momentum measured with the tracking system, p as a function of p for isolated tracks hitting the Central calorimeter in the inner 36% of the target tower face. See text for details. | 59 |
| 5.10 | The quantity $9/8 \cdot \langle E_{neutral}/p \rangle$ is plotted vs the momentum. $E_{neutral}$ is the total energy in the 8 electromagnetic towers surrounding the target tower for tracks which penetrate the electromagnetic section without interacting. This quantity is an estimate for the average energy deposited in the calorimeter by neutral particles accompanying charged particles that produce golden tracks. | 60 |
| 5.11 | $\langle E_{corr}/p \rangle$ vs p for isolated tracks hitting the Central calorimeter in the inner 36% of the target tower face. E_{corr} is defined as $E_{cal} - E_{neutral}$. See text for details. | 62 |
| 5.12 | The energy in the target tower of the electromagnetic section (top) and the energy in the 9 hadronic towers behind the target tower (bottom). Shown are particles with momenta between 5 and 15 GeV/c. Penetrating particles are defined as those for which the energy in the target electromagnetic tower is between 0.2-0.5 GeV and the energy in the 9 hadronic towers is greater than 1.0 GeV. Nonpenetrating particles are those for which the energy in the target electromagnetic tower is greater than 0.7 GeV. | 63 |
| 5.13 | E_{corr}/p for penetrating and nonpenetrating pions when Method I is used. Shown are particles with momenta between 5 and 15 GeV/c. The means of the distributions differ by $\sim 12\%$. Note that most tracks are in the nonpenetrating category. | 65 |
| 5.14 | The factor, $\langle k \rangle$, that the hadronic section energy must be multiplied by in order to equalize E_{corr}/p for penetrating and nonpenetrating pions. $\langle k \rangle$ is constant over p | 66 |

| | | |
|------|--|-----|
| 5.15 | E_{corr}/p for penetrating and nonpenetrating pions when Method III is used. The plot only includes particles with momenta between 5 and 15 GeV/c. The means of the distributions are not significantly different given the statistical uncertainties. | 67 |
| 6.1 | Relative improvement of the jet resolution by using the Energy Flow Method, as a function of the jet energy. Results of Monte Carlo simulations with different parameter choices. The black diamonds were obtained using testbeam data from the CDF Plug Upgrade calorimeter. See text for details. . . . | 73 |
| 7.1 | The signal $W, Z \rightarrow jets$ seen by UA2. The signal shown consists of 5618 ± 1334 | 78 |
| 7.2 | Central calorimeter signal distributions obtained using isolated tracks from Run IB minimum bias data. Signal distributions are shown separately for the electromagnetic and hadronic sections for tracks with momenta in the 0-1 GeV/c range and 1-2 GeV/c range. See text for details. | 83 |
| 7.3 | Signal distributions for the central electromagnetic calorimeter and the central hadronic calorimeter. Distributions were obtained from isolated tracks in Run IB minimum bias data and are shown for hadrons with $p = 2 - 3$ GeV/c and $p = 3 - 4$ GeV/c. See text for details. | 95 |
| 7.4 | Central electromagnetic and hadronic calorimeter signal distributions obtained from isolated tracks in Run IB minimum bias data with $p = 4 - 5$ GeV and $p > 5$ GeV/c. See text for details. | 96 |
| 7.5 | Jet signal distributions which result from simulations described in text. Here, Method III was used to set the energy scale of the central hadronic calorimeter. Distributions are shown for jet energies ranging from 10-60 GeV. | 97 |
| 7.6 | Jet response curves for CDF's traditional method of determining the energy scale of the hadronic calorimeter section (Method I) and a new method of setting the hadronic section energy scale (Method III). The response is normalized to that of electrons. The inverse of the response represents the correction factor for the absolute jet energy scale (see Equation 7.10). . . . | 98 |
| 7.7 | Raw dijet invariant mass spectrum. No energy corrections have been applied. The two jets were required to be back-to-back ($\cos \Phi < -0.4$) and events in which a third jet with $E_T > 15$ GeV was present were rejected. The steep falloff below 50 GeV/c ² is a result of trigger inefficiencies. . . . | 99 |
| 7.8 | Quality of exponential fits to the dijet invariant mass spectrum over a limited mass range. Shown is the χ^2 (for 23 degrees of freedom) as a function of the lowest mass point of the 45 GeV/c ² wide dijet mass region. See text for details. | 100 |

| | | |
|------|---|-----|
| 7.9 | Residuals when an exponential background is subtracted from the raw dijet mass spectrum (a) and from the dijet mass spectrum in which jets are corrected using Method III (b). The fit shown is the sum of two Gaussian distributions in which the difference between the two means and the ratio of the widths of the two gaussians were fixed, but all other parameters were left free. See text for details. | 101 |
| 7.10 | Raw dijet mass spectrum. Shown is a fit to the spectrum in the range 125-300 GeV/c ² . The fit is extrapolated to lower values of dijet mass in order to extract a trigger efficiency vs dijet mass curve. See text for details. . . | 102 |
| 7.11 | Trigger efficiency curve resulting from dividing the original dijet data (raw) by the extrapolated fit to the background region 125-300 GeV/c ² . Shown is a fit to the data with the function arctan. See text for details. | 103 |
| 7.12 | Resulting signal when the original data (raw) is divided by a fit to the trigger efficiency curve shown in Figure 7.11. | 104 |
| 7.13 | Resulting signal when the "Method III dijet mass spectrum" is divided by a fit to the trigger efficiency curve. | 105 |

CHAPTER 1

INTRODUCTION

Particle physics involves the study of the most fundamental constituents of matter and the interactions between them. A brief review of the Standard Model of particles and interactions is given in Chapter 2. Experimentalists in particle physics use huge particle accelerators to speed particles up to very high energies (TeV¹) and then force them to collide. Using large particle detectors, they then measure various properties of the resulting particle debris. Chapter 3 describes the particle accelerator and one of the particle detectors (Collider Detector at Fermilab) used at the Fermi National Accelerator Laboratory (Fermilab).

The particle detectors used at particle accelerators are multipurpose detectors with many thousands of electronic channels. In this thesis, we concentrate on one subsystem of such multipurpose detectors, namely the calorimeters. Calorimeters measure the energy of charged and neutral particles. The basic workings of calorimeters are described in Chapter 4. Several studies involving calorimeters were performed. Two of these studies were independent, self-contained analyses, and the third study led directly to an analysis of a sample of data taken with the Collider Detector at Fermilab (CDF).

The first self-contained analysis involved a study of radiation damage in a prototype built for the Very Forward Calorimeter of the Compact Muon Solenoid (CMS) detector at the future proton-proton collider, the Large Hadron Collider (LHC). In this study, the prototype was irradiated with particles of the type responsible for very large radiation doses which are expected to accumulate in the forward calorimeters during proton-proton collisions at the LHC. After the irradiation, the performance

¹1 TeV = 10¹²eV; 1 eV = 10⁻¹⁹ joule

of the calorimeter was tested and a model was developed to describe the effects of radiation damage. This work is described in detail in Section 4.7 and Appendix A.

The second study involved the evaluation of an algorithm used to define the energy of a jet, sprays of particles resulting from the breakup of a hadron (such as a proton). Claims have recently been made in the literature that the use of this algorithm along with a highly segmented calorimeter would result in fantastic improvements in the energy measurements of jets. We have performed simulations which show that the improvement is of the order of 30%, but that segmentation does not play a role in the improvement. At higher jet energies, the improvement provided by the algorithm decreases, and the energy resolution of the calorimeter for hadrons becomes the dominant factor in the energy measurement of jets. This work is described in detail in Section 6.4 and Appendix C.

The study which led to an analysis of CDF data involved the calibration of a calorimeter which is segmented into two parts along the direction of incoming particles, an electromagnetic section and a hadronic section (segmentation is discussed in Section 4.4). When a calorimeter is segmented in this way and when it is noncompensating (the signal resulting from a 50 GeV charged pion is smaller than that from a 50 GeV electron; see Section 4.6.4), calibrating the detector is nontrivial. We developed a new method to calibrate such a calorimeter, and this method eliminates problems with previously used methods. This study is described in detail in Chapter 5 and Appendix B. We applied this new method to a sample of data taken with the CDF detector, namely a sample of ~ 3 million events with two jets in the event. In this sample of data, we looked for two-jet decays of the W and Z bosons (mediators of the weak force; see Chapter 2) in the dijet invariant mass spectrum. Using this data sample, events of this type cannot be found on an event-by-event basis, since they produce a signal in the detector (two jets) very similar to that produced by the large background from parton-parton scattering. These events can be found, however, in a

statistical manner since the background (parton-parton scattering) is a smooth function of the dijet invariant mass. When the new calibration method for the calorimeter was used, $9873 \pm 3950(\text{sys}) \pm 1130(\text{stat})$ two-jet decays of the W and Z were found. This analysis is described in detail in Chapter 7. This signal is an important check of the calibration of the jet energy at CDF. The uncertainty on the jet energy is important for many measurements at CDF, e.g., the top quark mass measurement.

CHAPTER 2

THE STANDARD MODEL

"It should be possible to explain the laws of physics to a barmaid." -Albert Einstein

2.1 Introduction

The currently accepted theory of the fundamental constituents of matter and how they interact is called the Standard Model of Particles and Interactions. In the Standard Model, there are four forces, the electromagnetic force, the strong force, the weak force, and gravity.¹ The fundamental particles are divided into three categories, leptons, quarks, and gauge bosons. Leptons feel only the electromagnetic, weak and gravitational forces. Quarks feel all forces. Gauge bosons carry the forces and are referred to as mediators of the forces.

There are six leptons. The electron (e), muon (μ) and tau (τ) are leptons which carry electric charge of -1 . The electron (ν_e), muon (ν_μ) and tau (ν_τ) neutrinos have zero electric charge. The most recent experimental evidence suggests that the mass of neutrinos, while small, is not zero.

There are six types of quarks, up (u), down (d), charm (c), strange (s), bottom (b), and top (t). They each carry $|1/3|$ electric charge. They also carry a color charge (the charge of the strong interaction) of red, green or blue.

The gauge bosons are the carriers of the four forces. The electromagnetic force is mediated by the massless photon, the strong force by the massless gluon, and the weak force by the massive W^\pm and Z^0 particles.

Leptons and quarks are fermions since they carry half integer spin and obey Fermi-Dirac statistics. Gauge bosons are called bosons because they have integral spin and

¹Gravity has not been successfully incorporated into the Standard Model.

obey Bose-Einstein statistics.

Each fermion in the standard model has an antiparticle which is identical to its particle in terms of mass and spin, but has opposite values for other properties such as electric charge or color.

The Standard Model uses gauge theories to mathematically describe how forces interact with fundamental particles. Gauge theories are quantum field theories in which an invariance principle requires the existence of interactions among the particles. The gauge theory of electromagnetism, which uses the $U(1)$ group, is called Quantum Electrodynamics (QED). The gauge theory for the strong force, which uses the $SU(3)$ group, is called Quantum Chromodynamics (QCD) and is modeled after QED. The weak interaction uses the $SU(2)$ group. The gauge theories of the electromagnetic and weak forces have been unified ($U(1) \otimes SU(2)$) into a single gauge theory called the Electroweak theory.

2.1.1 Quantum Electrodynamics

Quantum Electrodynamics connects quantum mechanics to the classical principles of electricity and magnetism. In QED, the force between two charged particles results from the exchange of a field quantum, the photon.

The strength of the electromagnetic interaction is given by the electromagnetic coupling constant α , given by

$$\alpha = \frac{e^2}{4\pi} \quad (2.1)$$

where e is the electromagnetic charge and α is the fine structure constant. QED processes are calculated using a perturbative expansion in α . The lowest order process (terms in the perturbation expansion which are linear in α), called a tree level process, is simple to calculate, but higher-order processes (terms in the perturbation expansion that are quadratic or higher in α) involve divergent (i.e., infinite) momentum integrals.

A redefinition or renormalization of the electric charge as

$$e_R^2(Q^2) \rightarrow \frac{e^2}{1 - C e^2 \ln \frac{Q^2}{-M^2}} \quad (2.2)$$

where Q is square root of the momentum transfer and M is mass removes these infinities. The Q^2 dependence of the strength of the interaction means that at higher energy scales, the strength of the electromagnetic interaction increases. The value of the fine structure constant is often quoted as $1/137$, but this is only the value at atomic energy scales. At energy scales equivalent to the mass energy of the Z gauge boson, the value of α is $1/128$. This is termed the “running” of the coupling constant and is physically interpreted as a screening of the electric charge by virtual e^-e^- pairs in the vacuum.

2.1.2 Quantum Chromodynamics

QCD is the formal theory of the strong interaction between quarks which is based on the $SU(3)$ symmetry group. There are 8 massless gauge bosons, called gluons, which result from imposing local gauge invariance. Gluons carry a quantum called *color charge* or simply *color*. Only quarks and gluons have color charge, so the strong force acts only on them. Quarks carry a color charge (red, green, or blue) and antiquarks carry a corresponding anticolor charge (antired, antigreen, antiblue). They are held together by the exchange of gluons, which carry one color charge and one anticolor charge. QCD is a gauge invariant field theory, just like QED, but unlike QED, it is *non-Abelian*, meaning the generators of the $SU(3)$ group do not commute. This physically means that the gluons carry color charge and can interact with other gluons. This is in sharp contrast to QED (the $U(1)$ group is abelian), where the photon is electrically neutral and does not interact with itself, only with particles which carry electric charge. This has interesting consequences which are discussed in further detail in Section 6.1.

2.1.3 Electroweak

The electromagnetic and weak interactions were unified in the 1960s by Glashow, Salam and Weinberg into a single gauge theory called the Electroweak theory. The $SU(2) \times U(1)$ gauge theory formulated by Glashow involved four massless vector bosons, two of which are charged, but no massless, charged field-mediating particles had ever been observed. In 1967, Salam and Weinberg applied the Higgs mechanism to Glashow's theory, which through spontaneous symmetry-breaking gives three of the four gauge bosons mass. The masses of the electroweak gauge bosons, the W^\pm and Z^0 were predicted by the theory and were discovered in 1983 at the CERN $p\bar{p}$ collider. The Higgs mechanism requires the presence of one more boson, the Higgs boson. The mass of the Higgs boson is a free parameter and can only be determined experimentally. The Higgs boson still eludes experimentalists and is one of the most important outstanding issues in particle physics today.

CHAPTER 3

EXPERIMENTAL APPARATUS

We briefly describe the particle accelerator and the particle detector used to take the data used in the analysis described in Chapter 7. These data were taken during a period of accelerator operation coined "Run I" which lasted from 1985-1996. Currently, "Run II" is underway in which many improvements were made both to the accelerator and the detector. One of the detector improvements is discussed in Sections 5.1 and 5.2.

3.1 The Particle Accelerator

The particle accelerator which provided the proton-antiproton collisions for the analysis described in Chapter 7 is located at Fermi National Accelerator Laboratory in Batavia, Illinois. The accelerator complex, which consists of several different accelerators connected in sequence, is shown in Figure 3.1. For protons, the acceleration sequence is: (1) Cockcroft-Walton, (2) Linac, (3) Booster, (4) Main Ring, (5) Tevatron. For antiprotons, the sequence is: (1) Debuncher, (2) Accumulator, (3) Main Ring, (4) Tevatron.

At the end of the accelerator chain, protons and antiprotons are moving at almost the speed of light in a circular orbit inside a stainless steel pipe at vacuum. Here, we briefly follow (in Section 3.1.1) the chain of acceleration for protons and antiprotons (in Section 3.1.2). Details of the acceleration process can be found in [2].

3.1.1 Protons

The chain of proton acceleration goes as follows:

- Hot hydrogen gas (from an ordinary bottle of hydrogen gas) is passed through a device which extracts negative hydrogen ions and accelerates them to 18 keV.

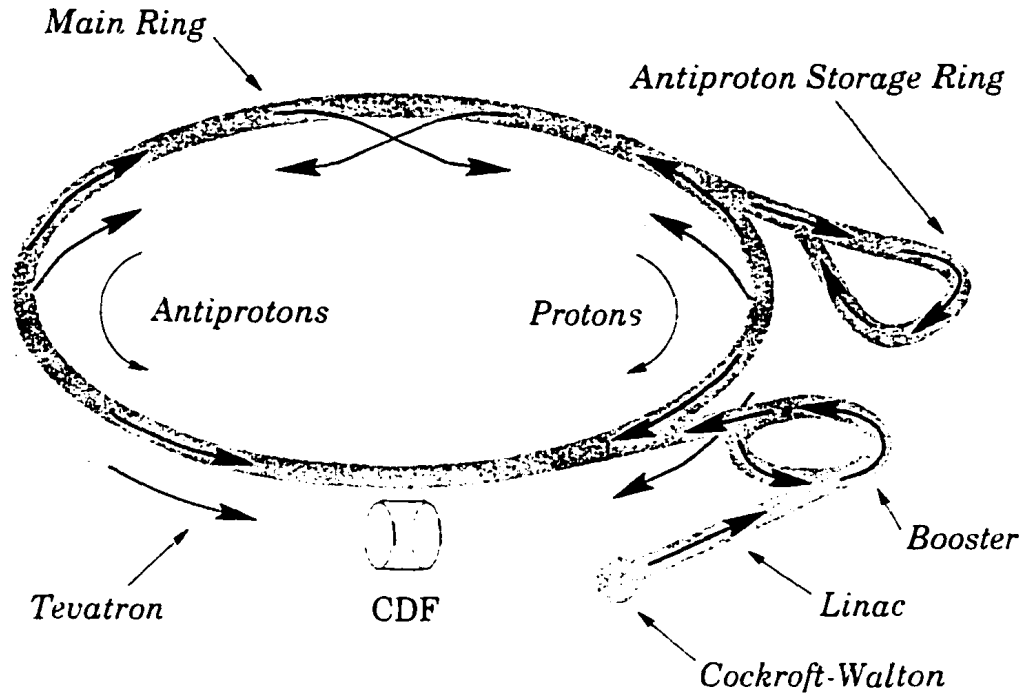


Figure 3.1: The Fermilab accelerator complex. From [1].

- The hydrogen ions are injected into a **Cockcroft-Walton** electrostatic accelerator, where a potential difference accelerates the negative ions to 750 keV.
- The ions are transported to a 145 meter long linear accelerator (**Linac**). The Linac accelerates the ions via 12 radio frequency (RF) cavities to an energy of 401.5 MeV.
- The hydrogen ions are injected into the next accelerating stage, the **Booster**, via *charge exchange injection*. Both the ion beam and the beam of already circulating protons in the Booster are passed through a *dogleg* (two adjacent dipole magnets of opposite polarity) in order to merge the ion beam with the proton beam. The combined beam is then sent through a carbon foil which strips most H^- ions of their two electrons. The beam is sent through another dogleg which steers any remaining H^- ions into a beam dump and restores

the path of the protons in the Booster. The Booster is a proton synchrotron with a radius of 75.5 meters. The protons in the Booster are kept in a stable circular orbit using 96 combined-function dipole/quadrupole magnets. After $\sim 3 \cdot 10^{12}$ protons are transferred from the Linac to the Booster, 17 RF cavities are used to accelerate the protons. In the Booster, protons collect in *buckets*, stable acceleration regions, and form *bunches* of protons. After about 20,000 revolutions around the Booster ring, the proton bunches have been accelerated to 8 GeV.

- The **Main Ring**, a proton synchrotron with a 1 kilometer radius, is the next accelerating stage. It consists of 18 RF cavities, 774 dipole magnets and 240 quadrupole magnets. When enough antiprotons have been stored in the Accumulator (see Section 3.1.2), fifteen proton bunches are taken from the Booster, injected into the Main Ring, accelerated to 150 GeV and coalesced into a single bunch consisting of $\sim 15 \cdot 10^{10}$ protons.
- The single coalesced proton bunch is finally injected into the **Tevatron**, which sits in the same tunnel 65 cm below the Main Ring. The Tevatron uses 774 dipole and 216 quadrupole magnets to keep the protons (and antiprotons, see Section 3.1.2) in a stable circular orbit. Unlike the magnets in the accelerators up to this point, the Tevatron magnets are superconducting magnets, cooled with liquid helium. Six bunches of protons are injected into the Tevatron as described above and (after six bunches of antiprotons have also been injected) accelerated to their final energy of 900 GeV.

The entire process described above takes about 1 minute.

3.1.2 Antiprotons

Antiprotons are not present in ordinary matter. We cannot take a bottle of anti-hydrogen gas, strip the anti-electrons off the anti-hydrogen atoms in the gas and find ourselves with antiprotons. In the elements around us, there are simply no sources of antimatter. So, we have to make antiprotons and then accelerate them. This process is much slower than collecting and accelerating protons.

- Antiprotons are made by extracting protons with an energy of 120 GeV from the Main Ring and directing them at a Nickel target. In the nuclear reactions that take place when the protons hit the target, a spray of secondary particles, including antiprotons, are produced. About 1 antiproton is produced for every 10^5 protons that hit the target. Antiprotons are focused into a beam using a cylindrical lithium lens. A pulsed magnet is then used to deflect negatively charged 8 GeV particles into a transport line to the Debuncher.
- The **Debuncher** does exactly what its name implies. Since the antiprotons were created with bunches of protons, they too arrive in the Debuncher with a narrow spread in time, i.e., bunched. The Debuncher increases the time spread. It also uses *stochastic cooling* to decrease the phase space of the beam.
- The antiprotons are then transferred to the **Accumulator**, a storage ring which stores antiprotons until enough have been collected to inject into the Main Ring. As antiprotons are accumulated (a process known as “stacking”), stochastic cooling is used to decrease the *emittance* of the beam. Antiprotons are accumulated at a rate of about $5 \cdot 10^{10}$ antiprotons per hour.
- After about 8 hours, the “stack” of antiprotons is sufficiently large to be reverse injected into the **Main Ring** for acceleration. After six bunches of protons have already been injected into the Tevatron, a portion of the antiproton stack

from the Accumulator is injected into the Main Ring. As with protons, the antiprotons are accelerated to 150 GeV and coalesced into a single bunch. A typical bunch consists of $5.5 \cdot 10^{10}$ antiprotons.

- One by one, six antiproton bunches are injected into the **Tevatron** moving in the opposite direction relative to the protons. This process uses about half of the antiproton stack in the Accumulator.

3.1.3 Collisions

Once all six proton and six antiproton bunches are countercirculating in the Tevatron, they are accelerated to 900 GeV. Both the proton and antiprotons circulate in the same beampipe and their orbits are spatially separated by $\sim 3\text{-}6$ mm. When the beam energies reach 900 GeV, special quadrupole magnets installed in the CDF (see Section 3.2) and D0 experimental halls are used to force the two beams to “collide” at the center of the detectors. Collisions occur every $3.5\mu\text{s}$. The collisions do not occur at the same point in space from collision to collision. Rather, the *luminous region* is a gaussian distribution about the nominal interaction point with a width of 30 cm in the longitudinal direction (along the beam axis) and $35\mu\text{m}$ in the transverse direction (perpendicular to the beam axis). Typically there is only ~ 1 interaction per bunch crossing, i.e., every time a proton and antiproton bunch are forced to collide by the special quadrupole magnets, only one proton from the proton bunch and one antiproton from the antiproton bunch actually experience a strong interaction with each other.

A given six proton and antiproton bunches continue cycling in the Tevatron for 8-18 hours (called a *store*). The instantaneous luminosity, defined as

$$L = \frac{N_p N_{\bar{p}} B f_0}{4\pi\sigma^2} \quad (3.1)$$

where N_p and $N_{\bar{p}}$ are the number of protons and antiprotons per bunch respectively. B is the number of bunches of each type. f_0 is the revolution frequency of the bunches, and σ^2 is the cross-sectional area of a bunch, decreases exponentially during the store. During a store, the accelerator chain below the Tevatron remains active, so that after the beam from a given store is dumped, fresh bunches are ready to be injected into the Tevatron.

3.2 The Particle Detector

One of the two particle detectors used to observe the proton-antiproton collisions at Fermilab is called the Collider Detector at Fermilab (CDF). It is a multipurpose detector that weighs 5,000 tons and is approximately a 10 meter high, 27 meter long cylinder. When an inelastic interaction between a proton and antiproton takes place, the proton and antiproton are broken up, and different kinds of particles emerge from the interaction point. The CDF detector cylindrically surrounds the beamline, so that particles emerging from the interaction point with some momentum component perpendicular to the beamline will encounter the CDF detector and produce signals in its various subsystems. These signals are electronically measured and used to reconstruct quantities such as the energy, momentum, identity and trajectory of the particles.

The CDF detector is cylindrically symmetric about the beamline and forward-backward symmetric about the interaction point. The coordinate system used by CDF is centered on the nominal interaction point. The positive z -axis points along the beamline in the direction of the protons (east, towards Chicago), the positive y -axis points vertically upwards (towards the sky), and the positive x -axis points radially outwards in the horizontal plane of the Tevatron. The polar angle (θ) is measured with respect to the positive z -axis. Typically, locations of particles in the

detector are identified by the Lorentz-invariant quantity pseudorapidity, η , defined as

$$\eta = -\log(\tan(\theta/2)) \quad (3.2)$$

and by the azimuthal angle (ϕ) which is measured counterclockwise from the positive x -axis. A three-dimensional view of the CDF detector is shown in Figure 3.2. A view of one quadrant of the detector is shown in Figure 3.3. The detector's subsystems can be classified into three main categories:

- Tracking system.
- Calorimeters.
- Muon detectors.

Here, we briefly describe these detector systems as they existed in Run I. A more complete description of the CDF detector can be found in [3]. The detector was modified for Run II which is currently underway. The modifications to the Plug calorimeter are discussed in some detail Section 5.1.

3.2.1 The Tracking System

The tracking system is composed of three different detectors. Surrounding the beampipe is a silicon strip detector, the SVX (Silicon Vertex Detector). Surrounding the SVX is a time projection chamber called the VTX (Vertex Tracking Chamber), and surrounding the VTX is a gas drift chamber, the CTC (Central Tracking Chamber). The silicon detector provides the most precise tracking information, the time projection detector provides information about the z position of an event's interaction point, and the gas drift chamber is used to reconstruct three-dimensional tracks from particles traversing the detector. All of these detectors are surrounded by a superconducting solenoid which provides an axial magnetic field of 1.41 Tesla. From

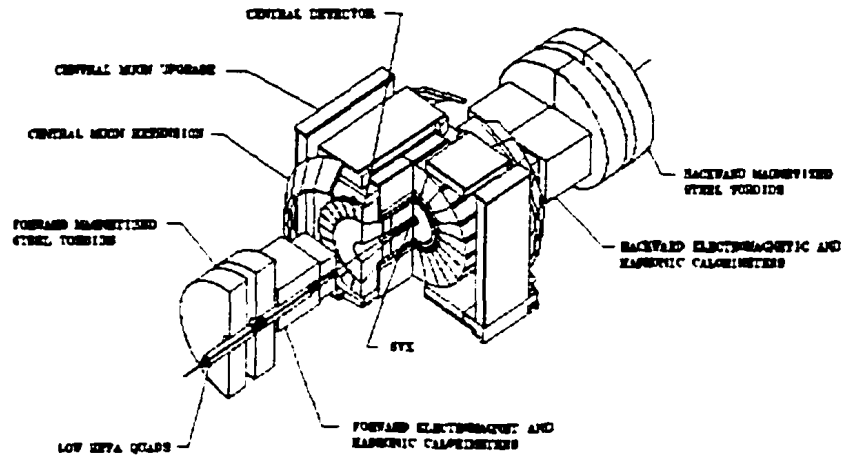


Figure 3.2: A three-dimensional view of the CDF detector. From [1].

the curvature of charged particle tracks in the tracking volume, the momentum of the particles can be measured. The momentum p is given by

$$p = qB\rho \quad (3.3)$$

where q is the charge of the particle, B is the magnetic field strength, and ρ is the radius of curvature of the particle's trajectory.

3.2.1.1 Silicon Vertex Detector (SVX)

The Silicon Vertex Detector used by CDF during its first running period (Run 1A), was the first silicon vertex detector ever used at a hadron collider. A detailed description of the detector's construction and performance can be found in [4].

The detector consists of two cylindrical barrels (side-by-side along z) which coaxially surround the beampipe. A three-dimensional view of one of the barrels is shown

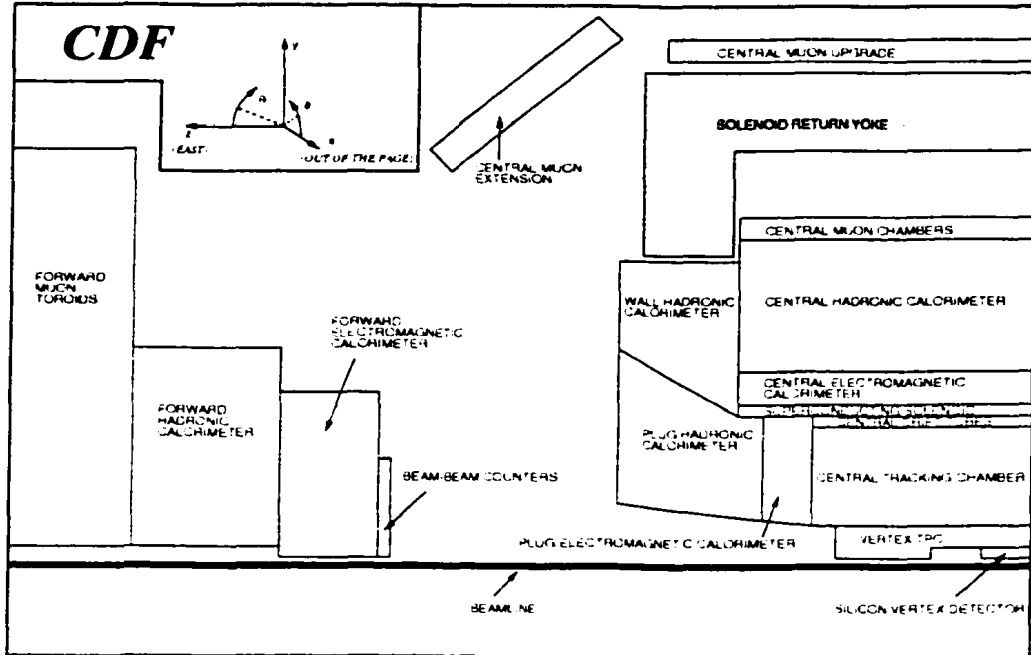


Figure 3.3: A view of one quadrant of the CDF detector showing the various detector components and the CDF coordinate system. From [1].

in Figure 3.4. Each barrel is 25.5 cm long (along z) with a 2.15 cm separation between the two barrels at $z = 0$, making the total active length of the detector 51 cm. Since the interaction region has a spread of $\sigma \sim 30$ cm about $z = 0$, the SVX track acceptance is only $\sim 60\%$. The pseudorapidity coverage is $|\eta| < 1.9$.

Each barrel is divided into 12 azimuthal sections (*wedges*) each subtending 30° . Each wedge consists of four layers of silicon strip detector modules (*ladders*) with the innermost layer at a radius of 2.86 cm and the outermost layer at a radius of 7.87 cm. The ladders (see Figure 3.5) consist of three 8.5 cm long single-sided silicon strip detectors with readout strips running parallel to the beam. On the inner three layers of ladders, the readout strips have a pitch of $60 \mu\text{m}$ whereas the outermost layer's ladders have strips of $55 \mu\text{m}$ pitch.

The detector has a total of 96 ladders and a total of 46,080 channels. Only channels which register a hit are read out. For a typical event, about 5% of the total SVX channels are read out. The readout time for the SVX detector is one of the longest

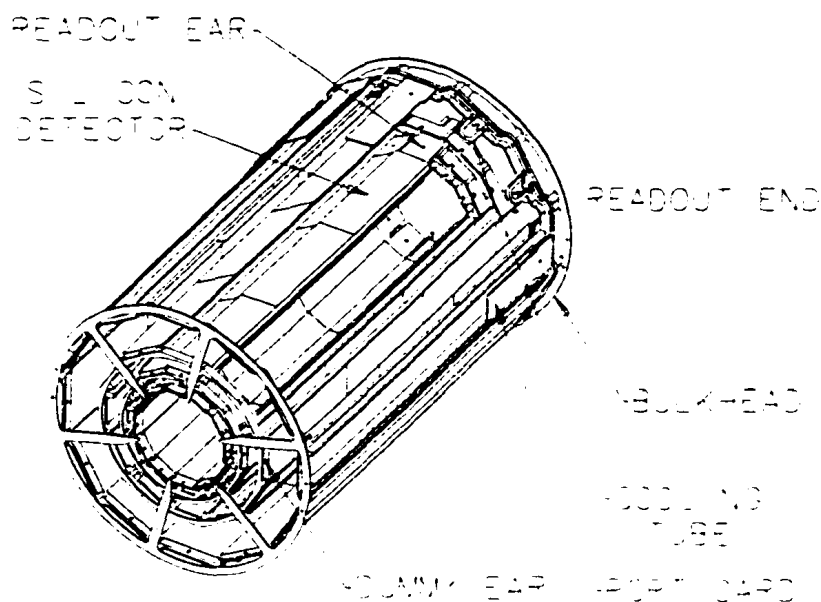


Figure 3.4: A three-dimensional view of an SVX barrel. From [1].

readout times in the CDF detector, typically 2 ms. The SVX provides precise r - ϕ information for the reconstruction of charged particle tracks. The single hit resolution per layer is about $13\mu\text{m}$ with a 96% hit efficiency per layer. The resolution allows the measurement of the secondary vertex of B hadrons which travel distances of $c\tau \sim 300\text{-}400\ \mu\text{m}$ before decaying.

3.2.1.2 Vertex Tracking Chamber (VTX)

The Vertex Tracking Chamber is a gas drift chamber of the TPC (time projection chamber) type which surrounds the SVX. It provides precise tracking information in the $r - z$ plane. This enables the determination of the location along the beamline of the primary $p\bar{p}$ interaction. Also, if there is more than one interaction in the same bunch crossing, the VTX can identify multiple primary vertices and associate a track

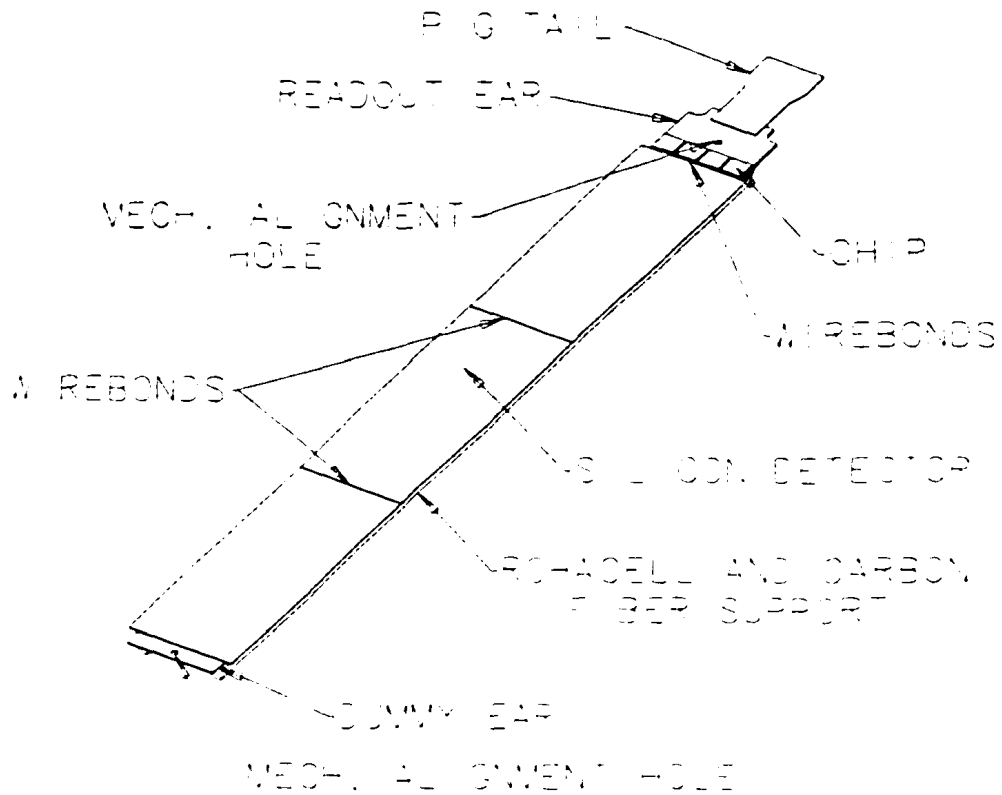


Figure 3.5: SVX ladder. From [1].

to its correct vertex along the beamline.

The VTX consists of 28 separate TPC modules stacked end-to-end along the beam direction. Each module is divided into two 15 cm long drift regions. At the end of the drift regions, proportional chambers are arranged in octants. Each octant has alternating sense wires and field shaping wires strung perpendicular to the radial direction. The detector is 2.8 m long in z with an inner radius of 8 cm and an outer radius of 22 cm. It covers a pseudorapidity range of $|\eta| < 3.5$. The tracking chambers use a 50%-50% mixture of ethane and argon gas. When charged particles pass through the gas, they ionize the gas, and the freed electrons drift (with a velocity of $46\mu\text{m}/\text{ns}$) in the axial direction to the sense wires. The voltage drop on the wire is read out and amplified. The position of the wire provides radial information about the particles traversing the detector and the drift time provides longitudinal information,

so that the track position in the r - z plane can be determined. Using this information from multiple tracks, the primary vertex is located. The location of the primary $p\bar{p}$ interaction vertex is determined with 1 mm uncertainty in z . A cartoon of a charged particle passing through the VTX is shown in Figure 3.6

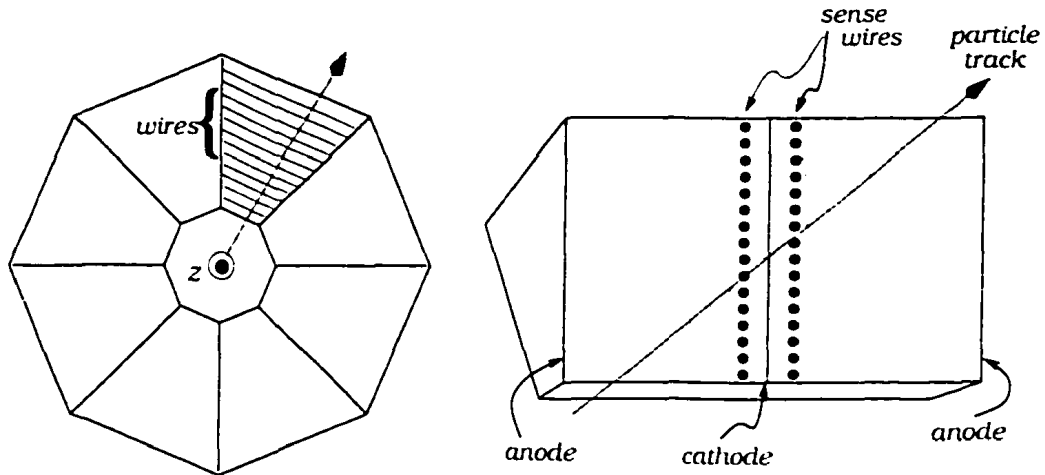


Figure 3.6: When a charged particle passes through the VTX, the gas is ionized. The freed electrons drift to the sense wires shown. From [1].

3.2.1.3 Central Tracking Chamber (CTC)

The Central Tracking Chamber is a large cylindrical drift chamber that surrounds the VTX. It is 3.2 m long (along z) and has an inner radius of 0.3 m and an outer radius of 1.38 m. It provides full 3-D track reconstruction in the pseudorapidity range $|\eta| < 1.1$.

The CTC consists of 84 layers of $40\ \mu\text{m}$ gold-plated tungsten wires running the length of the chamber. They are grouped into nine “super-layers.” There are five *axial* superlayers in which the wires run parallel to the beam and four *stereo* superlayers in which the wires are offset by $\pm 3^\circ$ from the beamline. In the axial superlayers, there are 12 wires per layer whereas in the stereo superlayers there are 6 wires per layer. Combining tracking information provided by the axial superlayers, which measure tracks in the r - z plane, and the stereo superlayers, which measure tracks in the r - ϕ

plane, gives full 3-D track reconstruction. A schematic drawing of a CTC endplate is shown in Figure 3.7. 5

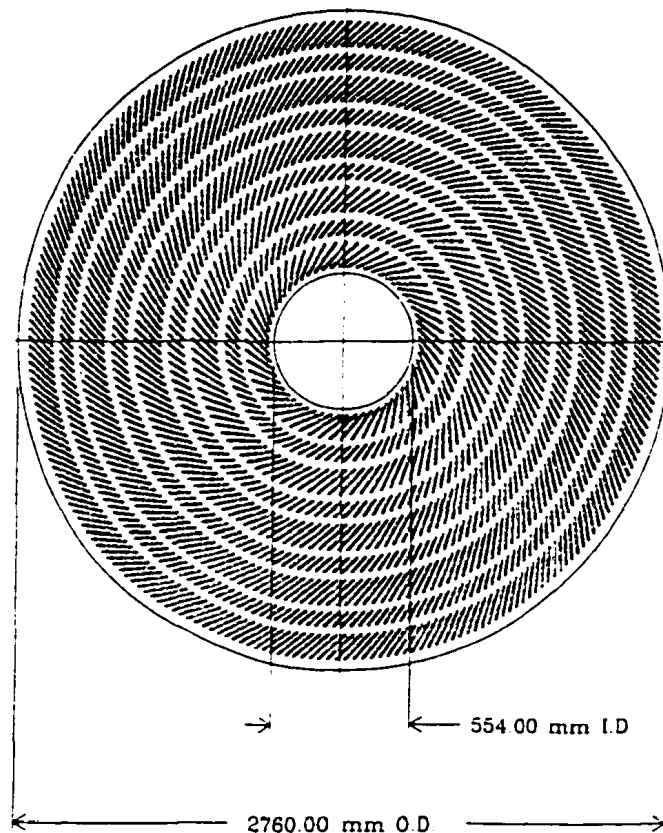


Figure 3.7: CTC endplate. From [1].

Positioned about the sense wires are high voltage field wires which establish a 1350 V/cm electric field. The ionization medium is a mixture of 49.6% Argon, 49.6% Ethane, and 0.8% Ethanol. The maximum drift time of the ionization electrons is 800 ns, much shorter than the 3.5 μ s between bunch crossings. Because of the crossed electric and magnetic fields inside the chamber, the ionization electrons drift to the sense wires with a Lorentz angle of 45° with respect to the electric field. To account for this angle, the layers of wires are tilted 45° relative to the radial direction. A track

is reconstructed by fitting a helix to the hits in the CTC. The transverse momentum resolution of the CTC is

$$\frac{\Delta p_T}{p_T} = 0.002 p_T(\text{GeV}/c). \quad (3.4)$$

By combining the tracking information from the CTC with that from the SVX, the transverse momentum resolution can be improved to

$$\frac{\Delta p_T}{p_T} = 0.001 p_T(\text{GeV}/c). \quad (3.5)$$

3.2.2 Calorimeters

After passing through the tracking system, particles emerging from the interaction point enter the calorimeters. The CDF Calorimeter system is separated into three main detector regions according to their pseudorapidity coverage: the Central, Wall and Plug calorimeters.

3.2.2.1 Central and Wall Calorimeters

The Central calorimeter is a sampling calorimeter. It is longitudinally segmented into an electromagnetic section (CEM) and a hadronic section (CHA). The electromagnetic section consists of alternating layers of 3.175 mm thick Pb absorber plates and 5 mm thick SCSN-38 polystyrene scintillator plates, and the hadronic section consists of alternating layers of 2.5 cm thick steel absorber plates and 1.0 cm thick PMMA (polymethylmethacrylate) scintillator plates. The electromagnetic section is $\sim 17X_0$ ($\sim 1\lambda_0$) in length, and the hadronic section is $\sim 4.7\lambda_0$ in length. Both sections are divided into 24, 15° wedges in ϕ . A diagram of one ϕ wedge is shown in Figure 3.8. Each wedge is divided into 10 projective towers in η , each tower subtending 0.11 units of η . There are two wavelength shifting waveguides per tower, one on each side in azimuth. Connected to the each waveguide is a photomultiplier tube (PMT).

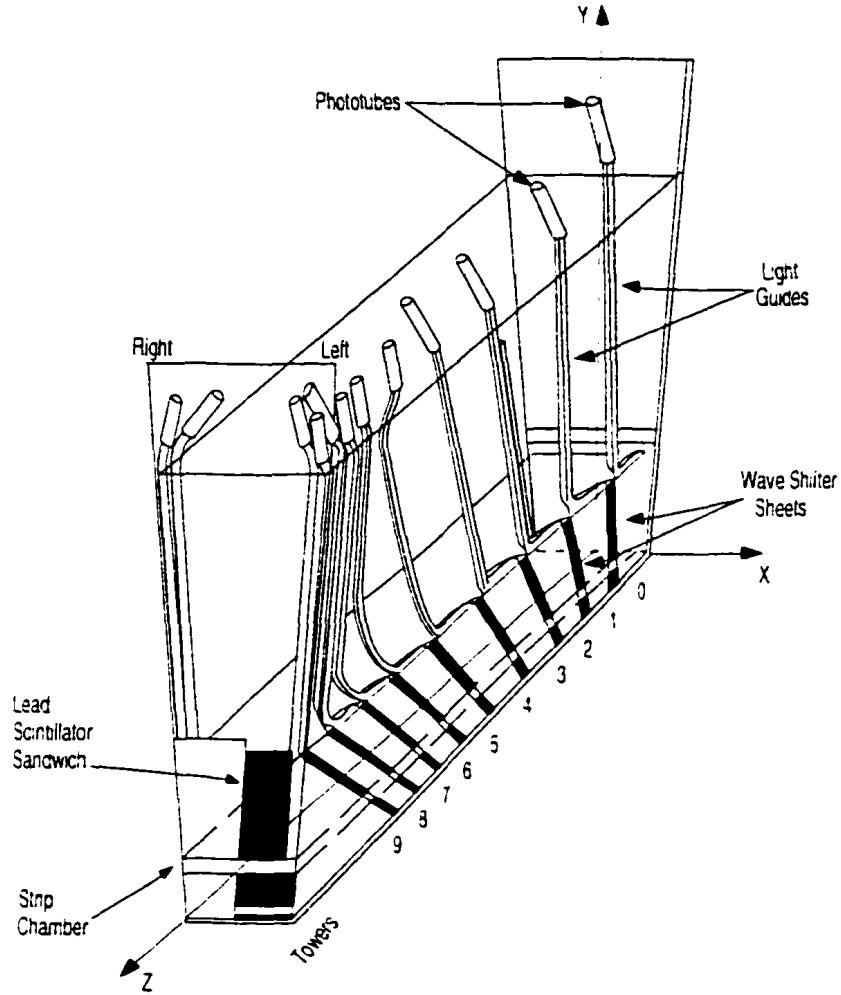


Figure 3.8: A 15° ϕ wedge of the Central calorimeter. From [1].

The Central calorimeter extends 2.5 m parallel to the beamline on either side of $z = 0$ and covers a pseudorapidity range of $|\eta| < 1.1$. The distance from the interaction point to the inner radius of the calorimeter is ~ 173 cm.

As described in Sections 4.5 and 4.6, when a particle hits the calorimeter, it produces a shower. When a charged particle from the shower passes through a scintillating plate, it brings a scintillating molecule into an excited state. When the molecule relaxes back to its original state, it isotropically emits light, usually in the ultraviolet range. Some of the light emitted is then trapped in the scintillating plate and is in-

ternally reflected to the edge of the plate. The two wavelength shifting waveguides at the edges of the plates in ϕ , absorb the ultraviolet light and reemit green light. Some of the green light then travels radially outward toward the end of the waveguide to a PMT.

The Wall calorimeter covers an awkward geometrical region (see Figure 3.3) between the Central calorimeter and the Plug calorimeter. It consists of 5.1 cm thick steel absorber plates alternated with 1.0 cm thick PMMA scintillator plates, and covers a region in pseudorapidity from $\sim 0.66 < |\eta| < \sim 1.1$.

3.2.2.2 Plug Calorimeter

The Plug calorimeter uses gas proportional tube arrays instead of plastic scintillating plates as its active medium. In the electromagnetic section, the 34 layers of proportional tubes are interleaved with 2.7 mm thick layers of Pb. In the hadronic section, 20 layers of proportional tubes are interleaved with 5.1 cm thick steel absorber plates. The segmentation for the electromagnetic and hadronic sections is the same, namely 0.09 in η and 5° in ϕ .

Charge produced by ionizing particles traversing the gas in the proportional tubes is internally amplified. The extent of this amplification, which directly affects the reconstructed energy of shower particles, is quite sensitive to the temperature and pressure of the gas. For this reason, gaseous calorimeters require a substantial amount of monitoring. In addition, gaseous calorimeters have a very small sampling fraction and no saturation effects [5]. This gives rise to the “Texas tower” effect, single towers with signals orders of magnitude larger than those in neighboring towers. For these reasons, the Plug calorimeter was replaced by a scintillator based calorimeter in Run II. The new calorimeter is described in detail in Chapter 5.

3.2.3 Muon Detector

Whereas all other particles (except neutrinos) shower and are thus completely absorbed in the calorimeter, muons generally do not shower in the calorimeter. To first order, they are simply minimum ionizing in the calorimeter. Any particles detected radially beyond the calorimeters then, can be assumed to be muons. There are three components of the muon system at CDF (see Figure 3.3): the Central Muon Chambers (CMU), the Central Muon Upgrade (CMP), and the Central Muon Extension (CMX). All three components consist of single-wire, rectangular drift tubes.

3.2.3.1 Central Muon Chambers (CMU)

The CMU is located radially outside the Central Hadron Calorimeter at a distance of 3.47 m from the beamline and covering a pseudorapidity range of $|\eta| < 0.6$. It is segmented into 24, 12.6° wedges in ϕ . Since there are 2.4° gaps between the wedges, the CMU coverage in ϕ is only 85%. Each CMU wedge contains three towers with each tower containing four radial layers of four drift tubes. The layers are offset from one another by ~ 2 mm to remove ambiguity of which side the particle passed the wires in ϕ . The position resolution of the CMU is $250 \mu\text{m}$ in ϕ and 1.2 mm in z .

3.2.3.2 Central Muon Upgrade (CMP)

The Central Hadron Calorimeter is too short to fully longitudinally contain high energy hadron showers. When the muon system consisted of only the CMU, the tails of high energy hadron showers would often leak out the back of the CHA and produce a signal in the CMU, thus faking a muon. In order to avoid such signals, another 0.6 mm of steel ($2.4 \lambda_0$) was added at the back of the CHA. Behind the added steel, four more layers of drift chambers were added and named the Central Muon Upgrade (CMP). The CMP fills in the gaps between wedges in ϕ in the CMU. At the inner and outer surfaces of the CMP, there are scintillator planes (CSP) used to provide

timing information.

3.2.3.3 Central Muon Extension (CMX)

At the time the CMP was added, another muon system, the Central Muon Extension (CMX) was added in order to extend the muon system's coverage in pseudorapidity in the $0.6 < |\eta| < 1.0$ range. Just as in the CMP, the inner and outer surfaces of the CMX have scintillator planes, known as the CSX.

CHAPTER 4

CALORIMETRY

The subdetector system which is crucial to the analysis discussed in Chapter 7 is the calorimeter. Here, we give a brief summary of the basics of calorimetry. For a complete discussion, the reader is referred to Reference [6].

4.1 What calorimeters measure

In a typical multicomponent detector such as that described in Section 3.2, calorimeters are located just outside the tracking system and are simply a large chunk of dense material. When particles emerging from the interaction point hit the material, they are completely absorbed (and, except for muons and neutrinos, are thus destroyed for further measurement purposes). In the absorption process, certain materials in the calorimeter produce a signal that can be measured. From the signals that result, the energy of the particles can be deduced. While this is the main purpose calorimeters serve, through segmentation, they also often are used to distinguish e 's, γ 's and π^0 's from charged hadrons and to measure the position and angular distributions of particles, particularly jets.

4.2 Parts of a calorimeter

Calorimeters consist of three main parts, the *active material*, the *passive material* (or *absorber*), and the *readout*.

When a charged particle passes through the active material, it generates a signal. Materials that have been used as active material in multipurpose detectors at accelerators include scintillating plastic, quartz, liquid argon, fancy crystals, and various types of gas mixtures. When a charged particle passes through scintillating material, molecules in the material are brought into an excited state. When they relax back

to their ground state, they emit light, usually in the blue or ultraviolet range. This light is collected and measured. When quartz is used as an active material, a signal is generated due to the Čerenkov mechanism, namely light is produced when a particle travels through a medium faster than the speed of light in that medium. When gas or noble liquids (Ar, Kr, Xe) are used as the active medium, ionization is the means through which a signal is produced. When a charged particle passes through the medium, the medium is ionized and the ionization charges are collected or induce a signal in an electrode placed in the medium.

The passive material is usually a dense material which causes a particle to shower and eventually completely absorbs the particle. Popular choices for the absorber material include Pb, steel (Fe), ^{238}U , and fancy crystals such as thallium-doped cesium iodide or lead tungstate (PbWO_4).

The readout consists of the system which transports the signals produced inside the active material to a more convenient location outside of the material where other instruments and electronics that can measure and process the signal are located. Waveguides or wavelength shifting material and PMTs are often used to transport and measure the signal, respectively, in light based calorimeters. In ionization based calorimeters, electrodes are used to collect charge.

4.3 Types of calorimeters

There are two main types of calorimeters: *sampling* and *homogeneous*. In a sampling calorimeter, the active medium is a different material than the passive medium and is somehow interspersed within the absorber. Since a signal is produced only in the active medium, the calorimeter “samples” the energy deposition of the incoming particle’s shower. One type of sampling calorimeter consists of alternating planes of absorber and active medium, such as scintillating plates or liquid argon alternated with plates of your favorite absorber (steel or Pb, for example). In other designs,

interleaved throughout the absorber structure are scintillating or quartz fibers.

In a homogeneous calorimeter, the active and passive media are one and the same material. Crystals and lead/glass are the most common materials used in a homogeneous calorimeter in large hybrid detectors at high energy particle accelerators. In cosmic ray experiments, the air of the atmosphere, the water of oceans, or the ice of the Antarctic act as a homogeneous calorimeter, both producing a measurable signal and absorbing the cosmic rays.

4.4 Segmentation

Calorimeters are often “segmented” into *lateral sections* and *longitudinal sections*. Segmentation simply means that the signal from a particular physical region of the calorimeter is read out separately from other physical regions. Lateral segmentation usually refers to the segmentation of the calorimeter into towers of η and ϕ . Typically, the tower structure is projective, meaning the cross sectional area of the tower gets larger as a function of the distance from the interaction point. Lateral segmentation gives a means of measuring the production angle of the particles detected and resolving showers from several particles traversing the same physical area. The precision with which the production angle of particles can be measured depends not only on the granularity of the lateral segmentation but the physical size of the showers induced by the particles in the calorimeter. Typical lateral segmentation involves towers with a size of ~ 0.1 units of η and $\sim 15^\circ$ of ϕ . This results in several hundred (> 500) separate towers of lateral segmentation.

Longitudinal segmentation refers to segmentation along the direction travelled by particles from the interaction point. There are many fewer longitudinal segmentations than lateral ones. Very often, in fact, there are only two longitudinal segments, referred to as the “electromagnetic” and “hadronic” sections. The electromagnetic section’s main purpose is to measure the energy of electrons and photons. Since

electrons and photons are absorbed in a relatively small amount of material (see Section 4.5.1). the electromagnetic section is placed in front of (as seen by particles emerging from the interaction point) the hadronic section. The hadronic section combined with the electromagnetic section measures the energy of charged hadrons which require more material to deposit their energy.

Electrons and photons deposit their energy in a different way than charged hadrons. The calorimeter properties needed to optimize the resolution of a calorimeter are different (in fact, they are completely opposite) for electrons and charged hadrons [7]. For this reason, the electromagnetic and hadronic sections are usually built with different compositions. If the composition of the electromagnetic section is chosen for optimal electromagnetic energy resolution, then since the signals from the electromagnetic section are used in combination with those from the hadronic section to measure the energy of a charged hadron, the energy resolution for charged hadrons suffers (charged hadrons would be measured better with a calorimeter with no electromagnetic section in front of it). Thus, longitudinal segmentation allows for excellent energy resolution for one type of particle but rather poor energy resolution for the other type of particle.

Longitudinal segmentation also allows for particle identification. Since electrons (and γ s) deposit most of their energy in the electromagnetic section, whereas charged hadrons deposit energy in both sections, electrons (and γ s) can be discriminated from charged hadrons by cutting on the ratio of signal in the hadronic section with the signal in the electromagnetic section.

While longitudinal segmentation allows particle identification and the optimization of resolution for one type of particle, it introduces significant complications in the calibration of the calorimeter. These complications are discussed in Chapter 5.

4.5 Electromagnetic (em) showers

When an electron interacts with matter, it loses energy via ionization or Bremsstrahlung radiation. Photons interact via the photoelectric effect, Compton scattering or pair production. An electron (or photon) that hits a block of matter with enough energy (>100 MeV) will start a process known as a cascade or shower. It usually uses soap and shampoo and sometimes likes to take a bath instead¹. In this process, the electron radiates Bremsstrahlung photons. Those photons in turn interact via one of their interaction processes (photoelectric effect, Compton scattering or pair production). Photons with enough energy (5-10 MeV) will produce an energetic electron-positron pair. The resulting electron and positron can also emit Bremsstrahlung photons which with enough energy can create other electron-positron pairs and so on. Thus, the number of particles interacting inside the material as a function of depth increases. At some point (called the shower maximum) inside the material, electrons produced by the shower process no longer have enough energy to emit Bremsstrahlung radiation, and they simply deposit their energy in the material by ionizing it. At lower energies, photons too will interact via Compton scattering or the photoelectric effect, thus not multiplying the number of shower particles interacting. In this way, beyond the shower maximum, the number of particles decreases.

It should be noted that all of the kinetic energy of the incoming electron (or photon) is eventually deposited in the material in the form of ionization charge which can be measured or by exciting atoms or molecules which upon returning to the ground state emit light that can be measured.

¹This often proves difficult to measure.

4.5.1 Physical size of em showers

The *radiation length*, X_0 , is defined as the distance over which a high-energy ($\gg 1$ GeV) electron or positron loses, on average, $1 - e^{-1}$ of its energy to Bremsstrahlung radiation. This variable is used to describe the longitudinal dimension of an electromagnetic shower in a material independent way. The radiation lengths of Pb and Fe are 0.56 cm and 1.76 cm, respectively. The radiation length of water is 36.1 cm. Thus, an electron loses the same fraction of its energy in 0.56 cm of Pb, 1.76 cm of Fe, or 36.1 cm of water.

The depth (in units of X_0) of the shower maximum depends logarithmically on the energy of the incoming electron. The lateral development of an electromagnetic shower is independent of the energy of the incoming particle.

4.5.2 Resolution of em showers

Energy which is deposited in the active portion of the calorimeter is turned into a signal, but energy which is deposited in the passive layers (in sampling calorimeters) does not result in a signal. The fluctuations in the amount of energy which is deposited in the active material of the calorimeter (and thus fluctuations in the signal) are called *sampling fluctuations*. In sampling calorimeters, sampling fluctuations usually dominate the energy resolution for em showers. Sampling fluctuations follow Poisson statistics. Thus, if a particle of energy E produces n photoelectrons on average, the event-to-event fluctuations on that number are \sqrt{n} . The relative precision with which the calorimeter can measure energy (i.e., the relative width of the signal distribution) is then $\sigma_E/E = \sqrt{n}/n = 1/\sqrt{n}$. If a calorimeter is linear, then a particle with energy xE will produce xn photoelectrons when absorbed by the calorimeter. The relative precision of the energy measurement is then $\sqrt{xn}/xn = \sqrt{x}/x \cdot 1/\sqrt{n}$, a factor \sqrt{x}/x better than for a particle of energy E . For linear calorimeters this leads to the form

often quoted as the energy resolution of a calorimeter

$$\sigma_E/E = a/\sqrt{E} \quad (4.1)$$

where a is a parameter characterizing the calorimeter quality and E is given in GeV. The larger the *sampling fraction*, which is defined as the energy deposited by a minimum ionizing particle (mip) in the active calorimeter layers, measured relative to the total energy deposited by such particles in the calorimeter, the better the energy resolution for em shower detection². In homogeneous calorimeters, the sampling fraction is 100%, so there are no sampling fluctuations. For this reason, homogenous calorimeters have the best resolution for electromagnetic showers. The energy resolution of these calorimeters is limited by factors such as light collection efficiency.

4.6 Hadronic showers

When a high energy charged hadron hits a block of matter, the shower that develops is more complicated than the electromagnetic shower described in Section 4.5. While the basic idea is the same, the number of particles interacting in the material increases up to a certain depth in the calorimeter and then decreases after that point, the number of different processes that may contribute to this phenomenon is much larger. The incoming hadron can interact strongly with the nuclei of the absorber material and protons and neutrons can be released from the nuclei. Also when the incoming particle interacts with a nucleus, the particle can change its identity and produce additional mesons or baryons. Some of these hadrons are neutral and decay electromagnetically as is discussed in Section 4.6.3.

²*Sampling frequency* also plays a role in the energy resolution of a calorimeter for em shower detection [6].

4.6.1 Physical size of hadron showers

Hadron showers are spatially larger than electromagnetic showers, both longitudinally and laterally. Hadron showers are characterized by the nuclear interaction length, λ_0 which is defined as the average distance a high energy hadron must travel inside a material before a nuclear interaction occurs. The probability a hadron will not undergo a nuclear interaction after travelling a distance z inside a material is

$$P = e^{-z/\lambda_0}. \quad (4.2)$$

Unlike electrons, hadrons can penetrate a material quite deeply before starting a shower. Thus, the fluctuations in the longitudinal energy deposit profile are large. As with electromagnetic showers, the average longitudinal development of a hadron shower depends logarithmically on the energy of the incoming particle. Unlike electromagnetic showers, however, the transverse dimensions of hadron showers become *smaller* with increasing energy of the incoming particle. This is due to the increase in the electromagnetic component of a hadron shower as the energy of the incoming particle increases (see Section 4.6.3).

4.6.2 Invisible energy

One of the biggest differences between electromagnetic and hadronic showers is the phenomenon of *invisible energy*, energy which is deposited in the calorimeter but which does not result in a measurable signal. Since nuclei have large binding energies, it takes a considerable amount of energy to break up a nucleus. The energy used to do so does not result in a measurable signal. The fluctuations in the amount of invisible energy from event to event are large, on average 40% of the non-em component. Thus, the best energy resolution that can be attained for hadronic showers is intrinsically worse than that for electromagnetic showers.

4.6.3 Electromagnetic component of hadron showers

Another difference between electromagnetic and hadronic showers that worsens the hadronic energy resolution in many calorimeters (noncompensating ones) is the fact that there is an electromagnetic component of hadronic showers. When a charged hadron interacts with an absorber nucleus, a variety of processes can turn the incoming hadron into a different hadron, or can turn the incoming hadron into many new hadrons. Some of these hadrons (on average 1/3 of them) are neutral (mostly π^0 s and η s) and decay electromagnetically into photons. These photons produce electromagnetic showers. We will refer to the portion of a hadron shower which ends up as neutral mesons and thus as electromagnetic showers in this way as the *electromagnetic (em) component* or π^0 *component* of the shower. We will refer to the other portion of the shower as the *hadronic component* or *non-em component* of the hadron shower.

The fraction of the incoming hadron's energy which ends up as the electromagnetic component varies greatly from one event to the next. Also, on average, the electromagnetic component increases as the energy of the incoming hadron increases. The two points have important consequences for the resolution and response (defined in Section 4.6.4), respectively of a calorimeter.

4.6.4 Compensation and noncompensation (e/h)

In most calorimeters, the amount of signal produced by a 50 GeV charged hadron is smaller than the amount of signal produced by a 50 GeV electron or photon. This is due to the invisible energy phenomenon discussed in Section 4.6.2. In a hadron shower, some energy from the incoming hadron is used to break up absorber nuclei which in general does not produce a signal.

The *response* of a calorimeter to a certain type of particle is defined as the average calorimeter signal divided by the incoming energy of the particle that caused the signal. The response for a type of particle, X is denoted simply as X . The response

of a calorimeter to electrons and pions, for instance, is e and π .

The extent to which the calorimeter signals from electrons and charged hadrons of the same energy differ in a calorimeter is given by a quantity known as the e/h value, the response of the calorimeter to electrons divided by the response of the calorimeter to the hadronic component of hadron showers, h . The quantity h is given by

$$h = f_{rel} \cdot rel + f_p \cdot p + f_n \cdot n + f_{inv} \cdot inv \quad (4.3)$$

where f_{rel} , f_p , f_n , f_{inv} is the fraction of non-em shower energy carried by relativistic charged pions, spallation protons, evaporation neutrons, and invisible energy (used to release protons and neutrons from absorber nuclei), and rel , p , n and inv are the calorimeter's responses to relativistic charged pions, spallation protons, evaporation neutrons, and invisible energy, respectively. The quantity inv is, by definition, zero.

In *noncompensating calorimeters*, $e/h \neq 1$. In most calorimeters, the response of the calorimeter to electromagnetic energy deposition is larger than the response to hadronic energy deposition, $e/h > 1$. In some calorimeters, the signal resulting from an electron and charged hadron of the same energy is on average the same, i.e., $e/h = 1$. These calorimeters are referred to as *compensating calorimeters*. In these calorimeters, either the signal produced by the electromagnetic component of hadron showers is suppressed to some extent or the signal produced by the hadronic component of hadron showers is enhanced to some extent so that the response of the calorimeter to both types of energy deposit is equalized.

4.6.5 Consequences of noncompensation

The fluctuations from event to event in the electromagnetic component of hadron showers are large and not of a Gaussian nature. If the calorimeter response to these two types of energy deposit are different (as in noncompensating calorimeters), then these fluctuations usually dominate the energy resolution. In compensating calorime-

ters, the response to the two types of particles is the same. Then, the fluctuations in the electromagnetic component of hadron showers do not affect the energy resolution. Hence, the calorimeters with the best hadronic energy resolution are compensating ones.

Since the electromagnetic component of hadronic showers increases on average with the energy of the incoming charged hadron, the response of a noncompensating calorimeter increases as a function of energy. Thus, if the response in a noncompensating calorimeter to a 50 GeV charged pion is 50 photoelectrons per GeV, the response to a 100 GeV charged pion will not be 50 photoelectrons per GeV, but rather something like 70 photoelectrons per GeV. In compensating calorimeters, however, the average increase in the electromagnetic component of hadron showers has no effect on the response and compensating calorimeter have a linear response for hadron shower detection.

4.7 Radiation Damage Issues

4.7.1 Radiation damage studies for the CMS very forward calorimeter

At the future Large Hadron Collider (LHC), an unprecedented luminosity and center of mass energy will (hopefully) be reached. This collider will slam protons with protons at $\sqrt{s} \sim 14$ TeV and an integrated luminosity of ~ 1000 fb⁻¹ over 10 years. Detectors at this collider will have to withstand enormous amounts of radiation. In the forward region ($\eta > 3$) especially, the dose delivered to the detectors will be extremely large, ~ 1 -10 MGy in 10 years of running.³

It is imperative, then, that the detectors built at this collider are extremely radiation hard. The CMS experiment (Compact Muon Solenoid) has chosen a very forward calorimeter composed of quartz fibers as the active material. Here we summarize the

³1 Gray = 1 J kg⁻¹ = 100 rad = 6.24 · 10¹² MeV kg⁻¹

results of a dedicated study of the effects of radiation damage on calorimeter performance in which a prototype of the very forward calorimeter was irradiated (at CERN) with the types of particles responsible for most of the radiation doses at the LHC. Details of this study, which were published in [8] can be found in Appendix A.

The detector used in this study consisted of thin (0.60 mm diameter) quartz fibers embedded in a copper matrix. The fibers were oriented along the direction travelled by the incoming particles. The showering particles generated Čerenkov light in the fibers, and photons emitted within the numerical aperture of the fibers were captured and transported through internal reflection to the fiber ends. There they were converted into photoelectrons in the photocathode of a PMT, and the digitized output of the PMTs comprised the calorimeter signals. The calorimeter was 33.75 cm in depth ($22.6 X_0$) and was comprised of 12 towers. The fibers were read out at one end and made reflective by aluminum deposition at the other end. More details about this calorimeter can be found in [9].

4.7.2 Radiation exposure

The radiation experienced by detectors operating at $3 < |\eta| < 5$ at the LHC comes primarily from the pp collisions as opposed to beam-gas interactions. The most abundant particles emerging from the interactions are low energy (1 GeV) pions, neutral and charged. Radiation damage in the calorimeter results mostly from the electromagnetic showers induced by photons (decay products of neutral pions), since photons deposit their energy in a limited depth in the calorimeter. To mimick this situation, the prototype calorimeter module was exposed to an intense beam of 0.5 GeV electrons, produced by the Linear Injector for LEP (LIL) at CERN. The beam intensity during this exposure was typically a few times 10^{11} electrons per second. This beam was steered perpendicular to the mirrored fiber surface (see Figure 4.1). Over ~ 3 days, a total of $1.45 \cdot 10^{16}$ electrons with an energy of 0.5 GeV each were sent

into an area of a few cm^2 . The calorimeter became quite radioactive in this process, requiring ~ 3 days to cool down before it could be transported to the testbeam area (H4 beamline at CERN).

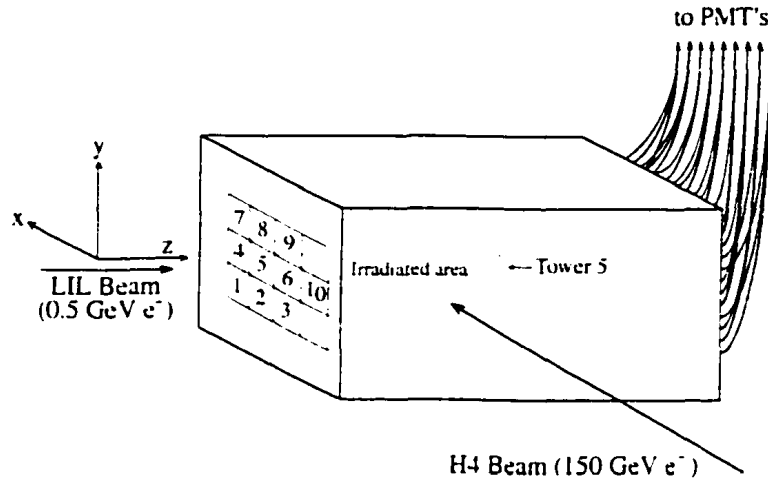


Figure 4.1: Orientation of the quartz fiber calorimeter prototype during testbeam studies of the effects of radiation damage. The tower numbering scheme used for these studies is shown. The direction of the beam used to irradiate the module (LIL Beam) and the direction of the beam used to assess the effects of irradiation on the calorimeter's performance (H4 Beam) are shown.

4.7.3 Data Analysis

The effects of the calorimeter's performance were measured using a beam of 150 GeV electrons at the CERN H4 beamline sent into the detector sideways, i.e., perpendicular to the fiber plane (see Figure 4.1). The calorimeter response was measured as a function of z , the distance between the impact point of the particles and the aluminized front face of the detector. An example of the results of such a z -scan is shown in Figure 4.2a, where the average signal recorded in Tower 5 is plotted as a function of z . In Figure 4.2b, this data is divided into events in which the electrons entered the detector at $y = 0 - 5$ mm or $y = 20 - 25$ mm. Before the irradiation, the signals recorded in scans of this type were practically independent of z . After the irradiation, however, a clear reduction in the signals was observed. This is indicated

by a change in the shape of the z -scan data, namely a kink at a depth $z = 15 - 20$ cm. This agrees with Monte Carlo simulations of the dose absorbed by the calorimeter from the LIL beam which showed that the radiation effects were limited to the area $z < 20$ cm.

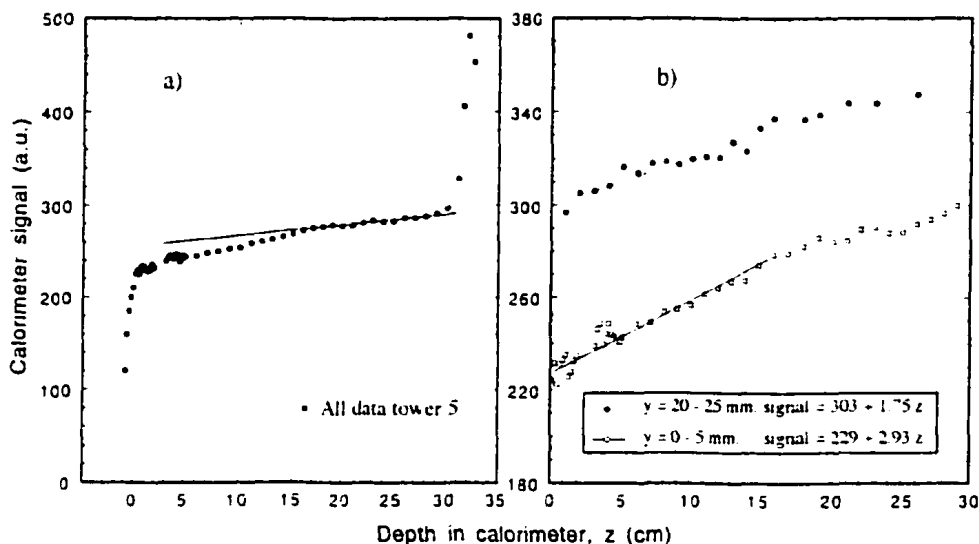


Figure 4.2: The average signal in Tower 5 recorded in z -scans with electrons entering the detector in the regions $y = 0 - 5$ mm and $y = 20 - 25$ mm, respectively.

4.7.4 A model that reproduces data

We used a Monte Carlo simulation based on a simple model in an attempt to reproduce the experimental z -scans. In this model, the local loss in light transmission is parameterized as

$$\frac{1}{l(z)} = \frac{1}{l_0} + \alpha_0 D(z)^{1-n} \quad (4.4)$$

where $l(z)$ is the attenuation length at a depth z inside the calorimeter after the detector has received a radiation dose $D(z)$, and l_0 represents the attenuation length in the absence of radiation. The radiation sensitivity of the detector is measured by the value of the parameter α_0 . A small value of α_0 corresponds to a small radiation sensitivity (i.e., a large radiation hardness).

With this model, simulated response curves (z -scans) were obtained as follows. The Čerenkov light produced at a certain depth z and trapped inside the fibers was split into two components, with equal fractions going to the right ($+\hat{z}$, straight to the PMT) and to the left ($-\hat{z}$, to the aluminized front end of the fibers). The photons in both components were tracked in steps of 0.5 cm on their way through the fiber. In every step, the light intensity was diminished by a factor $\exp[-0.5/l(z')]$, with the local attenuation length $l(z')$ at depth z' expressed in cm. Light traveling to the left ($-\hat{z}$, see Figure 4.1) was assumed to undergo an intensity loss of 20% upon reflection off the mirrored fiber end. The value of l_0 was taken as 20 m. Both numbers were based on results of measurements with an unirradiated module of exactly the same composition [9]. In this way, the fraction of the Čerenkov light trapped in the fibers that reached the PMT was calculated. By repeating the described procedure for a large number of points at different depths (z), the simulated response curve was obtained.

In order to reproduce the experimental data, we found that the attenuation length had a power-law dependence on the dose levels. In radiation hardness studies of plastic scintillating fibers, the attenuation length was found to be a linear function of the received dose (Eq. 4.4 with $n = 0$). In the quartz fibers used in this study, however, it turned out that a power-law dependence more accurately described the data.

Figure 4.3 shows the results of the simulations described above when a value of $n = 0$ is used. The simulated curves exhibit the same characteristic features as the experimental data: a more or less flat response for z -values larger than 20 cm, where the radiation effects become negligibly small and a more or less logarithmic decline of the response for light produced in the affected region of the calorimeter ($z < 20$ cm). From the observed z -dependence in the first 10 cm in the figure, one would conclude that α_0 amounts to $(3 - 4) \cdot 10^{-4} \text{ Mrad}^{-1} \text{ cm}^{-1}$. However, for such a value of α_0 , the kink separating the z range of flat response and the z range affected by the radiation

dose appears to be located deeper inside the detector than the simulations lead us to believe ($z \approx 20$ cm experimentally, vs. $z \approx 10$ cm in the simulations).

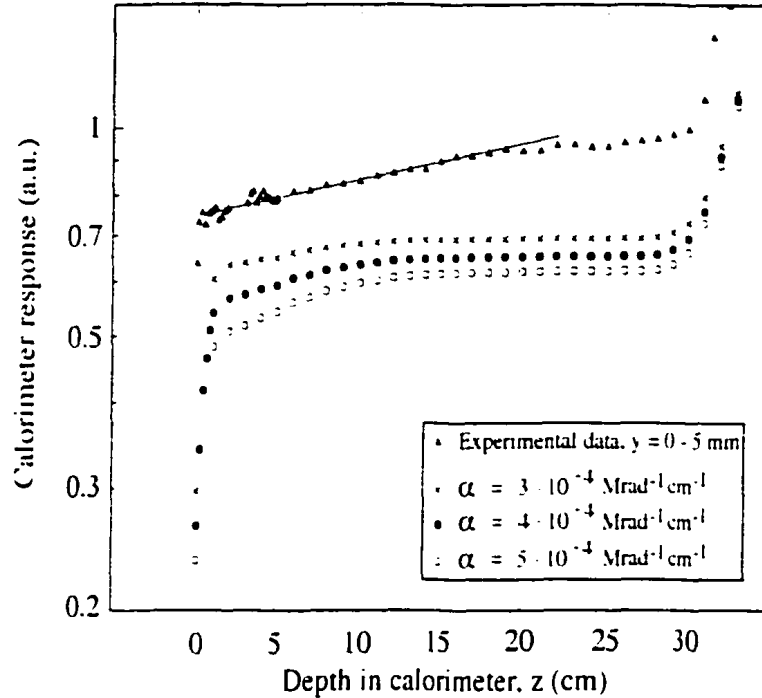


Figure 4.3: Simulated response curves based on Equation 4.4 and the dose profile $D(z)$ accumulated in the y interval 0-5 mm for $n = 0$ and different values of the parameter α . For comparison, the experimental z -response curve for $y = 0 - 5$ mm, conveniently normalized, is shown as well. See text for details.

When we repeated this analysis (with $n = 0$) for other regions in which z -scans had been performed (i.e., for different y -slices, where the induced doses were much smaller), we found that considerably larger values of α_0 were needed to describe the measured response curves. And, as before, the simulations (with $n = 0$) were only capable of reproducing the z dependence in the first part of the detector, whereas the experimental effects of the induced radiation extended much deeper inside the calorimeter.

This led us to believe that in order to adequately describe the experimental data for quartz fibers, $1/\lambda(z)$ is not a linear function of dose, but a function of some power of the dose. Figure 4.4 shows the results of simulations performed with various values

of α_0 and n . In these simulations, the value of n determines the location in depth of the kink. The value of α_0 determines the slope of the region in front of the kink in z . The best reproduction of the experimental position of the kink (at $z \approx 20$ cm) was found for $n = 0.7$, and the corresponding optimum value of α_0 was 0.010.

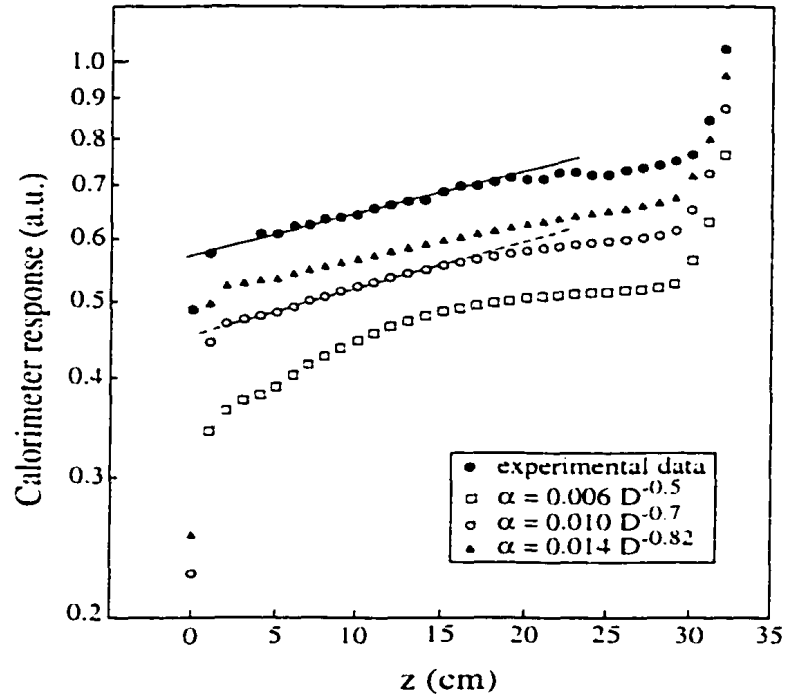


Figure 4.4: Simulated response curves based on Equation 4.4 and the dose profile $D(z)$ accumulated in the y interval 0-5 mm for different values of the parameters n and α . For comparison, the experimentally measured curve is shown as well. See text for details.

The fact that $1/\lambda(z)$ is a function of some power of the dose means that relatively small doses of radiation cause relatively large effects of induced light attenuation. At doses of a few megarads, the radiation hardness is not much better than that of the best plastic scintillators [10], but at much higher doses the radiation hardness is considerably better.

CHAPTER 5

CALIBRATING LONGITUDINALLY SEGMENTED CALORIMETERS

Calibrating a calorimeter is a tricky business. In this chapter, some of the subtleties of calorimeter calibration are addressed.

5.1 CDF Plug Upgrade Calorimeter

The analysis discussed in the next section was carried out with testbeam data from the new endplug calorimeter of the Collider Detector at Fermilab (CDF). This calorimeter system was modified as part of the upgrade program in preparation for Run II at the Tevatron. It covers the pseudorapidity range from 1.1 – 3.6 and replaces the original gas-based calorimeter. The new detector consists of a $0.75\lambda_{\text{int}}$ deep electromagnetic (EM) section and a $7.4\lambda_{\text{int}}$ deep hadronic (HAD) section. The electromagnetic section has a lead/scintillator sandwich structure, with 4.5 mm thick lead plates alternated by 4.0 mm thick plastic scintillator plates. In the hadronic section, 6.0 mm thick scintillator plates are sandwiched between 50.8 mm thick iron absorber plates. The signals are read out by means of wavelength shifting optical fibers, which are embedded in the scintillator plates. The electromagnetic and hadronic sections are both noncompensating devices with e/h values of 1.43 and 1.36, respectively. More details about this device are given in Reference [11].

5.2 CDF Plug Upgrade testbeam analysis

Finding the correct energy scale of a calorimeter which is divided into an electromagnetic and a hadronic section is not trivial [12]. The energy scale is the constant which converts the signal from the calorimeter to units of energy. If a calorimeter is longitudinally divided into two sections with different material compositions, then an energy scale is needed for each section separately.

The energy scale of a calorimeter is (at least initially) determined from a test-beam of particles of the type that the calorimeter will measure with a well defined energy. Such a beam is sent into the calorimeter, and the ratio of the signal from the calorimeter (ADC counts) with the energy of the incoming particles (GeV) is defined as the energy scale. In most longitudinally segmented calorimeter systems, determining the energy scale of the electromagnetic section is straightforward since the electromagnetic section is deep enough to fully contain the shower from an incoming electron. A testbeam of electrons is sent into the electromagnetic section and the ratio of the signal from the electromagnetic section (ADC counts) with the energy of the incoming electrons (GeV) is defined as the energy scale for that section. Determining the energy scale of the hadronic section, however, is tricky. In most calorimeter systems with two longitudinal segments, hadrons deposit their energy in *both* segments. We have studied three methods to determine the energy scale of the hadronic section using experimental data taken with a special module of the CDF Plug Upgrade Calorimeter that was built for testbeam purposes. This module consists of four 15° sections which are replicas of the actual Plug Upgrade calorimeter (see Figure 5.1). One of these four wedges was built without an EM compartment. The results of this study were published in *Nuclear Instruments and Methods in Physics Research*. Here, we summarize the most important results and refer to Appendix B for details.

5.2.1 The calibration methods

5.2.1.1 Electromagnetic section energy scale

Although we discuss three different methods of determining the energy scale of the hadronic section, we only used one method to determine the energy scale of the electromagnetic section. The energy scale of the electromagnetic section, A , was determined with beams of electrons (ranging from 8-180 GeV) sent into the electromagnetic section. Figure 5.2 shows the value of A as a function of the electron

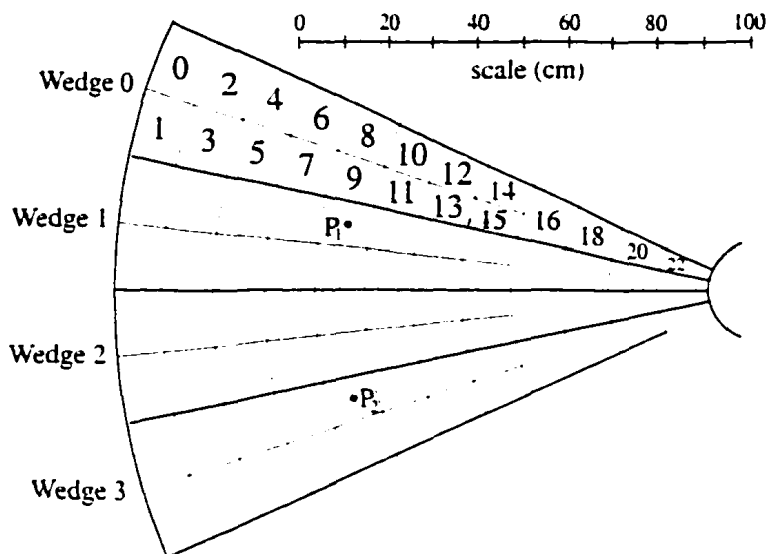


Figure 5.1: The Plug Upgrade testbeam module consisted of four 15° sections, each with 20 towers. Wedge 3 was built *without* an EM section.

beam energy. The value of A is constant within experimental uncertainties over this energy range. The weighted average was found to be $A = 128.1$ counts/GeV.

5.2.1.2 Hadronic section energy scale—Method I

In this method, a beam of pions with a well defined energy is sent into the electromagnetic section of the calorimeter (with, of course, the hadronic section directly behind it). Pions which pass through the electromagnetic section without undergoing a nuclear interaction (“penetrating pions”) are selected. For only those penetrating pions, the ratio of the signal from the hadronic section (ADC counts) with the energy of the incoming pions (GeV) is defined as the energy scale of the hadronic section. Pions with energies ranging from 8-160 GeV were used to find the value of the hadronic section energy scale B_I with this method. Figure 5.3 shows the value of B_I as a function of the energy deposited in the hadronic calorimeter section by the penetrating pions. Note the logarithmic scale of the horizontal axis. Unlike A , the value of B_I is clearly energy-dependent. This is the method CDF has traditionally used to calibrate

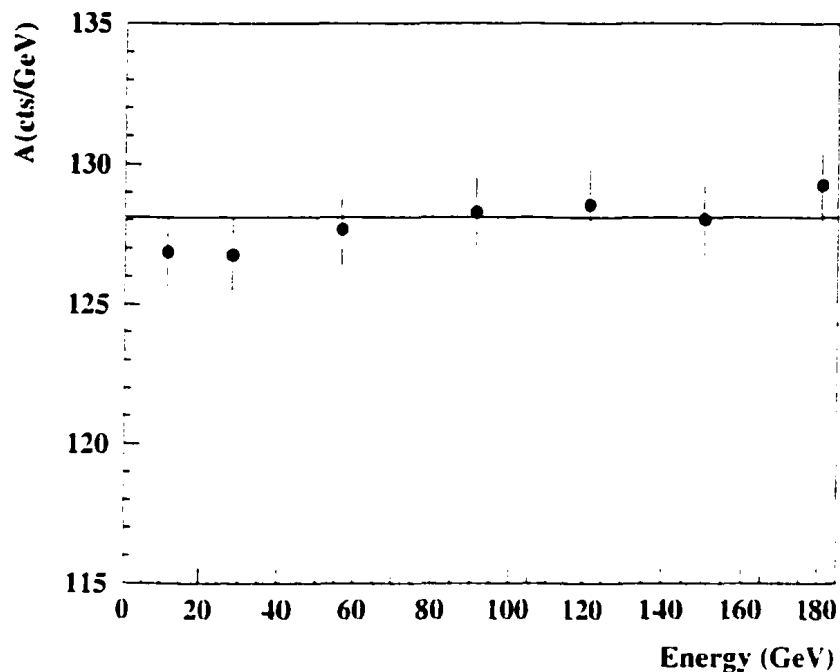


Figure 5.2: The energy scale for the EM calorimeter section, A , as a function of energy.

the hadronic calorimeter section.

5.2.1.3 Hadronic section energy scale—Method II

In this method, the calibration constants of both calorimeter sections are established with the same type of particles. The underlying philosophy of this method is that the relationship between deposited energy and resulting calorimeter signal should be established in the same way for all segments of the calorimeter system. In our case, we used a beam of high-energy electrons, sent directly into the hadronic calorimeter section, to test the merits of this method. In practice this method is usually impossible to implement in an experiment, since the HAD section is shielded from the particle source (i.e., the interaction region) by the EM section. However,

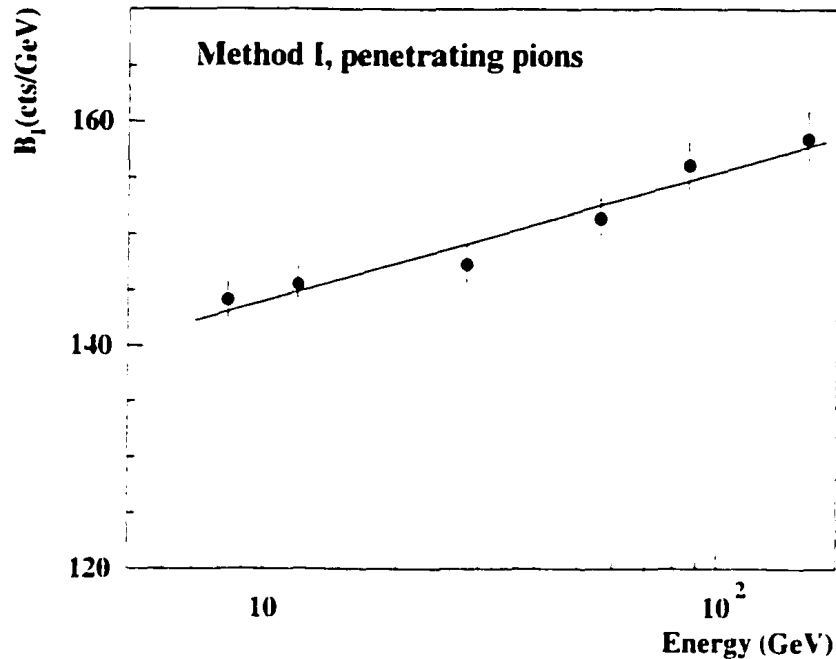


Figure 5.3: The energy scale of the hadronic section, B_I , found using Method I as a function of the energy deposited in the hadronic section of the calorimeter by penetrating pions.

in our testbeam setup we could study this method thanks to the fact that part of the tested calorimeter was *not* equipped with an EM section. Electrons with energies ranging from 11-177 GeV were used to find the value of the hadronic section energy scale B_{II} , which is shown as a function of the electron energy in Figure 5.4. B_{II} is constant, 173.5 counts/GeV, for a wide range of electron energies.

5.2.1.4 Hadronic section energy scale—Method III

In this method, which to our knowledge has not yet been applied in any other experiment, pions with a well-defined energy are used to intercalibrate the EM and HAD calorimeter sections. The calibration constant for the EM section is, as usual,

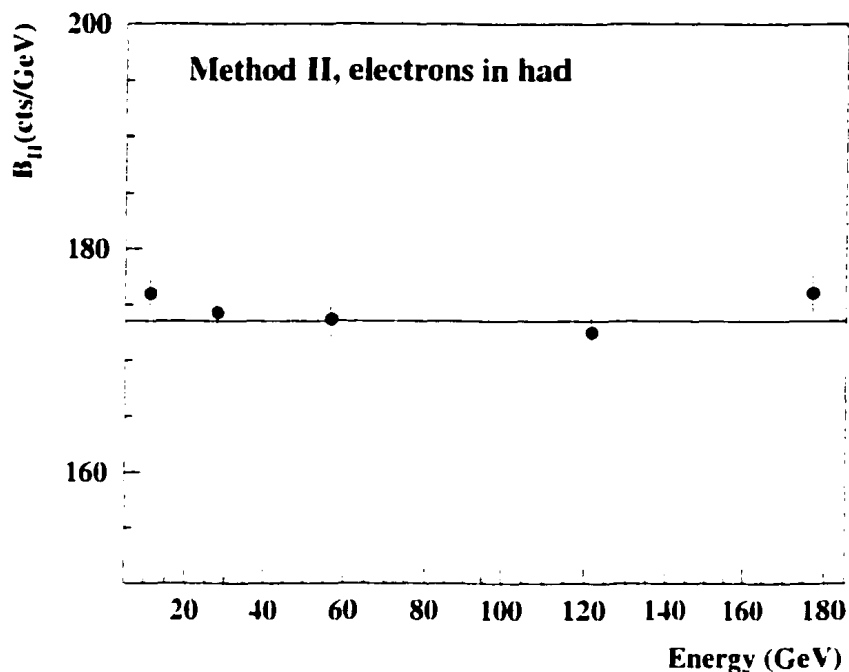


Figure 5.4: The energy scale of the hadronic section. B_{II} , found using Method II as a function of the energy of the incoming electrons.

determined with electrons of known energy, while the calibration constant for the HAD section is chosen such that the average energy reconstructed for penetrating pions is equal to that for nonpenetrating pions.

The underlying philosophy of this method is to avoid any dependence of the reconstructed (hadronic) energy on the starting point of the showers. As we will see later, such a dependence is an inevitable consequence of the application of Method I. Unlike Method II, this method has the advantage that it can be implemented in practice and that it can be applied *in situ* using reconstructed tracks of isolated particles produced in the interactions studied by the experiment.

In order to avoid the effects of shower leakage, we used several low energy (<20

GeV) pion runs to find the value of the hadronic section energy scale B_{III} using this method. We found an average value $B_{III} = 186.5$ counts/GeV.

5.2.2 Experimental consequences of each method

The reconstructed energy is defined as

$$E_{\text{recon}} = \frac{\text{EM signal (ADC cts)}}{A} + \frac{\text{HAD signal (ADC cts)}}{B_{I,II,III}} \quad (5.1)$$

where A is the energy scale of the electromagnetic section and $B_{I,II,III}$ denotes the energy scale of the hadronic section according to Method I, II, or III.

If we chose Method I to set the energy scale of the HAD section, we would need to specify the energy at which the calibration constant B_I was determined, since this value is energy dependent. Depending on the energy, the value of B_I may change by as much as 10%. The other two methods are based on energy-independent calibration constants. In practice, we used a value $B_I = 151.4$ cts/GeV for our studies of the implications of Method I, i.e., the value obtained for the 56 GeV point and an approximate average of all the values obtained over the energy range we studied.

For each method, we (1) compared the reconstructed energy of penetrating pions (late showering pions) with the reconstructed energy of nonpenetrating pions (early showering pions) and (2) plotted the ratio of the reconstructed energy with the beam energy as a function of the beam energy.

5.2.2.1 Dependence on the starting point of the showers

We studied the implications of the various calibration methods with events collected in the 8.6 GeV pion beam. We split these events into two samples, based on the starting point of the showers: The penetrating and the nonpenetrating events.

Figure 5.5 shows the reconstructed energy distributions for these two event samples, obtained on the basis of Method I, using $B_I = 151.4$ cts/GeV. The mean values

of these two distributions differ by 15%. From these results, we conclude that using Method I to set the energy scale of the hadronic section of the calorimeter introduces a dependence of the reconstructed energy on the starting point of the pion shower. This is, in fact, a logical and inevitable consequence of using this method with a noncompensating calorimeter. If penetrating pions are used to set the energy scale for the hadronic section, then it is only for this particular sample of pions that the energy will be reconstructed correctly. The value of B_I found using Method I gives a larger weight to the signal in the hadronic section. Pions which begin showering in the electromagnetic section do not fully benefit from this “boosting” of the hadronic section’s signal and will therefore have a reconstructed energy which is smaller than that of penetrating pions.

Figure 5.6 shows the signal distributions for the same event samples, but this time Method III has been used to calculate the reconstructed energy ($B_{III} = 186.5$ counts/GeV). In this case, the mean values of the reconstructed energies of the penetrating and the nonpenetrating pions were found to be equal within the experimental uncertainties (a small fraction of 1%).

5.2.2.2 Signal nonlinearity

For hadron showers, the average energy fraction carried by π^0 s and other particles developing electromagnetic showers (e.g., η s) increases as a function of energy [13, 14]. This causes an *intrinsic* signal nonlinearity for hadrons in *all* noncompensating calorimeters. This intrinsic nonlinearity appears when the pion energy is reconstructed using the calibration constant B_{III} for the signals from the hadronic calorimeter section. If Method I is used to reconstruct the energy of pions, then one sees a *larger* nonlinearity than if Method II or III is used. This can be understood from the fact that as the energy of the pion shower increases, more and more energy is deposited in the hadronic section of the calorimeter. In Method I, the signal from

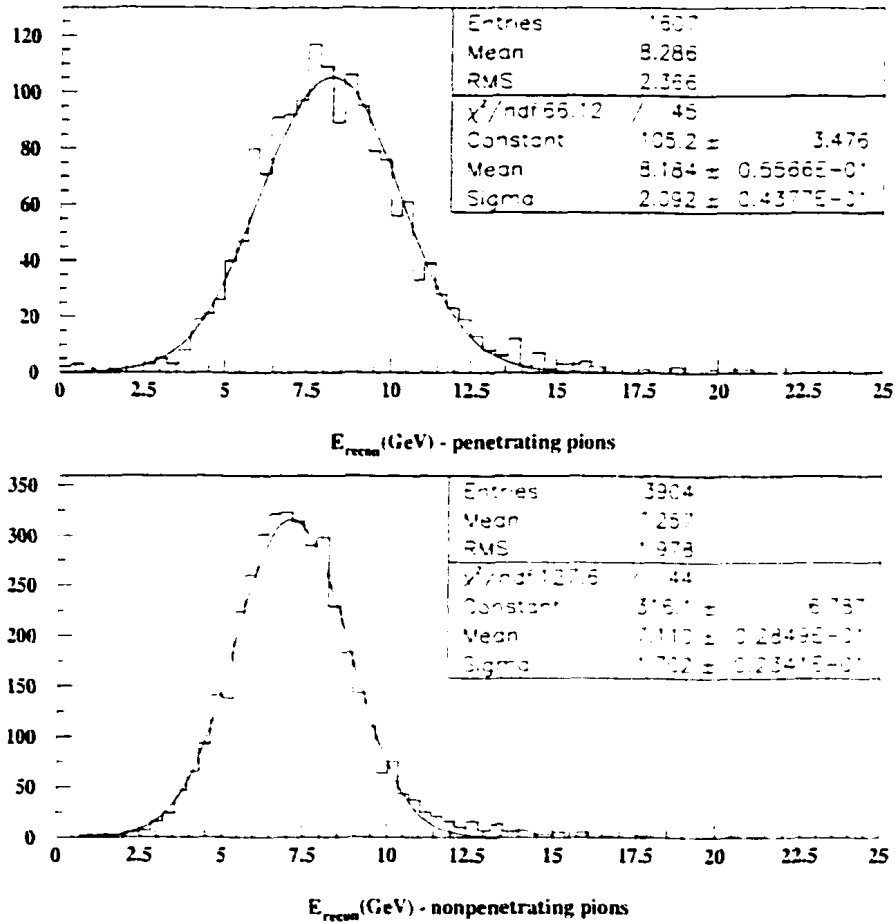


Figure 5.5: The reconstructed energy of penetrating (top) and nonpenetrating (bottom) pions when Method I is used to find the value of B .

the hadronic section of the calorimeter is "boosted" with respect to the signal from the electromagnetic section of the calorimeter.

Figure 5.7 shows the ratio of the reconstructed energy and the deposited energy as a function of the latter for all three different calibration methods. Each data point represents the mean value of the distribution of E_{recon} (Equation 5.1), where all pions, penetrating and nonpenetrating, have been taken into account. Each data set was fit with the function

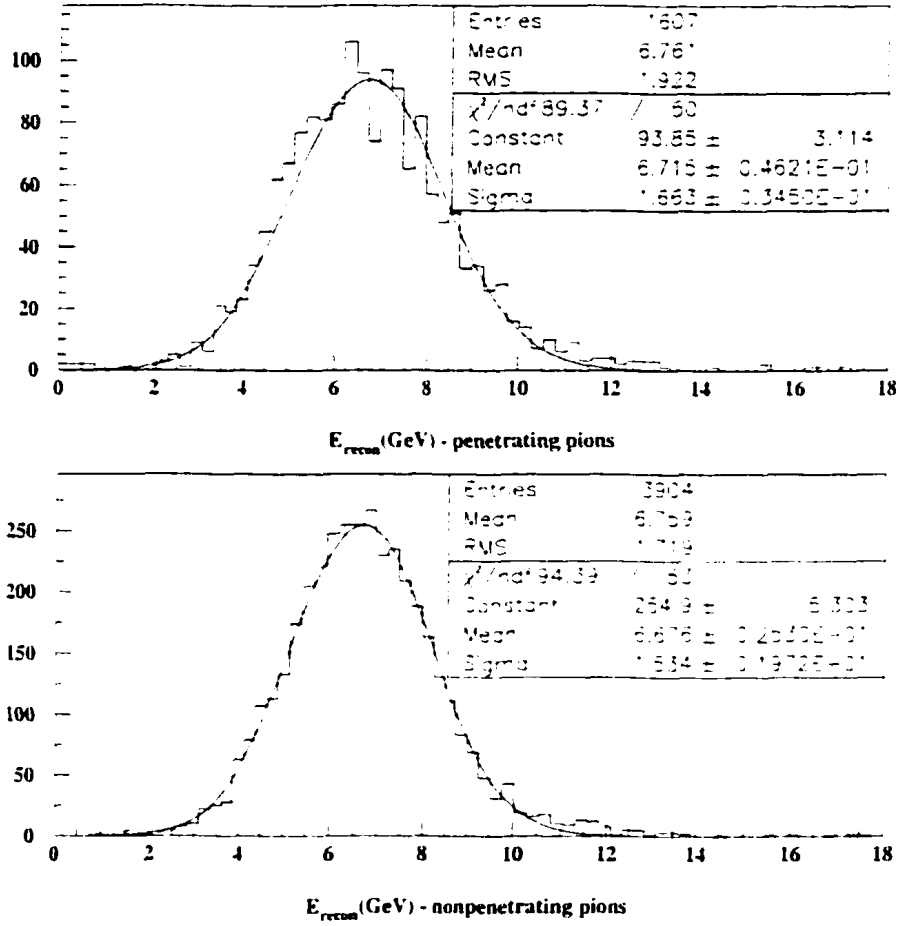


Figure 5.6: The reconstructed energy of penetrating (top) and nonpenetrating (bottom) pions when Method III is used to find the value of B .

$$\frac{\langle E_{\text{recon}} \rangle}{E_{\text{deposit}}} = k_1 + k_2 \ln E_{\text{deposit}} \quad (5.2)$$

The quantity k_2/k_1 , which is a measure of the signal nonlinearity, is $\sim 40\%$ larger when Method I is used as compared to Method III.

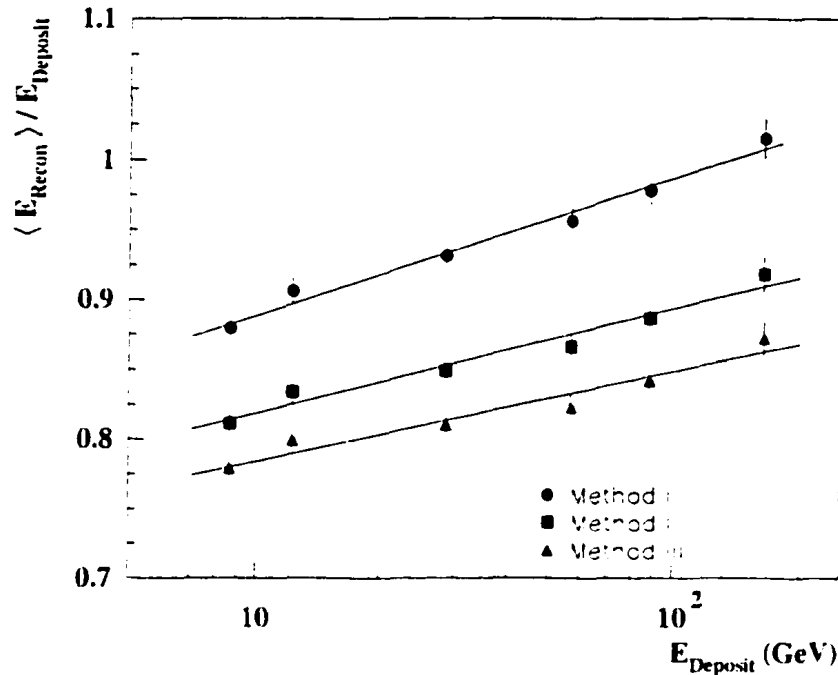


Figure 5.7: The ratio of the reconstructed energy and the deposited energy as a function of the energy deposited by pions showering in the CDF Plug Upgrade calorimeter. Results are given for the three calibration methods discussed in the text. The curves through the points are fits to the function in Equation 5.2.

5.2.3 Final energy reconstruction

As can be seen from Figure 5.7, the value of the reconstructed energy does not equal the value of the deposited energy (i.e., $\langle E_{\text{recon}} \rangle / E_{\text{deposit}}$, regardless of which method is used to set the energy scales of the hadronic section. In order to arrive at the correct value of the energy deposited by a pion in the calorimeter, one must multiply the reconstructed energy, found according to Equation 5.1, by an energy-dependent correction factor, which is simply the inverse of the curves shown in Figure 5.7. The details of this procedure are given in Appendix B.

5.2.4 Consequences for Jets

The consequences discussed in the previous section also have ramifications for the energy measurement of jets. In order to determine the effects of the three methods on the response of the calorimeter to jets, we used a Monte Carlo program previously developed as a part of calorimeter studies for the LHC [15]. In this approach, a jet is treated as a collection of particles, each with varying energy and charge. The energy of each jet particle is selected randomly according to a fragmentation function

$$D(z) = (\alpha + 1)(1 - z)^\alpha / z \quad (5.3)$$

where $D(z)$ is the probability that a jet fragment will end up with a fraction z of the jet energy, and α is a parameter. Fragmentation functions measured by CDF favor a value of $\alpha = 6$, which we therefore used in these simulations. The charge of each fragment was chosen randomly so that 33% of the time it was a neutral pion and 67% of the time a charged pion. For a jet of energy E_{jet} we randomly pulled n particles from the function in Equation 5.3 such that $E_{\text{jet}} = \sum_{i=1}^n E_i$ where E_i is the energy of each jet fragment. For each jet fragment with energy E_i , we randomly pulled an em and had signal, s^{em} and s^{had} , from the em and had signal distributions for a testbeam run of electrons (if the fragment was neutral) or pions (if the fragment was charged) whose beam energy was close to the jet fragment energy. For instance, for a 10 GeV neutral jet fragment, a signal s^{em} and s^{had} was pulled from the em and had section signal distributions for an 8 GeV testbeam run of electrons. The jet fragment was then attributed an em and had signal of $S_i^{em} = (10/8)s^{em}$ and $S_i^{had} = (10/8)s^{had}$ respectively. For a 10 GeV charged fragment, the same procedure would be followed, but the signals would be pulled from a pion run rather than an electron run. This process was repeated for each of the n jet fragments that made up the jet of energy

E_{jet} . The energy the calorimeter would have reconstructed for this jet then is simply

$$E_{\text{jet}}^{\text{recon}} = \left\langle \sum_{i=1}^n \frac{S_i^{\text{em}}}{A} + \frac{S_i^{\text{had}}}{B_{\text{I,II,III}}} \right\rangle. \quad (5.4)$$

The value of A is 128 cts/GeV, and the value of B depends on the method used (I, II, or III).

Figure 5.8 shows the calorimeter's response to jets in the energy range from 25-200 GeV using the three different calibration methods as a function of the jet energy. For each point, 10,000 jets were generated and the calorimeter's response to each jet was calculated as described above. As was the case for single pions, the slope of the curve for Method III is somewhat smaller than the slope of the curve for Method I. This illustrates that the nonlinearity effects described in Section 5.2.2.2 for single pions propagate into the energy measurement of jets.

5.2.5 Conclusions

We have compared three different methods of setting the hadronic section energy scale of a longitudinally segmented calorimeter. The merits of these methods have been studied with testbeam data from the CDF Plug Upgrade calorimeter. It turns out that one of the methods (the standard method used by CDF) introduces a number of undesirable side effects, such as an increased hadronic signal nonlinearity and a dependence of the reconstructed energy on the starting point of the hadron showers. These problems are a direct consequence of the noncompensating nature of the calorimeters. They can be avoided when a different calibration method is used.

5.3 CDF Central calorimeter studies

The same problems encountered when calibrating the Plug Upgrade calorimeter are also present for the Central CDF calorimeter. We have used Run I minimum

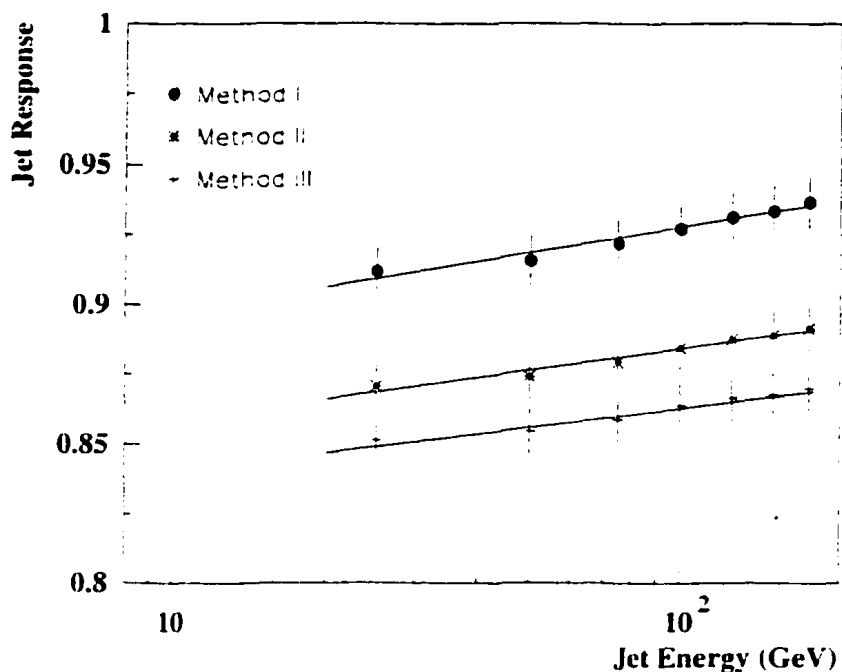


Figure 5.8: The jet energy response of the Plug Upgrade Calorimeter as found using the Monte Carlo program described in the text. The slope of the line fitting the response is larger when Method I is used than when Method III is used.

bias data to reproduce a testbeam environment in order to compare the effects of calibration Methods I and III in the Central calorimeter.

Ideally, one would use a clean testbeam of pions with well-defined momenta to determine the hadronic energy scale. The Central calorimeters were placed in a testbeam in 1985 and 1990, but data from these tests are no longer available or relevant. In the absence of testbeam data, one may use *in situ* data. We have used minimum bias data from Run I taken in 1994-95 to manufacture a “beam” of pions with well-defined momenta in order to study the effects of the calibration method in the Central calorimeter.

5.3.1 Run I minimum bias data

Particles' momenta are precisely measured by the tracking chamber inside the calorimeters, and one can assume that $\sim 90\%$ of the tracks seen in minimum bias data are pions. In order to select a sample of particles that would be suitable for our purpose, we made the following requirements.

- The sum of the total transverse energy $\sum E_T$ must be smaller than the center of mass energy of the $p\bar{p}$ collision. $\sqrt{s} = 1800$ GeV.
- The z -position of the primary vertex must be within 40 cm of $z = 0$.
- The missing energy, E_t , must be less than 20 GeV. This ensures rejection of events in which a cosmic ray passed through the detector at the same time as the pp collision.

For events which passed these cuts, tracks were selected using standard CDF tracking routines, TRKSEL and TRKSUN. These routines require hits to be present in two axial superlayers and one stereo superlayer of the CTC. A total of 17,960,043 tracks were recorded. Each of these tracks was extrapolated to the calorimeter. We call the tower that the track extrapolates to the "target" tower.

In order to choose high quality tracks, we applied the following track requirements:

- $|d_0| \leq 0.5$ cm,
- $|z_0 - z_{vtx}| \leq 5$ cm,
- $p_t \geq 0.3$ GeV/c,

where d_0 is the impact parameter of the track, z_0 is the value of closest approach to the beam axis, and z_{vtx} is the z position of the primary vertex.

With these requirements, we can be reasonably sure that the reconstructed track indeed corresponds to a charged particle. After the above requirements were applied,

7,550,255 tracks remained. We also eliminated tracks for which the energy deposited in the target electromagnetic tower plus the energy in the hadronic tower directly behind it was less than 10 MeV. This cut was meant to eliminate particles which did not escape the magnetic field and therefore did not deposit their energy in the calorimeter. It was also meant to cut particles which hit in the crack between calorimeter towers. We also cut tracks for which the energy in the target electromagnetic or hadronic tower was greater than 499 GeV.

Since we only wanted to study the Central calorimeter (not the Wall or Plug calorimeters), we required the track to hit the calorimeter within the eta range: $|\eta| \leq 0.66$. In order to further emulate the testbeam environment, we selected tracks which were isolated, i.e., particles for which no other tracks extrapolated to the 24 towers surrounding the target tower. When checking for tracks extrapolated to the surrounding 24 towers, we did not apply the above cuts or requirements. Finally, we selected tracks which hit the inner 36% of the target tower face area. It has been shown that there is little lateral leakage outside the target tower if the track hits the tower in the inner 36% of the tower face area [16].

In summary, we applied the following requirements to tracks:

- $|d_0| \leq 0.5$ cm,
- $|z_0 - z_{vtx}| \leq 5$ cm,
- $p_t \geq 0.3$ GeV/c,
- $E_{em}^{target} + E_{had}^{target} > 0.01$ GeV,
- $E_{em, had}^{target} < 499$ GeV,
- require track to hit calorimeter in eta range, $|\eta| \leq 0.66$,
- require no other track to hit calorimeter in 24 towers surrounding target tower,

- require track to hit inner 36% of tower face area.

With all of the above cuts and requirements, we were left with 409,634 “golden” tracks. We define the energy measured by the calorimeter as

$$E_{cal} = \sum_{i=1}^9 E_{em,i} + \sum_{i=1}^9 E_{had,i} \quad (5.5)$$

where $E_{em,i}$ is the energy in the i th electromagnetic calorimeter tower and $E_{had,i}$ is the energy in the i th hadronic calorimeter tower. The sum is over the 9 tower grid centered on the target tower. Figure 5.9 shows the quantity $\langle E_{cal}/p \rangle$ as a function of the momentum p for our golden track sample.

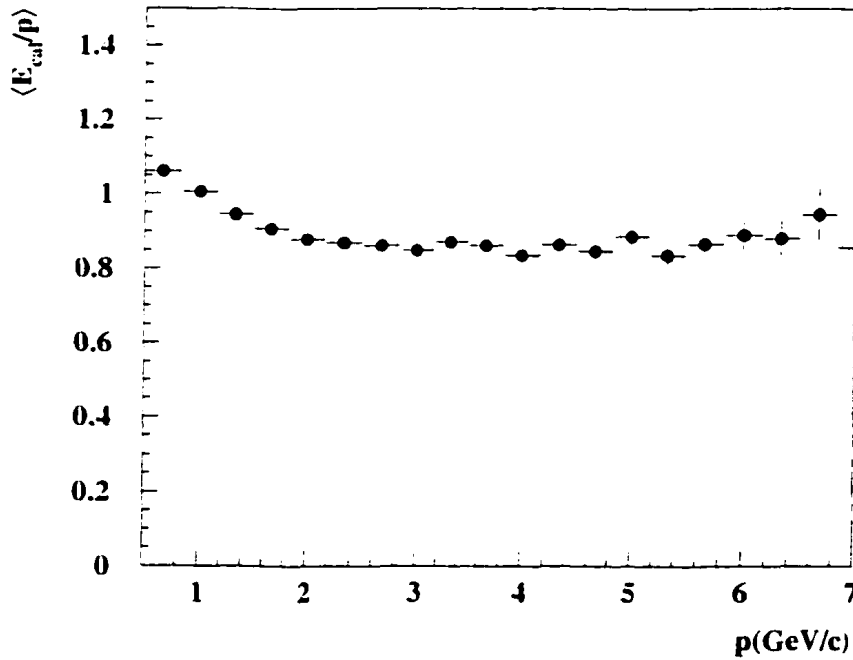


Figure 5.9: Ratio of the particle energy reconstructed by the calorimeter, E_{cal} , and the particle momentum measured with the tracking system, p as a function of p for isolated tracks hitting the Central calorimeter in the inner 36% of the target tower face. See text for details.

5.3.2 Background correction

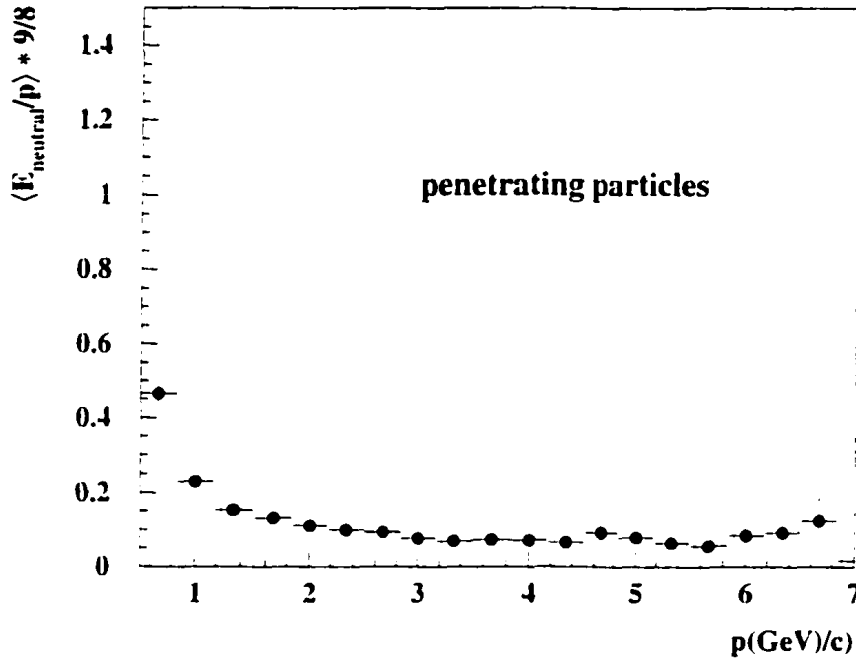


Figure 5.10: The quantity $9/8 \cdot \langle E_{neutral}/p \rangle$ is plotted vs the momentum. $E_{neutral}$ is the total energy in the 8 electromagnetic towers surrounding the target tower for tracks which penetrate the electromagnetic section without interacting. This quantity is an estimate for the average energy deposited in the calorimeter by neutral particles accompanying charged particles that produce golden tracks.

By using the isolation requirement as described above, one hopes to choose only particles which are not accompanied by other particles hitting the target tower or the 24 calorimeter towers surrounding the target tower. With the tracking system, however, it is only possible to identify charged particles. If a neutral particle were to accompany the particle producing the golden track (as in the case of a ρ^\pm decaying to a charged pion and a neutral pion) and hit the same calorimeter tower as the charged particle, there would be no sign of the accompanying particle in the tracking system, but the energy measured by the calorimeter would be larger than that produced by

the charged particle alone. In order to reproduce the testbeam environment, this neutral background must be accounted for.

We estimated this background in the following way. Out of the tracks remaining after applying all of the cuts and requirements described above, we selected tracks which deposited energy like a mip particle in the electromagnetic section, i.e., they penetrated the em section without undergoing a nuclear interaction. From these particles, there is no lateral leakage into the surrounding electromagnetic towers. The energy in the 8 surrounding electromagnetic towers then must be a result of accompanying neutral particles. We used this energy to estimate the average energy deposited in each electromagnetic calorimeter tower for all of our golden tracks.

We selected particles that deposited energy in the electromagnetic section like a mip as follows (see Figure 5.12). We defined a mip-like track as one in which the energy in the target electromagnetic tower was between 0.2 and 0.5 GeV and the energy in the 9 hadronic towers behind the target electromagnetic tower was greater than 1.0 GeV. We call these particles “penetrating” particles since they penetrate the electromagnetic section without strongly interacting.

Figure 5.10 shows, for penetrating particles, the mean energy in the 8 towers surrounding the target tower multiplied by 9/8 (since our energy definition includes a 9 electromagnetic tower sum) and divided by the momentum of the golden track, as a function of this momentum. In other words, we have plotted the quantity

$$\langle E_{neutral}/p \rangle = \left\langle \left[\sum_{i=1}^8 E_{em,i} * 9/8 \right] / p \right\rangle \quad (5.6)$$

where $E_{em,i}$ is the energy in the i th electromagnetic calorimeter tower and the sum is over the 8 electromagnetic towers surrounding the target tower.

Since we would like to measure the energy deposited in the calorimeter by *only* the golden charged track, we subtract $E_{neutral}$ from E_{cal} not only for penetrating particles but for *all* particles in our golden track sample. We define this quantity as

the corrected energy, E_{corr} :

$$E_{corr} = E_{cal} - E_{neutral}. \quad (5.7)$$

E_{corr}/p is shown as a function of p in Figure 5.11. For momenta larger than 1 GeV/c, this ratio amounts to ~ 0.8 almost independent of energy. Note that this correction for energy carried by neutral particles accompanying our gold tracks has eliminated the energy dependence observed before this correction was applied (Figure 5.9).

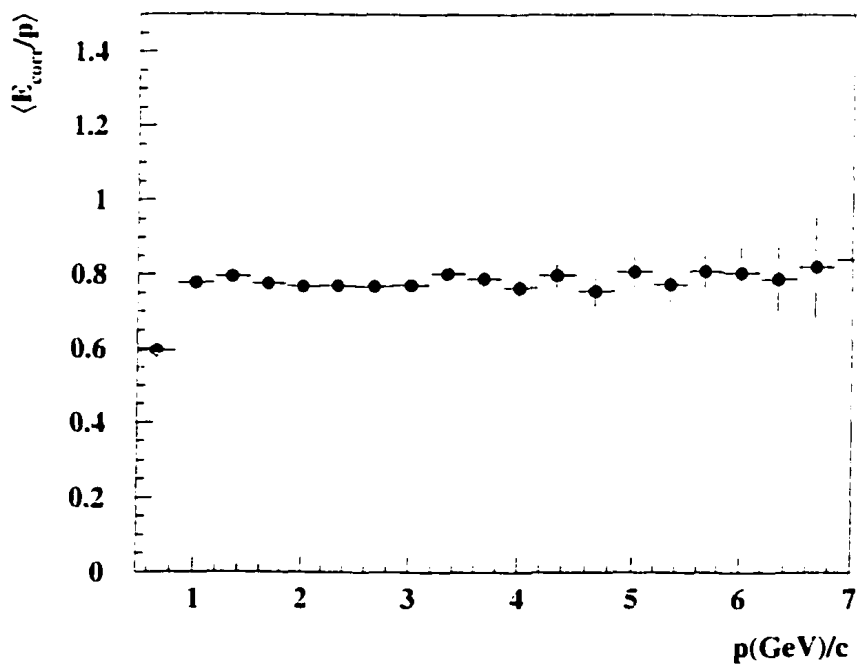


Figure 5.11: $\langle E_{corr}/p \rangle$ vs p for isolated tracks hitting the Central calorimeter in the inner 36% of the target tower face. E_{corr} is defined as $E_{cal} - E_{neutral}$. See text for details.

5.3.3 Comparison of calibration methods

We will now discuss the consequences of calibration methods I and III introduced in Section 5.2 when applied to the CDF Central calorimeter.

5.3.3.1 Method I

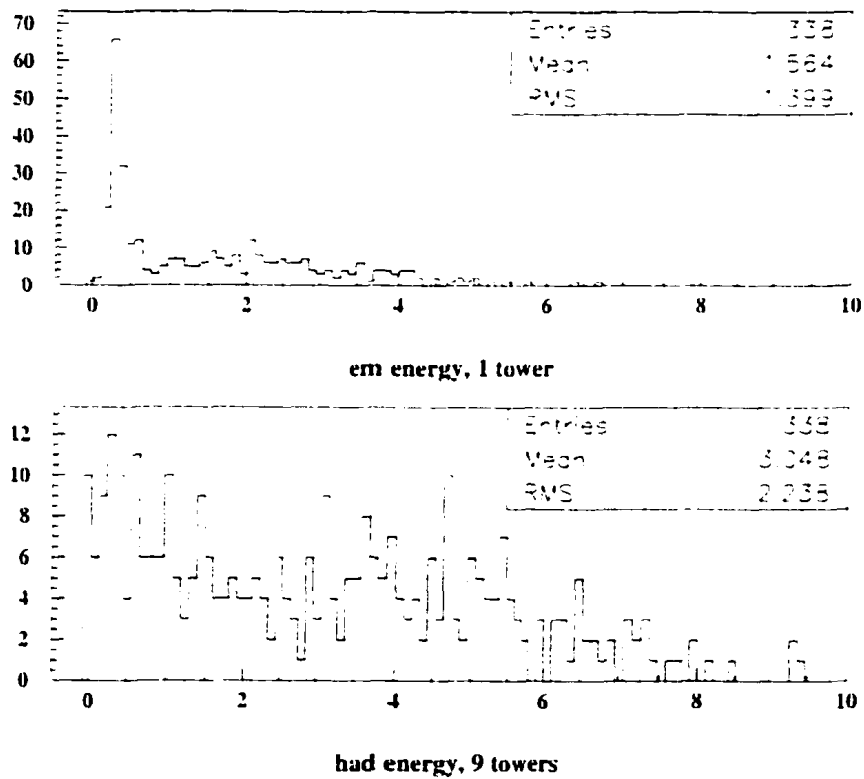


Figure 5.12: The energy in the target tower of the electromagnetic section (top) and the energy in the 9 hadronic towers behind the target tower (bottom). Shown are particles with momenta between 5 and 15 GeV/c. Penetrating particles are defined as those for which the energy in the target electromagnetic tower is between 0.2-0.5 GeV and the energy in the 9 hadronic towers is greater than 1.0 GeV. Nonpenetrating particles are those for which the energy in the target electromagnetic tower is greater than 0.7 GeV.

Figure 5.12 shows the energy in the target tower of the electromagnetic section and the energy in the 9 hadronic towers behind the target electromagnetic tower for

particles with $5 < p < 15 \text{ GeV}/c$. On the basis of these plots, we divided the sample of particles into “penetrating” and “nonpenetrating” particles.

We defined “penetrating” particles as described in Section 5.3.2, namely particles for which the energy in the target electromagnetic tower, E_{em}^{target} is between 0.2 and 0.5 GeV and the energy in the 9 hadronic towers behind the target electromagnetic tower, $\sum_{i=1}^9 E_{had,i}$ is greater than 1.0 GeV. Figure 5.12 shows the distribution of energy in the target electromagnetic tower and in the 9 hadronic towers behind the target electromagnetic tower. Nonpenetrating particles are defined as particles which do not penetrate the electromagnetic section without interacting. They begin showering in the electromagnetic section. If a particle deposited more than 0.7 GeV in the target electromagnetic tower, then we called it a nonpenetrating particle.

Figure 5.13 shows distributions of the quantity E_{corr}/p vs p for penetrating and nonpenetrating pions separately. E_{corr}/p is $\sim 12\%$ larger for penetrating pions than for the nonpenetrating ones. This is due to the fact that the energy scale of the hadronic section of the Central calorimeter was determined using Method I. Pions register a smaller signal in a noncompensating calorimeter than electrons of the same energy. Since pions were used to calibrate the hadronic section but *not* the electromagnetic section, the signal that nonpenetrating pions leave in the electromagnetic section is not sufficiently boosted. Thus the reconstructed energy of nonpenetrating pions is, on average, too small. It is important to note that *most* hadrons hitting the calorimeter *will* interact in the electromagnetic section. Most hadrons do not miraculously know to wait until they hit the hadronic section of the calorimeter to begin depositing significant amounts of their energy.

It should also be noted from Figure 5.13 that the value of E/p for penetrating pions is not 1. The energy scale of the hadronic section of the Central calorimeter was determined with 57.1 GeV penetrating pions [16]. For these 57.1 GeV pions, E/p was defined to be 1. For lower energy pions with momenta between 5 and 10 GeV/ c ,

the value of E/p is smaller than 1. This indicates a nonlinearity of the calorimeter's response which is due to the noncompensating nature of the hadronic section of the calorimeter. The same effect was observed in the Plug Upgrade Calorimeter (see Figure 5.7). The magnitude of the nonlinearity of the hadronic section of the Central calorimeter is in agreement with what we would expect based on the material composition of the device [17].

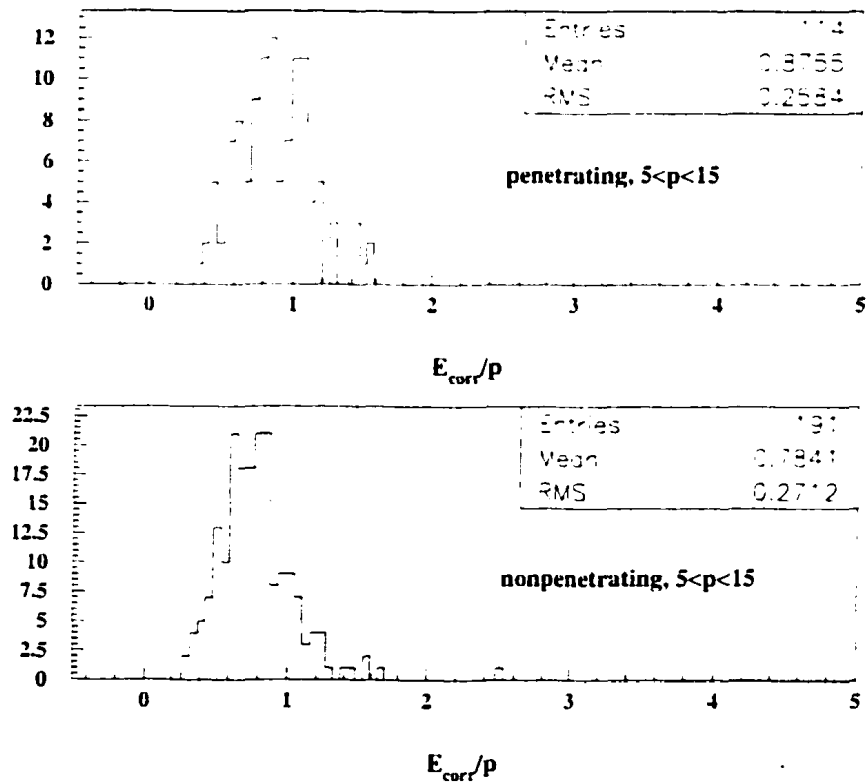


Figure 5.13: E_{corr}/p for penetrating and nonpenetrating pions when Method I is used. Shown are particles with momenta between 5 and 15 GeV/c. The means of the distributions differ by $\sim 12\%$. Note that most tracks are in the nonpenetrating category.

5.3.4 Method III

In order to establish Method III in the Central calorimeter, we need to determine a multiplicative factor, k that must be applied to the signals from the hadronic section in order equalize E_{cal}/p for penetrating and nonpenetrating pions. We have determined this factor, and it is shown in Figure 5.14 as a function of p of the golden track. Given our limited statistics, we do not see a significant p dependence of the k value. The value is $k = 0.81 \pm 0.04$.

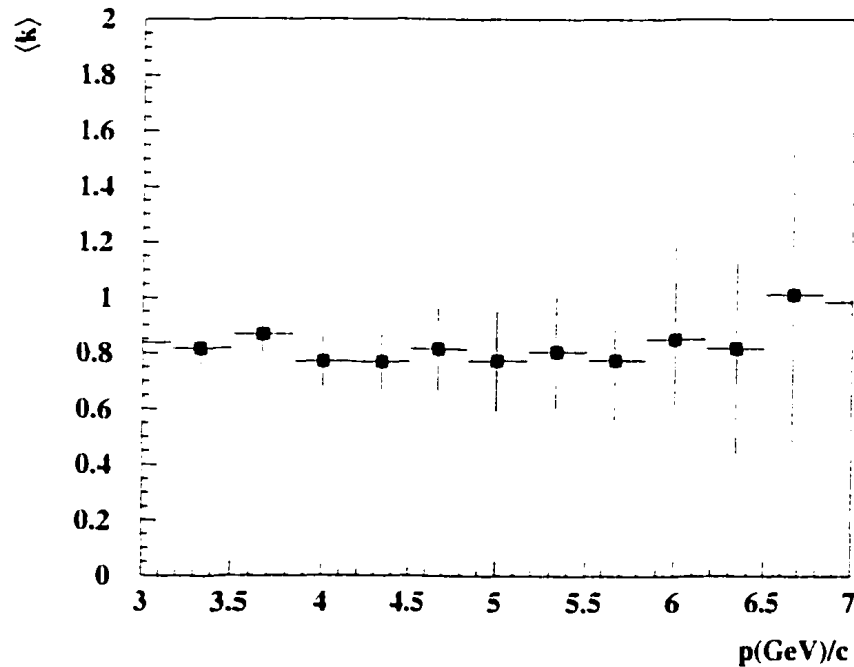


Figure 5.14: The factor, $\langle k \rangle$, that the hadronic section energy must be multiplied by in order to equalize E_{corr}/p for penetrating and nonpenetrating pions. $\langle k \rangle$ is constant over p .

When this factor is applied to the hadronic section energy, the quantity $E_{cal}/p - E_{neutral}/p$ is equal within the uncertainties for penetrating and nonpenetrating pions. This is shown in Figure 5.15. By using Method III, the dependence of the recon-

structed hadron energy on the starting point of the hadron shower is eliminated, as we saw earlier for the Plug Upgrade Calorimeter (see Figure 5.6).

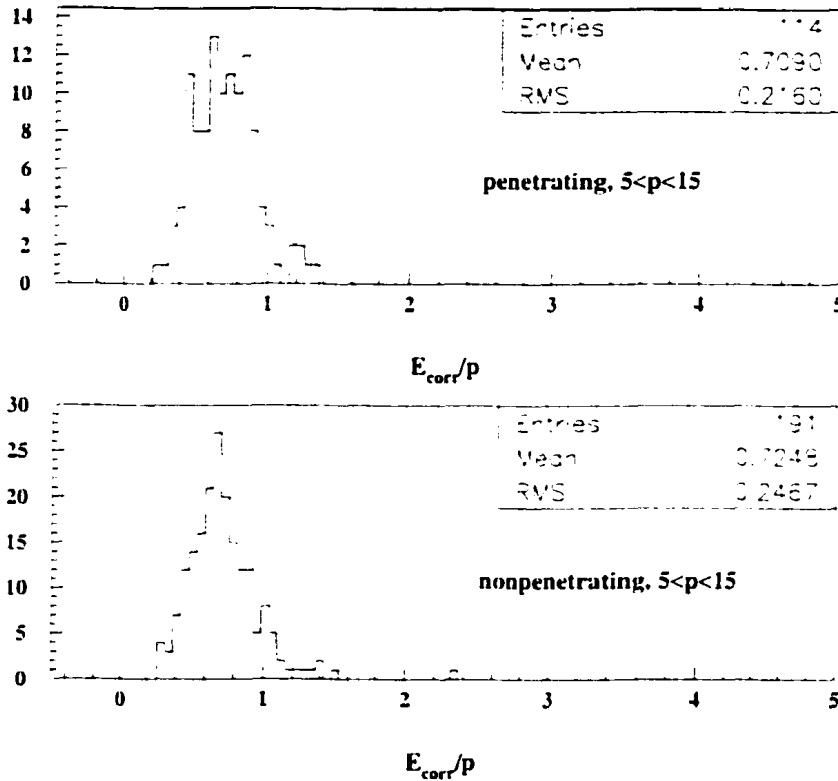


Figure 5.15: E_{corr}/p for penetrating and nonpenetrating pions when Method III is used. The plot only includes particles with momenta between 5 and 15 GeV/c. The means of the distributions are not significantly different given the statistical uncertainties.

5.4 Conclusions

We have presented two methods of determining the energy scale of the hadronic section of the Central calorimeter. We studied these two methods previously with Plug Upgrade testbeam data, and found that Method I introduces undesirable effects such as the dependence of the reconstructed energy of a hadron on the starting point of the hadron shower. We found the same effects in the Central calorimeter when

this calibration method was used. In particular, the reconstructed energy of hadrons with $5 < p < 15 \text{ GeV}/c$ which begin showering in the electromagnetic section of the calorimeter is systematically underestimated. Such particles carry most of the energy of jets at CDF. Using calibration Method III avoids this effect.

CHAPTER 6

JETS

"A scientific truth does not triumph by convincing its opponents and making them see the light, but rather because its opponents eventually die and a new generation grows up that is familiar with it." -Max Planck

6.1 Strong coupling constant

The fact that QCD is nonabelian and interactions between its gauge bosons are possible leads to two unique effects. As in QED, the coupling constant changes with the Q^2 (momentum transfer) of the interaction. The QCD coupling constant, $\alpha_s(Q^2)$, is given to order $\mathcal{O}(\alpha_s^2)$ by

$$\alpha_s(Q^2) = \frac{12\pi}{(33 - 2n_f) \ln \frac{Q^2}{\Lambda_{QCD}^2}} \quad (6.1)$$

with

$$\Lambda_{QCD}^2 = \mu^2 \exp\left(\frac{-12\pi}{(33 - 2n_f)\alpha_s(\mu^2)}\right) \quad (6.2)$$

where Q^2 is the momentum transfer (i.e., the energy of the probe) and n_f is the number of quark flavors (assumed to be six). Here, we see the difference between QED and QCD. In QED, as a bare electric charge is probed at higher and higher energies -corresponding to shorter and shorter distances - the strength of the electromagnetic coupling increases, but in QCD, α_s decreases with increasing Q^2 . At sufficiently high values of Q^2 , α_s becomes arbitrarily small, i.e., inside the proton, quarks are unbound. This is known as *asymptotic freedom* of the strong interaction.

The decrease of α_s with increasing Q^2 (small distance scale) implies an increase of α_s with decreasing Q^2 (large distance scale). This leads to the concept of *color confinement*, namely that quarks cannot exist as free particles. As two quarks are pulled apart, the potential energy between them becomes large enough that it becomes

energetically favorable to create a quark-antiquark pair from the vacuum, thus creating two separate hadrons. This process is known as *fragmentation* or *hadronization*. While confinement is still an experimental fact rather than a theoretical prediction, it is widely accepted since no free quarks or gluons have been observed in nature.

6.2 Hadronization

For $Q^2 \gg \Lambda_{QCD}$, the values of α_s are small, so that perturbation theory can be applied. For Q^2 of order Λ_{QCD} , α_s is large, and perturbation theory cannot be applied. Thus, semi-empirical models of hadronization have been developed. Here, we briefly describe the model known as the string model.

When a quark and antiquark are pulled apart, the color field between them is referred to as a “color string” or “color tube.” The potential between the quark and antiquark contains a term linear in the distance, r , separating the quark and antiquark.

$$V = kr. \tag{6.3}$$

Thus as the $q\bar{q}$ are separated, the potential energy between them rises linearly with r . At some separation (~ 1 fm), it takes less energy to create a $q\bar{q}$ pair from the vacuum and have two shorter strings than to continue the separation.

6.3 What is a jet?

The fragmentation process happens on the time scale of 10^{-23} seconds. Thus, quarks and gluons produced in high energy collisions hadronize immediately before travelling any significant distance away from the interaction point (i.e., before encountering the detector). They show up in the detector as a “spray” of hadrons which roughly follow the original direction of the quark or gluon. This collection of particles is called a jet. Thus, for an experimentalist, a jet can be thought of as simply

a collimated collection of charged and neutral hadrons emerging from the interaction point. Quark jets were first observed in e^+e^- collisions by the Mark-I Collaboration at SLAC in 1975 [18]. Gluon jets were first observed in 1979 by experiments at the e^+e^- collider PETRA at DESY [19]. The UA2 Collaboration at CERN observed the first jets at a $p\bar{p}$ collider in 1982 [20].

The process of quarks hadronizing into mesons and baryons which can be measured in a detector is typically described by a fragmentation function parametrized as follows

$$D(z) = N \frac{(1-z)^n}{z} \quad (6.4)$$

where $D(z)$ is the probability that a jet fragment will end up with a fraction z of the original parton energy and n and N are constants.

6.4 Measuring jets in high energy collisions

Usually, a jet is defined as the collection of particles that fall within a cone with opening angle R emerging from the interaction vertex. Typical values of R , when expressed in terms of an interval in η, ϕ space ($R = \sqrt{\Delta\eta^2 + \Delta\phi^2}$), range from 0.3-0.7. If the chosen R value is large, the cone may be contaminated with particles that have nothing to do with the fragmenting object. If R is small, some jet fragments may be located outside the cone. Fluctuations in the jet energy contained within the jet-defining cone form an irreducible component of the energy resolution of the jet detector.

High resolution hadron calorimetry will become increasingly important in the measurements of jets as the energy frontier is pushed to higher values of \sqrt{s} . Since high energy jets are more collimated than low energy jets, the limitations imposed by jet-defining algorithms decrease with increasing energy.

With current calorimeter technology, the requirements for high resolution hadron calorimetry, however, are exactly opposite of those needed for high resolution elec-

tromagnetic calorimetry [6] (energy measurement of electrons and photons). The ZEUS Collaboration currently operates the highest-resolution hadron calorimeter in the world [21], but pays a price for that with a marginal electromagnetic energy resolution: $\sigma/E = 18\%/\sqrt{E}$. Calorimeters being built for the LHC experiments emphasize excellent electromagnetic energy resolution, at the expense of hadronic resolution.

One solution which is being considered in the context of a possible (but unlikely) future linear e^+e^- collider, is a method called the *Energy Flow Method* (EFM). In this method, information from the calorimeter system is combined with that from an upstream tracker system. The momenta of the charged jet fragments, measured with high precision by the magnetic tracking system, serve as a first-order estimate of the jet energy. The calorimeter signals are used to obtain second-order corrections to that energy, caused by the neutral jet component (γ s, K^0 s and neutrons). With methods of this type, several LEP experiments improved the resolution of jets from Z -decay from $\sim 12\%$ to $\sim 9\%$. We have studied the merits of this method using the same testbeam data and a simulation very similar to that described in Section 5.2.4.

Using the method described in Section 5.2.4, we first built “libraries” of jet signal distributions, S_{jet} (equivalent to $E_{\text{jet}}^{\text{recon}}$ in Equation 5.4), for jets of a variety of energies, ranging from 30-1000 GeV. For a given jet of a certain fixed energy, e.g., 100 GeV, the experimental pion signal distributions were used (again in the same way) to determine the “measured” calorimeter energy for individual charged jet fragments, E_{charged} . The neutral jet component of the 100 GeV jet, E_{neutral} , was found by subtracting E_{charged} from the average value of the S_{jet} distribution for 100 GeV jets, i.e., $E_{\text{neutral}} = \langle S_{\text{jet}} \rangle - E_{\text{charged}}$. The energy found with the EFM for this particular jet was calculated as

$$E_{\text{EFM}} = \sum_{i=1}^m E_i + E_{\text{neutral}} \quad (6.5)$$

where $E_i (i = 1, 2, \dots, m)$ represent the *exact* energies of the chosen *charged* jet frag-

ments.

The relative effect of the EFM on the jet energy resolution was determined by comparing the fractional widths of the S_{jet} and E_{EFM} distributions. The improvement of the jet energy resolution found this way is shown in Figure 6.1. Details of this study are described in a paper that was recently accepted for publication in *Nuclear Instruments and Methods in Physics Research* [22]. A preprint of this paper is contained in Appendix C.

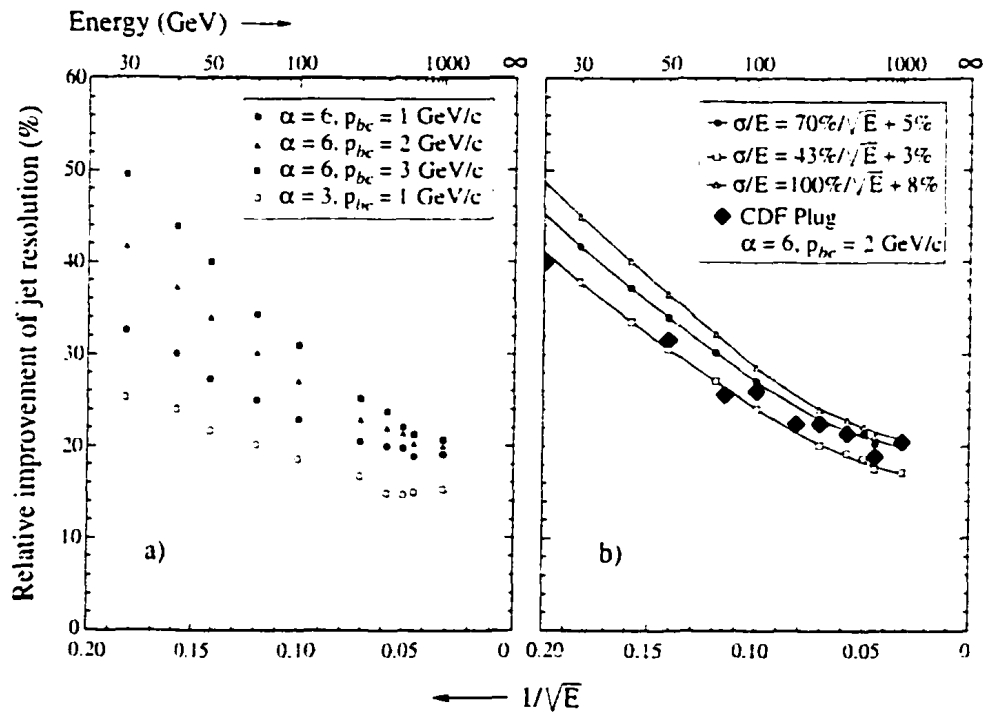


Figure 6.1: Relative improvement of the jet resolution by using the Energy Flow Method, as a function of the jet energy. Results of Monte Carlo simulations with different parameter choices. The black diamonds were obtained using testbeam data from the CDF Plug Upgrade calorimeter. See text for details.

6.4.1 Conclusions

The experimental data and the results of simulations both show that the EFM offers an improvement in the jet energy resolution of $\sim 30\%$. Poor calorimeter systems benefit more than good calorimeter systems, and a strong magnetic field also helps.

It is also important to note that the EFM does not work as well at high energies as at low energies. At high energies, the hadronic calorimeter resolution is dominated by fluctuations that result from the different calorimeter response to em and non-em energy deposit. These fluctuations are not addressed, nor cured by the EFM.

CHAPTER 7
SEARCH FOR TWO-JET DECAY OF THE W AND Z BOSONS AT THE
FERMILAB TEVATRON

7.1 Introduction

The W and Z bosons have been extensively studied at CDF through their leptonic decay modes, $W \rightarrow e\nu, \mu\nu$ and $Z \rightarrow ee, \mu\mu$. Such decays produce a clean and easily recognizable signature in the detectors. The hadronic decay of the W and Z , however, has been observed at CDF in only two very specific cases. The hadronic decay of the W has been identified in top quark samples [23], and the specific decay channel, $Z \rightarrow b\bar{b}$, has been observed in high P_T muon data samples [24]. It would be useful to extend these studies and identify W/Z hadronic decays in a more general way, namely in a sample of dijet events. While it is not possible to identify hadronic decays of W 's and Z 's from such an event sample on an event-by-event basis, it should be statistically possible to identify these decays since the QCD background is intrinsically a smooth function of the dijet invariant mass. Identifying a W/Z mass peak above the QCD background would serve several purposes.

First, such a peak would provide an important handle for understanding the jet energy scale. The jet energy scale has been determined in the past (for the top mass measurement, for example) by using samples of events in which a jet appears with a prompt photon or a Z and performing a "jet-photon balancing" or " Z -jet balancing" procedure [25, 26, 27]. Identifying the W/Z peak in the dijet invariant mass spectrum would provide a very clean method of directly determining the jet energy scale, since the W and Z masses are known to great precision. Furthermore, an ability to identify W 's and Z 's in the jet-jet invariant mass spectrum would truly indicate the ability to do "jet mass spectroscopy" at hadron colliders. This could provide a means for looking

for new particles which decay hadronically or which decay into W 's and Z 's (e.g., the Higgs boson, if $m_H > 2m_W$). Since the branching ratio for hadronic decay of the intermediate vector bosons is much larger than for leptonic decay, there is also a better chance of identifying a rare process involving these massive particles through hadronic decay channels as opposed to leptonic ones.

During Tevatron Run IC, a low-threshold dijet trigger was used to record 1.9 pb^{-1} of data. Approximately 3 million two-jet events were recorded in which the E_T of each jet was greater than 12 GeV. These data were previously used to search for hadronic W/Z decays in the jet-jet invariant mass distribution as described in [28]. Here, we review relevant background information and repeat the analysis using a new absolute jet energy scale correction.

7.2 UA2 Result

The UA2 experiment reported a peak in the dijet invariant mass spectrum, above the smooth QCD background [29]. The location of the peak corresponded nicely with the W and Z masses.

The $4.7 \pm 0.2 \text{ pb}^{-1}$ sample of data used in the analysis was collected with a two-level central dijet trigger. At the first trigger level, energy was summed over 90° in ϕ . Two such sums at opposite azimuth, each with $E_T > 17 \text{ GeV}$ (for the “low mass trigger”) or $E_T > 13 \text{ GeV}$ (for the “very low mass trigger”) and in coincidence with a beam-beam interaction (determined by TOF detectors) were required. At the second trigger level, jet E_T was determined with a rectangular window of size $\Delta\theta \times \Delta\phi = 70^\circ \times 75^\circ$. Two such jets at opposite azimuth (within 30°) and with $E_T > 13 \text{ GeV}$ (for the “low mass trigger”) or $E_T > 10 \text{ GeV}$ (for the “very low mass trigger”) were required.

No track reconstruction was performed, and only calorimeter information was readout in order to keep the readout time and event size small. With the “low mass trigger” and “very low mass trigger,” 4.66 pb^{-1} and 0.58 pb^{-1} were collected,

respectively. A jet algorithm using a cone size of 0.8 was applied to all events passing the Level 2 trigger, and the jets in each event were ordered according to decreasing E_T .

The following offline requirements were applied to events passing the Level 2 trigger:

- $-200 \text{ mm} < z < 200 \text{ mm}$ where z is the longitudinal event vertex position. The event vertex was determined by the TOF detector.
- $|\cos\theta_{1,2}| < 0.6$ where $\theta_{1,2}$ are the polar angles of jet 1 and 2.
- $E_T^3 < 20 \text{ GeV}$ where E_T^3 is the E_T of the third jet. This requirement rejects events with more than 2 jets.
- $f_{em}^1 < 80\%$ or $f_{em}^2 < 80\%$ where $f_{em}^{1,2}$ are the electromagnetic energy fractions of the leading two jets. This requirement rejects $Z \rightarrow ee$ events.
- $f_{em}^{1,2} > 20\%$ in order to reject events in which the jets might not be completely longitudinally contained in the calorimeter. The UA2 calorimeter had a depth of $\sim 6.5\lambda_0$.
- $m_{JJ} > 40 \text{ GeV}/c^2$ where m_{JJ} is the invariant mass of the two leading jets.

After all cuts are applied, there were $3.6 \cdot 10^6$ and $1.4 \cdot 10^6$ events remaining for the “low mass” and “very low mass” triggers, respectively. A function of the form

$$m^{-\alpha} \cdot e^{-\beta \cdot m} \cdot e^{-\gamma \cdot m^2} \quad (7.1)$$

was used to fit the dijet invariant mass spectrum in the range $48 < m_{JJ} < 300 \text{ GeV}/c^2$. The fit quality was $\chi^2 = 163$ for 124 degrees of freedom. The fit quality was improved significantly, $\chi^2 = 97.5$ for 109 degrees of freedom (d.o.f.), when the range $70 < m_{JJ} < 100 \text{ GeV}/c^2$ was excluded from the fit (see Figure 7.1a). When the

spectrum was fit with the background function (7.1) and a signal function consisting of two Gaussian distributions with the W mass, the mass resolution and the signal size N as free parameters, then $\chi^2 = 114$ for 121 d.o.f. The signal consisted of 5618 ± 1334 events with a statistical significance of 4.2σ . The background-subtracted signal is shown in Figure 7.1b along with the overall signal fit and the contributions from the W and Z separately.

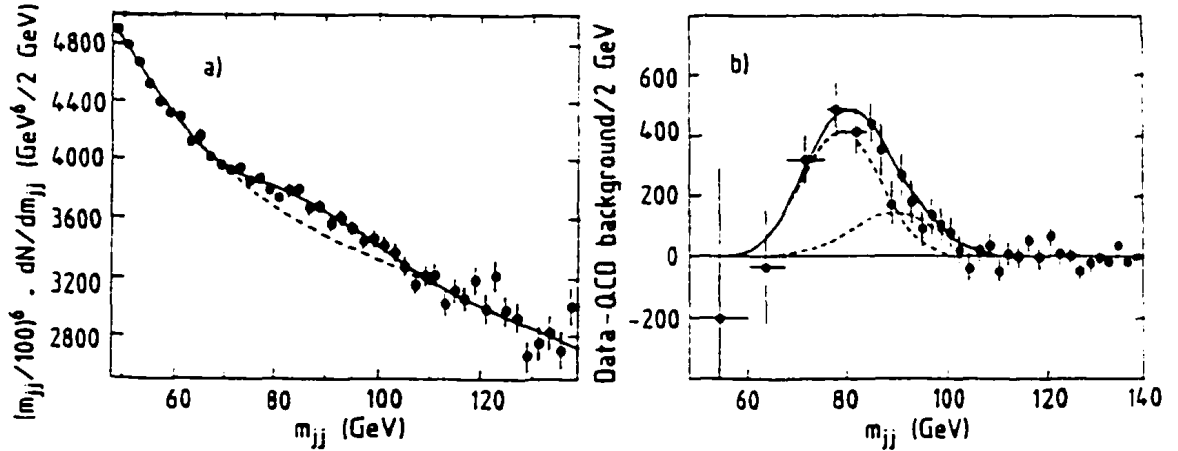


Figure 7.1: The signal $W, Z \rightarrow jets$ seen by UA2. The signal shown consists of 5618 ± 1334 events.

7.3 CDF Data

The dijet cross section is very large at low dijet masses. At the end of Run IC, half of the CTC was turned off due to a broken wire. Since tracking readout tends to be the prohibitively slow factor in taking data at high rates, and since calorimeter information, not tracking, is the crucial information for this analysis, a low threshold unprecaled dijet trigger was ideal for this running period.

The low threshold dijet trigger used in this analysis consisted of the following. At the first trigger level, at least one CEM tower and at least one CHA tower (independently) with $E_T > 4 \text{ GeV}$ were required. At the second trigger level, a primitive

clustering algorithm was applied. A cluster required a seed tower with $E_T > 3$ GeV. All adjacent towers with $E_T > 1$ GeV were included in the cluster. Two central jets with $E_T > 12$ GeV were required. At the third and final trigger level, a more extensive clustering algorithm was used and the Level 2 requirements were re-required. A total of 1.9 pb^{-1} was taken with this trigger. This is a much larger data sample than the entire Run I JET_20 sample ($\mathcal{L}/\text{prescale} = (19.1/500)\text{pb}^{-1}$ for Run IA and $(84.1/1000)\text{pb}^{-1}$ for Run IB).

7.4 Signal Expectations

CDF has measured the production cross section of W and Z bosons times the leptonic branching ratios. According to [30].

$$\sigma \cdot B(W \rightarrow e\nu) = 2.49 \pm 0.12 \text{ nb} \quad (7.2)$$

$$\sigma \cdot B(Z \rightarrow l^+l^-) = 0.231 \pm 0.012 \text{ nb}$$

at $\sqrt{s} = 1800$ GeV. The leptonic branching ratios of the vector bosons are well determined:

$$B(W \rightarrow e\nu) = 10.68 \pm 0.12\% \quad (7.3)$$

$$B(Z \rightarrow l^+l^-) = 3.3658 \pm 0.0023\%$$

Thus, the production cross sections for W and Z bosons at $\sqrt{s} = 1800$ GeV are 23.1 nb and 6.86 nb, respectively. Given the well-measured hadronic branching ratios

$$B(W \rightarrow jets) = 67.96 \pm 0.35\% \quad (7.4)$$

$$B(Z \rightarrow jets) = 69.91 \pm 0.06\%,$$

the cross section times hadronic branching ratios are

$$\sigma \cdot B(W \rightarrow jets) = 15.84 \pm 1.15\text{nb} \quad (7.5)$$

$$\sigma \cdot B(Z \rightarrow jets) = 4.8 \pm 0.36\text{nb}.$$

With no kinematical cuts and 1.9 pb^{-1} , we expect 30096 ± 2185 W events and 9120 ± 684 Z events.

The trigger requires that the two highest E_T jets be central jets, i.e., $|\eta_{1,2}| < 1.1$. Also, since many W 's and Z s produced in $p\bar{p}$ collisions at $\sqrt{s} = 1800 \text{ GeV}$ are produced at rest or nearly at rest, we required (offline) that $\cos \Phi < -0.4$ ($\Phi > 113^\circ$) where Φ is the angle between the two leading jets in E_T . In order to measure the effects of these two kinematical cuts, we generated 10,000 W and 10,000 Z events using PYTHIA. We forced the bosons to decay to two quarks and imposed the requirements

- $|\eta_{1,2}| < 1.1$
- $\cos \Phi < -0.4$

on the generated values of $\eta_{1,2}$ and Φ (no detector simulation was used). We found the efficiency to be 17.1% for W events and 18.4% for Z events.

Since we are interested in events with only two jets, we also require (offline) $E_T^3 < 10 \text{ GeV}$, where E_T^3 is the transverse energy of the jet with the third highest raw (no jet corrections) E_T . We assume this requirement is independent of the requirements on $|\eta_{1,2}| < 1.1$ and $\cos \Phi < -0.4$. According to CDF's measurement [31], the cross section for $W + \geq 1$ jets where the jet has energy greater than 15 GeV corrected E_T ($\sim 10 \text{ GeV}$ uncorrected or raw E_T) is $2.6 \pm 0.6 \text{ nb}$. The efficiency of the cut on E_T^3 then is $84 \pm 4\%$ for W 's. According to [32], the cross section for $Z + 1$ jet is $1.29 \pm 0.21 \text{ nb}$. The efficiency for Z s of the cut on E_T^3 then is $73 \pm 5\%$.

Assuming the requirements on $|\eta_{1,2}| < 1.1$ and $\cos \Phi < -0.4$ are independent of the requirement on E_T^3 , then the event selection efficiencies for W 's and Z s are $14.4 \pm 0.7\%$ and $13.4 \pm 0.9\%$, respectively. A summary of event selection efficiencies (i.e., acceptances) is given in Table 7.1.

Using the combined efficiency quoted in the last column of Table 7.1, we expect a total of 4333 ± 378 W events and 1222 ± 123 Z events when all three requirements

Table 7.1: Summary of efficiencies.

| | $ \eta_{1,2} < 1.1$ $\cos \Phi < -0.4$ | $E_T^3 < 10 \text{ GeV}$ | Combined |
|-----|--|--------------------------|------------------|
| W | 17.1% | $84 \pm 4\%$ | $14.4 \pm 0.7\%$ |
| Z | 18.4% | $73 \pm 5\%$ | $13.4 \pm 0.9\%$ |

($|\eta_{1,2}| < 1.1$, $\cos \Phi < -0.4$, $E_T^3 < 10 \text{ GeV}$) are applied. We look for the two signals as an excess of events, including both W and Z events (5556 ± 398 events), above the smooth QCD dijet background.

7.5 Central Calorimeter Jet Corrections

In Run I, CDF established a routine, known as JTC96, that performed “standard” jet corrections. The corrections included (1) a relative correction, f_{rel} , which corrected for the η response of the calorimeter relative to the central region (2) an absolute energy scale correction, f_{abs} , (3) an underlying event correction UE , and (4) an out-of-cone correction, OC . These corrections were applied as follows:

$$P_T(R) = P_T^{raw}(R) \cdot f_{rel}(R) \cdot f_{abs}(R) + UE(R) - OC(R) \quad (7.6)$$

where R is the jet cone size. A summary of these corrections is given in [27]. The particular correction we are concerned with is f_{abs} , the absolute energy scale correction. The method used to establish this correction in Run I is described in [33]. In short, the QFL calorimeter simulation was “tuned” to reproduce certain calorimeter signal distributions from testbeam and *in situ* data [34]. Jets were generated with SETPRT

(using ISAJET routines) and sent through QFL. The absolute jet correction was

$$f_{abs}(R) = \left\langle \frac{P_T^{\text{parton}}}{P_T^{\text{jet}}} \right\rangle \quad (7.7)$$

where P_T^{parton} is the true generated parton energy and P_T^{jet} is the estimate (from QFL) of what the measured energy would have been had the jet actually deposited its energy in the calorimeter. The absolute correction is given as a function of the cone size R because P_T^{parton} was defined as the sum of all daughter particles (from the original parton) that fell into a jet of cone size R . This process was repeated for 60 bins from 0-600 GeV/ c P_T^{jet} . For each bin, the mean of the P_T^{parton} distribution was plotted as a function of the mean of the P_T^{jet} distribution. The resulting curve was parametrized, and the parameterization was used in JTC96.

In these simulations, the hadronic energy scale was set according to what is referred to as “Method I” in [36]. However, in [35] and [36], another method of setting the energy scale of the hadronic section of the calorimeters (“Method III”) was presented. We have used this new energy scale to establish a new absolute jet energy scale correction. Here, we describe the procedure we used to establish this new correction. Our method is based on the calorimeter signals recorded for particles with well determined four vectors (from Run IB minimum bias data). We used these signals to reconstruct the signals of simulated jets. Calibration constants are chosen so as to avoid biases based on starting points of showers, the underlying philosophy of Method III.

Jets were generated according to the method described in [36]. With this method, a jet is treated as a collection of particles, each with varying energy and charge. For a jet of energy E_{jet} we used the fragmentation function

$$D(z) = (\alpha + 1)(1 - z)^\alpha / z \quad (7.8)$$

where $D(z)$ is the probability that a jet fragment will receive a fraction z of the

parton's momentum and α is a parameter (we used $\alpha = 6$) to randomly select n jet fragments with energy $E_i = E_{\text{jet}} \cdot z$ such that $E_{\text{jet}} = \sum_{i=1}^n E_i$. The charge of each fragment was chosen randomly so that 33% of the time it is a neutral pion and 67% of the time a charged pion.

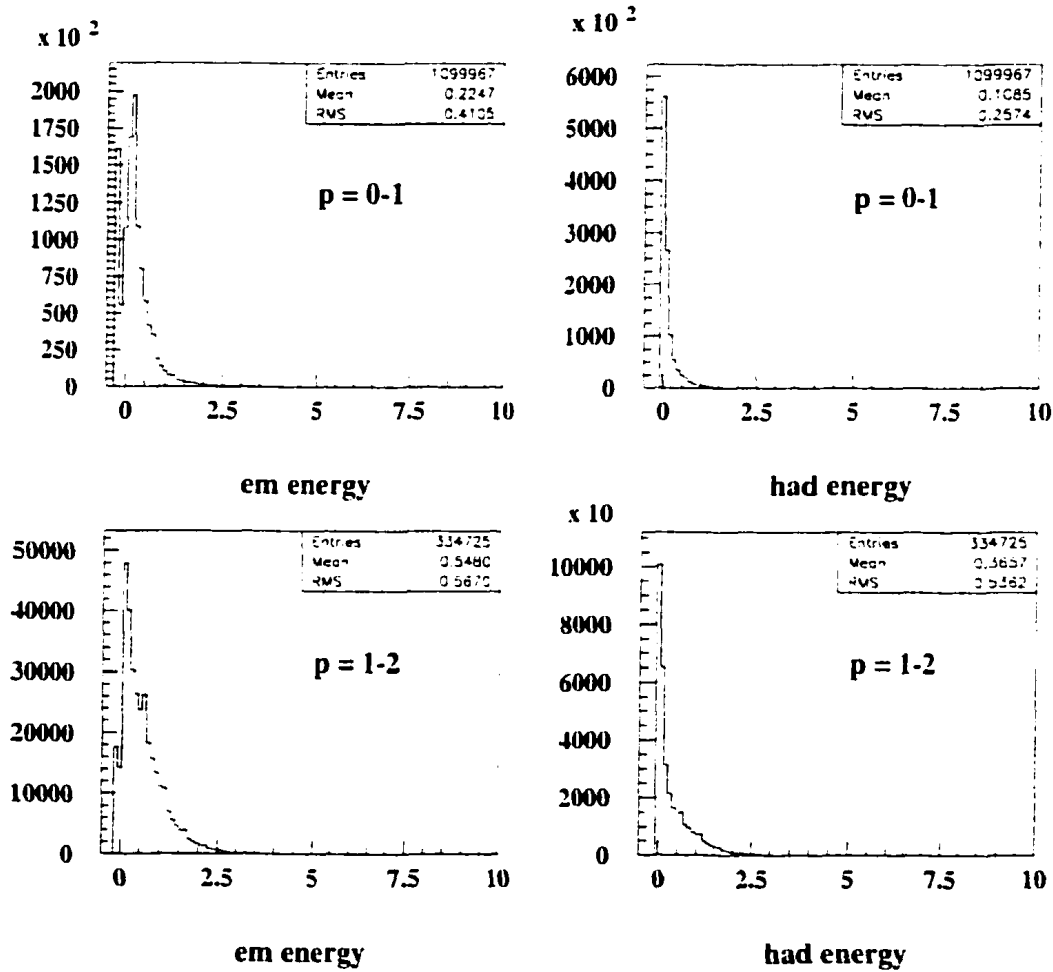


Figure 7.2: Central calorimeter signal distributions obtained using isolated tracks from Run IB minimum bias data. Signal distributions are shown separately for the electromagnetic and hadronic sections for tracks with momenta in the 0-1 GeV/c range and 1-2 GeV/c range. See text for details.

Figures 7.2, 7.3, and 7.4 show calorimeter signal distributions obtained from isolated hadrons in Run IB minimum bias data. Signal distributions from the electro-

magnetic and hadronic sections are shown separately for hadrons with varying momenta (measured by the tracking system). The following requirements were applied to tracks in order to make the plots.

- $|d_0| \leq 0.5$ cm, $|z_0 - z_{vtx}| \leq 5$ cm, $p_t \geq 0.3$ GeV/ c . These requirements were applied in order to choose high-quality tracks. With these requirements, we can be reasonably sure that the reconstructed track corresponds to a charged particle.
- $E_{em,had}^{target} < 499$ GeV. This requirement eliminated tracks for which the energy in the target (the calorimeter tower the track extrapolated to) em or hadronic tower was greater than 499 GeV.
- Tracks were required to hit the calorimeter in the eta range, $|\eta| \leq 0.66$ since we are only interested in tracks which hit the Central calorimeter.
- We required that no other track hit the calorimeter in the 24 towers surrounding the target tower in order to select isolated tracks.

For each charged jet fragment, an electromagnetic e^{em} and hadronic e^{had} signal was randomly pulled from these distributions according to the jet fragment's energy. For example, for a 1.8 GeV charged jet fragment, an electromagnetic and hadronic signal was randomly pulled from the distributions with measured hadron momenta $p = 1 - 2$ GeV/ c . The jet fragment was then attributed an electromagnetic and hadronic signal of $E_i^{em} = (1.8/1.5)e^{em}$ and $E_i^{had} = (1.8/1.5)e^{had}$, respectively. Compared to charged jet fragments, the calorimeter energy measurement of neutral fragments (π^0 's and γ 's) is quite precise. We therefore use the energy of neutral fragments exactly as they come from the fragmentation function.

This process was repeated for each of the n jet fragments that made up the jet of energy E_{jet} . The energy the calorimeter would have reconstructed for this jet, E_{recon}

then is simply

$$E_{\text{jet}}^{\text{recon}} = \left\langle \sum_{i=1}^n E_i^{\text{em}} + E_i^{\text{had}} \cdot k \right\rangle \quad (7.9)$$

where k is the factor used to recalibrate the hadronic energy scale according to “Method III.” The jet signal distributions that result from these simulations are shown in Figure 7.5. A plot of the jet response ($jet = \langle E_{\text{jet}}^{\text{recon}} \rangle / E_{\text{jet}}$) vs E_{jet} for Method I, jet_I , and Method III, jet_{III} is shown in Figure 7.6.

The new absolute jet energy correction is then

$$E_{\text{jet}}^{\text{corr}} = E_{\text{jet}}^{\text{raw}} \cdot 1/jet_{III} \quad (7.10)$$

where $E_{\text{jet}}^{\text{raw}} = E_{em} + k \cdot E_{had}$ and $k = 0.81$.

7.6 Initial search procedure

Figure 7.7 shows the jet-jet invariant mass spectrum in the energy range from 30-100 GeV/c^2 . For masses greater than 50 GeV/c^2 , the distribution is, in first approximation, reasonably exponential. We studied how well the distribution is described by an exponential function by determining the quality of an exponential fit involving four points at low mass ($M_n, M_{n+1}, M_{n+2}, M_{n+3}$) and 21 points ranging from $M_n + 23 \text{ GeV}/c^2$ to $M_n + 42 \text{ GeV}/c^2$. The χ^2 values of these fits (for 23 degrees of freedom) are plotted as a function of M_n in Figure 7.8.

The onset of the trigger inefficiency manifests itself as a sudden increase in the χ^2 value for $M_n < 55 \text{ GeV}/c^2$. The increase in χ^2 values in the range $60 < M_n < 80 \text{ GeV}/c^2$ correlates with an excess of events that is observed in this mass range when fits with $M_n = 56, 57, 58$ (which have a very good χ^2) are considered. The excess above the exponential background is shown in Figure 7.9a for the fit with $M_n = 57 \text{ GeV}/c^2$. There seems to be a peak that contains a total of $\sim 8,000$ events, centered around $m_{jj} = 67 \text{ GeV}/c^2$.

When the jet corrections described in Section 7.5 were applied and the above analysis was repeated, the excess of events above the exponential background shifted to higher mass values and increased to $\sim 12,000$ events. The results are shown in Figure 7.9b. The excess was fit with the sum of two Gaussian distributions, with excellent results. The difference between the two means and the ratio of the widths of the two gaussians were fixed in the fit to $10.8 \text{ GeV}/c^2$ and 1, respectively. All other parameters in the fit were left free. The dotted curves in Figure 7.9b represent the two Gaussians, and the solid curve is the sum of the two. The χ^2 value of this fit is 19.2 for 22 degrees of freedom. The two Gaussians are centered around 78.0 and $88.8 \text{ GeV}/c^2$, respectively. According to the fit, the peak consists of 9000 ± 1500 hadronically decaying W 's and 3500 ± 1500 Z 's. This puts the production ratio $\sigma(p\bar{p} \rightarrow Z) \cdot B(Z \rightarrow jets)/\sigma(p\bar{p} \rightarrow W) \cdot B(W \rightarrow jets)$ to a value somewhere between 0.2 and 0.5. This ratio is, in first approximation, independent of instrumental effects such as trigger efficiencies, detector acceptance, *etc.*. It is, within experimental errors, in agreement with the expected value of 0.307 (Equation 7.6).

7.7 Correcting for trigger inefficiencies

In CDF note 4191, the authors measured the trigger efficiency of the DIJET_12 trigger using single jet trigger efficiencies. Their results suggested that the trigger was not fully efficient below a dijet mass value of $\sim 130 \text{ GeV}/c^2$. We have used an alternative method to measure the trigger efficiency. The steps involved in extracting a trigger efficiency curve and a signal from the raw data are as follows:

- In the region of the dijet mass spectrum where only background events (dijets from QCD processes) are expected to be found, we fit the dijet mass spectrum with the functional form used by UA2, namely

$$m^\alpha e^{-\beta \cdot m} e^{-\gamma \cdot m^2}. \quad (7.11)$$

where $m(= m_{jj})$ is the dijet invariant mass and α , β , and γ are free parameters. This fit was performed in the region $m_{jj} = 125 - 300 \text{ GeV}/c^2$ and is shown in Figure 7.10 for the raw dijet mass spectrum (i.e., no jet corrections).

- The fit to the background region was extrapolated to dijet mass values below the starting point of the background fit, i.e., below $m_{jj} = 125 \text{ GeV}/c^2$. In the region above and below the expected signal region ($m_{jj} = 60 - 80 \text{ GeV}/c^2$ for the raw dijet mass spectrum) the original data was divided by the extrapolation of the background fit in order to find a trigger efficiency curve. Such a curve is shown in Figure 7.11.
- The trigger efficiency curve was fit on the left and right side of the expected signal region with two different functions.

$$\text{Eff}_{m_{jj}} = p_1 + (p_2 \tanh p_3(x - p_4)) \quad (7.12)$$

$$\text{Eff}_{m_{jj}} = (p_1 + \arctan p_2(x - p_3))p_4 \quad (7.13)$$

where p_1, p_2, p_3, p_4 are free parameters in the fit. These fits to the trigger efficiency above and below the expected signal region were used to find the trigger efficiency in the expected signal region.

- We divided the original data in the signal region by a fit to the trigger efficiency curve to find the dijet mass spectrum, corrected for trigger inefficiencies. This results in a “trigger corrected” dijet mass spectrum.
- Finally, we subtracted the original background fit (extrapolated to values of dijet mass in the expected signal region) from the trigger corrected dijet mass spectrum. Figure 7.12 shows a typical result of this procedure for the raw data (no jet energy corrections). We counted the number of events in the expected signal region.

Then we repeated this entire procedure for the dijet mass spectrum in which jet energies were obtained as described in Section 7.5 (“Method III spectrum”). A typical result of this procedure is shown in Figure 7.13.

7.8 Results

7.8.1 Signal Properties

Tables 7.2, 7.3, 7.4, 7.5, 7.6 list the results of many different fits. In these fits,

- different fit methods (χ^2 , Likelihood) were used to fit the background region
- different numbers of points on the left and right sides of the expected signal region were used to fit the trigger efficiency curves
- different functional forms (arctan and tanh) were used to fit the trigger efficiency curve

Results are shown for the raw dijet mass spectrum (Table 7.2) and the dijet mass spectrum in which jet energies were corrected with the procedure described in Section 7.5 (Tables 7.3, 7.4, 7.5, 7.6). Entries listed in the tables correspond to fits of the trigger efficiency curve in which the reduced χ^2 values were less than 1.1.

For the raw dijet mass spectrum, 43 fits had reduced χ^2 values less than 1.1. The mean value of the number of events in the signal region for these 43 fits is 3668 events and $\sigma_{rms} = 1297$ events. For the “Method III spectrum,” 112 fits resulted in reduced χ^2 values less than 1.1. The mean value of the number of signal events for these 112 fits is 9873 events. This corresponds to a signal to background ratio of $\sim 1/69$ when integrating the extrapolation of the background fit to the dijet mass spectrum from $m_{jj} = 72 - 98 \text{ GeV}/c^2$. For the 112 fits to the “Method III spectrum,” $\sigma_{rms} = 3950$ events. We interpret the σ_{rms} as the systematic error on the number of W and Z events observed due to the uncertainty of the trigger efficiency.

Table 7.2: Fits to the trigger efficiency curve derived from a χ^2 and likelihood fit to the background region ($m_{jj} = 125 - 300 \text{ GeV}/c^2$) of the raw dijet mass spectrum (no jet energy corrections). Functions involving arctan and tanh (see Equations 7.13, 7.12) are used to fit the trigger efficiency curve, and different numbers of points on the left and right sides of the signal region are included in the fit (to the trigger efficiency curve). All entries in the table correspond to fits (to the trigger efficiency curve) which had reduced χ^2 values less than 1.1.

| Background Fit | Trigger fit function | # pts left | # pts right | Signal | Error on signal |
|----------------|----------------------|------------|-------------|---------|-----------------|
| likelihood | atan | 9 | 9 | 5951.48 | 632.996 |
| likelihood | atan | 8 | 8 | 6521.34 | 633.951 |
| likelihood | atan | 10 | 9 | 4814.61 | 631.061 |
| likelihood | atan | 10 | 8 | 4891.98 | 631.179 |
| likelihood | atan | 10 | 7 | 4774.5 | 630.995 |
| likelihood | atan | 10 | 6 | 4931.24 | 631.246 |
| likelihood | tanh | 9 | 9 | 3578.43 | 629.017 |
| likelihood | tanh | 15 | 20 | 1741.98 | 625.889 |
| likelihood | tanh | 10 | 20 | 2417.89 | 627.024 |
| likelihood | tanh | 9 | 20 | 3305.22 | 628.515 |
| likelihood | tanh | 8 | 20 | 3194.77 | 628.331 |
| likelihood | tanh | 7 | 20 | 2265.5 | 626.799 |
| likelihood | tanh | 6 | 20 | 2473.55 | 627.135 |
| likelihood | tanh | 5 | 20 | 2298.02 | 626.914 |
| likelihood | tanh | 4 | 20 | 2441.02 | 627.179 |
| likelihood | tanh | 9 | 5 | 4077.62 | 629.829 |
| likelihood | tanh | 15 | 4 | 1622.04 | 625.698 |
| likelihood | tanh | 15 | 6 | 1400.65 | 625.949 |
| likelihood | tanh | 10 | 4 | 2925.45 | 627.909 |
| χ^2 | atan | 9 | 9 | 6508.63 | 748.411 |
| χ^2 | atan | 8 | 8 | 6691.03 | 748.691 |
| χ^2 | atan | 15 | 20 | 3931.99 | 743.965 |
| χ^2 | atan | 10 | 20 | 3036.27 | 742.439 |
| χ^2 | atan | 7 | 20 | 1790.59 | 740.435 |
| χ^2 | atan | 5 | 20 | 1894.73 | 740.757 |
| χ^2 | atan | 4 | 20 | 2213.02 | 741.347 |
| χ^2 | atan | 15 | 5 | 3879.78 | 743.922 |
| χ^2 | atan | 15 | 9 | 3302 | 743.003 |
| χ^2 | atan | 15 | 4 | 3520.16 | 743.346 |
| χ^2 | atan | 15 | 7 | 3337.56 | 743.057 |
| χ^2 | atan | 15 | 6 | 3632.41 | 743.526 |
| χ^2 | atan | 10 | 9 | 1413.96 | 744.886 |
| χ^2 | atan | 10 | 4 | 4243.61 | 744.57 |
| χ^2 | atan | 10 | 7 | 4332.04 | 744.745 |
| χ^2 | tanh | 9 | 9 | 4050.83 | 744.325 |
| χ^2 | tanh | 10 | 20 | 3033.17 | 742.618 |
| χ^2 | tanh | 9 | 20 | 3628.71 | 743.567 |
| χ^2 | tanh | 8 | 20 | 3642.4 | 743.594 |
| χ^2 | tanh | 7 | 20 | 3635.76 | 743.649 |
| χ^2 | tanh | 6 | 20 | 3441.73 | 743.241 |
| χ^2 | tanh | 5 | 20 | 4438.35 | 745.068 |
| χ^2 | tanh | 4 | 20 | 4675.45 | 745.145 |
| χ^2 | tanh | 9 | 5 | 4434.23 | 744.908 |

As a check of our method, we repeated the procedure described above with the raw dijet mass spectrum but used a different expected signal region. $m_{jj} = 90 - 110 \text{ GeV}/c^2$, when fitting the trigger efficiency curve, i.e., we looked for a signal in a dijet mass region where we would not expect to find one. The results are shown in Tables 7.7 and 7.8. Fifty-seven fits to the trigger efficiency curve resulted in reduced χ^2 values less than 1.1. The mean value of the number of signal events is 43 events and $\sigma_{rms} = 274$ events. Thus, in a region where no signal is expected, a result consistent with zero signal events is found.

Table 7.3: Fits to the trigger efficiency curve derived from a likelihood fit to the background region ($m_{jj} = 125 - 300 \text{ GeV}/c^2$) of the dijet mass spectrum in which jet energies were corrected using the method described in Section 7.5. A function involving arctan (see Equation 7.13) is used to fit the trigger efficiency curve, and different numbers of points on the left and right sides of the signal region are included in the fit (to the trigger efficiency curve). All entries in the table correspond to fits (to the trigger efficiency curve) which had reduced χ^2 values less than 1.1.

| Background Fit | Trigger fit function | # pts left | # pts right | Signal | Error on signal |
|----------------|----------------------|------------|-------------|---------|-----------------|
| likelihood | atan | 9 | 9 | 12219.7 | 1088.17 |
| likelihood | atan | 5 | 4 | 12588.4 | 1088.8 |
| likelihood | atan | 5 | 5 | 1859.04 | 1072.9 |
| likelihood | atan | 9 | 20 | 2509.41 | 1073.04 |
| likelihood | atan | 3 | 20 | 2010.08 | 1072.43 |
| likelihood | atan | 7 | 20 | 1989.86 | 1072.5 |
| likelihood | atan | 6 | 20 | 2471.41 | 1073.44 |
| likelihood | atan | 5 | 20 | 5881.56 | 1079.45 |
| likelihood | atan | 4 | 20 | 8638.04 | 1084.13 |
| likelihood | atan | 9 | 15 | 6857.28 | 1079.8 |
| likelihood | atan | 4 | 15 | 6207.08 | 1078.9 |
| likelihood | atan | 7 | 15 | 6127.22 | 1078.81 |
| likelihood | atan | 6 | 15 | 6250.52 | 1079.43 |
| likelihood | atan | 5 | 15 | 4815.63 | 1083.43 |
| likelihood | atan | 4 | 15 | 11087.1 | 1087.72 |
| likelihood | atan | 9 | 10 | 11963.6 | 1087.77 |
| likelihood | atan | 4 | 10 | 11577.4 | 1087.2 |
| likelihood | atan | 7 | 10 | 11917.4 | 1087.64 |
| likelihood | atan | 6 | 10 | 11741.8 | 1087.54 |
| likelihood | atan | 5 | 10 | 12562 | 1089.44 |
| likelihood | atan | 4 | 10 | 14150.7 | 1092.26 |
| likelihood | atan | 9 | 7 | 12466.9 | 1088.58 |
| likelihood | atan | 9 | 7 | 12344.1 | 1088.4 |
| likelihood | atan | 9 | 6 | 12399.5 | 1088.45 |
| likelihood | atan | 5 | 9 | 12159.2 | 1088.81 |
| likelihood | atan | 5 | 4 | 13900.3 | 1091.46 |
| likelihood | atan | 5 | 7 | 12084 | 1088.75 |
| likelihood | atan | 5 | 6 | 4076.67 | 1082.66 |

7.8.2 Cross section and comparison with Standard Model

The number of events found with the “Method III spectrum” has been converted to a cross section by correcting for event selection efficiencies (i.e., acceptances). In Section 7.4, the efficiencies of kinematic cuts are discussed in detail. The last column of Table 7.1 lists the combined efficiencies of all kinematic cuts, 14.4% and 13.4% for W and Z events respectively. Using the expected cross section ratio of W s and Z s, ($\sigma(W)/\sigma(W, Z)$ and $\sigma(Z)/\sigma(W, Z)$), a combined W, Z efficiency of $14.2 \pm 1.2\%$. The corrected cross section is $\sigma \cdot B(W, Z \rightarrow jets) = 36.6 \pm 14.6(\text{sys}) \pm 4.2(\text{stat}) \text{ nb}$, approximately 1.1 s.d. larger than the Standard Model prediction of $\sigma \cdot B(W, Z \rightarrow jets) = 20 \text{ nb}$ (Equation 7.6).

UA2 also quoted a cross section larger than the Standard Model prediction [29].

Table 7.4: Fits to the trigger efficiency curve derived from a likelihood fit to the background region ($m_{jj} = 125 - 300 \text{ GeV}/c^2$) of the dijet mass spectrum in which jet energies were corrected using the method described in Section 7.5. A function involving tanh (see Equation 7.12) is used to fit the trigger efficiency curve, and different numbers of points on the left and right sides of the signal region are included in the fit (to the trigger efficiency curve). All entries in the table correspond to fits (to the trigger efficiency curve) which had reduced χ^2 values less than 1.1.

| Background Fit | Trigger fit function | # pts left | # pts right | Signal | Error on signal |
|----------------|----------------------|------------|-------------|---------|-----------------|
| likelihood | tanh | 9 | 9 | 11749.5 | 1087.52 |
| likelihood | tanh | 8 | 8 | 12586 | 1088.83 |
| likelihood | tanh | 5 | 5 | 2040.98 | 1073.74 |
| likelihood | tanh | 9 | 20 | 4757.04 | 1076.79 |
| likelihood | tanh | 8 | 20 | 4898.24 | 1077.12 |
| likelihood | tanh | 7 | 20 | 4444.05 | 1076.56 |
| likelihood | tanh | 6 | 20 | 5695.28 | 1078.52 |
| likelihood | tanh | 5 | 20 | 9930.74 | 1085.69 |
| likelihood | tanh | 4 | 20 | 12709.5 | 1090.31 |
| likelihood | tanh | 9 | 15 | 7559.5 | 1081.07 |
| likelihood | tanh | 8 | 15 | 7454.05 | 1080.99 |
| likelihood | tanh | 7 | 15 | 7465.21 | 1081.01 |
| likelihood | tanh | 6 | 15 | 7863.64 | 1081.73 |
| likelihood | tanh | 5 | 15 | 11460.6 | 1087.92 |
| likelihood | tanh | 4 | 15 | 13864.3 | 1091.95 |
| likelihood | tanh | 9 | 10 | 11647.8 | 1087.36 |
| likelihood | tanh | 8 | 10 | 11391.7 | 1086.99 |
| likelihood | tanh | 7 | 10 | 11524.2 | 1087.14 |
| likelihood | tanh | 6 | 10 | 11633.4 | 1087.38 |
| likelihood | tanh | 5 | 10 | 13897.7 | 1091.53 |
| likelihood | tanh | 4 | 10 | 15790.3 | 1094.77 |
| likelihood | tanh | 9 | 4 | 12588 | 1084.83 |
| likelihood | tanh | 9 | 7 | 12127.9 | 1084.57 |
| likelihood | tanh | 9 | 6 | 11997.4 | 1087.48 |
| likelihood | tanh | 5 | 9 | 13454.1 | 1090.48 |
| likelihood | tanh | 5 | 4 | 14905 | 1092.88 |
| likelihood | tanh | 5 | 7 | 13837.2 | 1091.45 |
| likelihood | tanh | 5 | 6 | 9166.22 | 1084.45 |

The ratio

$$R = \frac{\sigma \cdot B(W, Z \rightarrow q\bar{q})}{\sigma \cdot B(W \rightarrow e\nu) \cdot \frac{\Gamma(W \rightarrow q\bar{q})}{\Gamma(W \rightarrow e\nu)} + \sigma \cdot B(Z \rightarrow ee) \cdot \frac{\Gamma(Z \rightarrow q\bar{q})}{\Gamma(Z \rightarrow ee)}} \quad (7.14)$$

is expected to be unity in the Standard Model. The values of the ratios of the partial decay widths into quarks and leptons are

$$\frac{\Gamma(W \rightarrow q\bar{q})}{\Gamma(W \rightarrow e\nu)} = 6.25 \quad (7.15)$$

$$\frac{\Gamma(Z \rightarrow q\bar{q})}{\Gamma(Z \rightarrow ee)} = 21.1.$$

UA2 quoted a value $R = 1.71 \pm 0.45$. We find $R = 1.74 \pm 0.72$.

Table 7.5: Fits to the trigger efficiency curve derived from a χ^2 fit to the background region ($m_{jj} = 125 - 300 \text{ GeV}/c^2$) of the dijet mass spectrum in which jet energies were corrected using the method described in Section 7.5. A function involving arctan (see Equation 7.13) is used to fit the trigger efficiency curve, and different numbers of points on the left and right sides of the signal region are included in the fit (to the trigger efficiency curve). All entries in the table correspond to fits (to the trigger efficiency curve) which had reduced χ^2 values less than 1.1.

| Background Fit | Trigger fit function | # pts left | # pts right | Signal | Error on signal |
|----------------|----------------------|------------|-------------|---------|-----------------|
| | atan | 9 | 9 | 12572.5 | 1123.19 |
| | atan | 8 | 8 | 13174.6 | 1124.17 |
| | atan | 5 | 5 | 1529.41 | 1107.32 |
| | atan | 9 | 20 | 2410.81 | 1107.39 |
| | atan | 8 | 20 | 2006.31 | 1106.95 |
| | atan | 7 | 20 | 2055.1 | 1107.13 |
| | atan | 6 | 20 | 2578.97 | 1108.15 |
| | atan | 5 | 20 | 6256.58 | 1114.62 |
| | atan | 4 | 20 | 9123.15 | 1119.49 |
| | atan | 9 | 15 | 6879.83 | 1114.32 |
| | atan | 4 | 15 | 6281.08 | 1113.52 |
| | atan | 7 | 15 | 6220.95 | 1113.46 |
| | atan | 6 | 15 | 6398.6 | 1113.9 |
| | atan | 5 | 15 | 9195.95 | 1118.98 |
| | atan | 4 | 15 | 11573.3 | 1123.66 |
| | atan | 9 | 10 | 12180.6 | 1122.58 |
| | atan | 4 | 10 | 11816.7 | 1122.05 |
| | atan | 7 | 10 | 12127.5 | 1122.48 |
| | atan | 6 | 10 | 11967.8 | 1122.31 |
| | atan | 5 | 10 | 12999.4 | 1124.66 |
| | atan | 4 | 10 | 14669.5 | 1127.63 |
| | atan | 9 | 8 | 13331.9 | 1124.39 |
| | atan | 9 | 7 | 13401.8 | 1124.52 |
| | atan | 9 | 6 | 12965.8 | 1123.8 |
| | atan | 5 | 9 | 12572 | 1124.02 |
| | atan | 5 | 8 | 14330.5 | 1126.66 |
| | atan | 5 | 7 | 12679.3 | 1124.2 |
| | atan | 5 | 6 | 8275.99 | 1117.54 |

7.9 Conclusions

A signal $\sigma \cdot B(W, Z \rightarrow jets)$ is observed in the dijet mass spectrum from a Run IC data sample taken with a low-threshold dijet trigger. The signal is observed at an invariant mass consistent with the W and Z masses. The measured cross section, $\sigma \cdot B(W, Z \rightarrow jets) = 35.6 \pm 14.2(\text{sys}) \pm 4.1(\text{stat}) \text{ nb}$ is consistent, within experimental errors with the Standard Model prediction. The systematic error is dominated by the uncertainty of the trigger efficiency. Hints of a double-peak structure are observed. The peaks are separated by $\sim 10 \text{ GeV}$, the mass difference between the W and Z , and the ratio of events in the peaks is consistent with the Standard Model prediction of $\sigma \cdot B(Z \rightarrow jets)/\sigma \cdot B(W \rightarrow jets)$. These results are obtained only after jet corrections

Table 7.6: Fits to the trigger efficiency curve derived from a χ^2 fit to the background region ($m_{jj} = 125 - 300 \text{ GeV}/c^2$) of the dijet mass spectrum in which jet energies were corrected using the method described in Section 7.5. A function involving tanh (see Equation 7.12) is used to fit the trigger efficiency curve, and different numbers of points on the left and right sides of the signal region are included in the fit (to the trigger efficiency curve). All entries in the table correspond to fits (to the trigger efficiency curve) which had reduced χ^2 values less than 1.1.

| Background Fit | Trigger fit function | # pts left | # pts right | Signal | Error on signal |
|----------------|----------------------|------------|-------------|---------|-----------------|
| χ^2 | tanh | 9 | 9 | 12153 | 1122.63 |
| | tanh | 9 | 9 | 13579.2 | 1124.83 |
| | tanh | 5 | 5 | 2147.15 | 1108.52 |
| | tanh | 9 | 20 | 4991.86 | 1111.66 |
| | tanh | 9 | 20 | 5162.21 | 1112.04 |
| | tanh | 7 | 20 | 5282.57 | 1112.26 |
| | tanh | 6 | 20 | 5973.18 | 1113.47 |
| | tanh | 5 | 20 | 10393.5 | 1120.97 |
| | tanh | 4 | 20 | 13246.8 | 1125.73 |
| | tanh | 9 | 15 | 7841.56 | 1116.01 |
| | tanh | 9 | 15 | 7747.47 | 1115.95 |
| | tanh | 7 | 15 | 7752.21 | 1115.96 |
| | tanh | 6 | 15 | 8174.9 | 1116.72 |
| | tanh | 5 | 15 | 12011.5 | 1123.17 |
| | tanh | 4 | 15 | 14416 | 1127.38 |
| | tanh | 9 | 10 | 11999.5 | 1122.39 |
| | tanh | 4 | 10 | 11853 | 1122.2 |
| | tanh | 7 | 10 | 11939.6 | 1122.28 |
| | tanh | 6 | 10 | 12000.5 | 1122.43 |
| | tanh | 5 | 10 | 14389.7 | 1126.82 |
| tanh | 4 | 10 | 16354.5 | 1130.2 | |
| tanh | 9 | 8 | 13758.7 | 1125.12 | |
| tanh | 9 | 7 | 13764.1 | 1125.11 | |
| tanh | 9 | 6 | 12474.8 | 1123.11 | |
| tanh | 5 | 9 | 13944.5 | 1126.17 | |
| tanh | 5 | 8 | 15303.2 | 1128.18 | |
| tanh | 5 | 7 | 14705.2 | 1127.3 | |
| tanh | 5 | 6 | 9540.26 | 1119.59 | |

based on a new calorimeter calibration procedure are applied to jet energies in the dijet sample.

This signal could be an important reference signal to calibrate the jet energy scale since the W and Z masses are known to great precision. Uncertainties on the jet energy scale currently limit the top mass measurement.

Table 7.7: Fits to the trigger efficiency curve derived from a likelihood fit to the background region ($m_{jj} = 125 - 300 \text{ GeV}/c^2$) of the raw dijet mass spectrum (no jet energy corrections). Functions involving arctan and tanh (see Equations 7.13, 7.12) are used to fit the trigger efficiency curve in a region **where no signal is expected**. $m_{jj} = 90 - 110 \text{ GeV}/c^2$. Different numbers of points on the left and right sides of the signal region are included in the fit (to the trigger efficiency curve). All entries in the table correspond to fits (to the trigger efficiency curve) which had reduced χ^2 values less than 1.1. The mean value of the number of events for all fits is consistent with zero.

| Fit # | Trigger fit function | # pts left | # pts right | Signal | Error on signal |
|------------|----------------------|------------|-------------|----------|-----------------|
| likelihood | atan | 3 | 3 | -91.2981 | 251.73 |
| likelihood | atan | 8 | 5 | -159.419 | 250.335 |
| likelihood | atan | 7 | 5 | -50.0344 | 251.886 |
| likelihood | atan | 6 | 5 | -88.0342 | 251.742 |
| likelihood | atan | 5 | 4 | -288.135 | 250.984 |
| likelihood | tanh | 7 | 7 | 304.182 | 253.23 |
| likelihood | tanh | 5 | 5 | -93.7266 | 251.721 |
| likelihood | tanh | 7 | 15 | 395.179 | 253.374 |
| likelihood | tanh | 6 | 15 | 343.41 | 253.378 |
| likelihood | tanh | 5 | 15 | 201.196 | 252.842 |
| likelihood | tanh | 4 | 15 | 179.62 | 252.759 |
| likelihood | tanh | 7 | 10 | 237.666 | 252.977 |
| likelihood | tanh | 6 | 10 | -37.1245 | 251.935 |
| likelihood | tanh | 5 | 10 | 88.3792 | 252.412 |
| likelihood | tanh | 10 | 5 | -215.518 | 251.259 |
| likelihood | tanh | 9 | 5 | -180.857 | 251.391 |
| likelihood | tanh | 6 | 5 | -5.7439 | 252.054 |
| likelihood | tanh | 10 | 4 | -290.173 | 250.977 |
| likelihood | tanh | 5 | 9 | 333.727 | 253.341 |
| likelihood | tanh | 5 | 9 | 139.605 | 252.606 |
| likelihood | tanh | 5 | 7 | 155.789 | 252.668 |
| likelihood | tanh | 5 | 4 | -58.3821 | 251.855 |

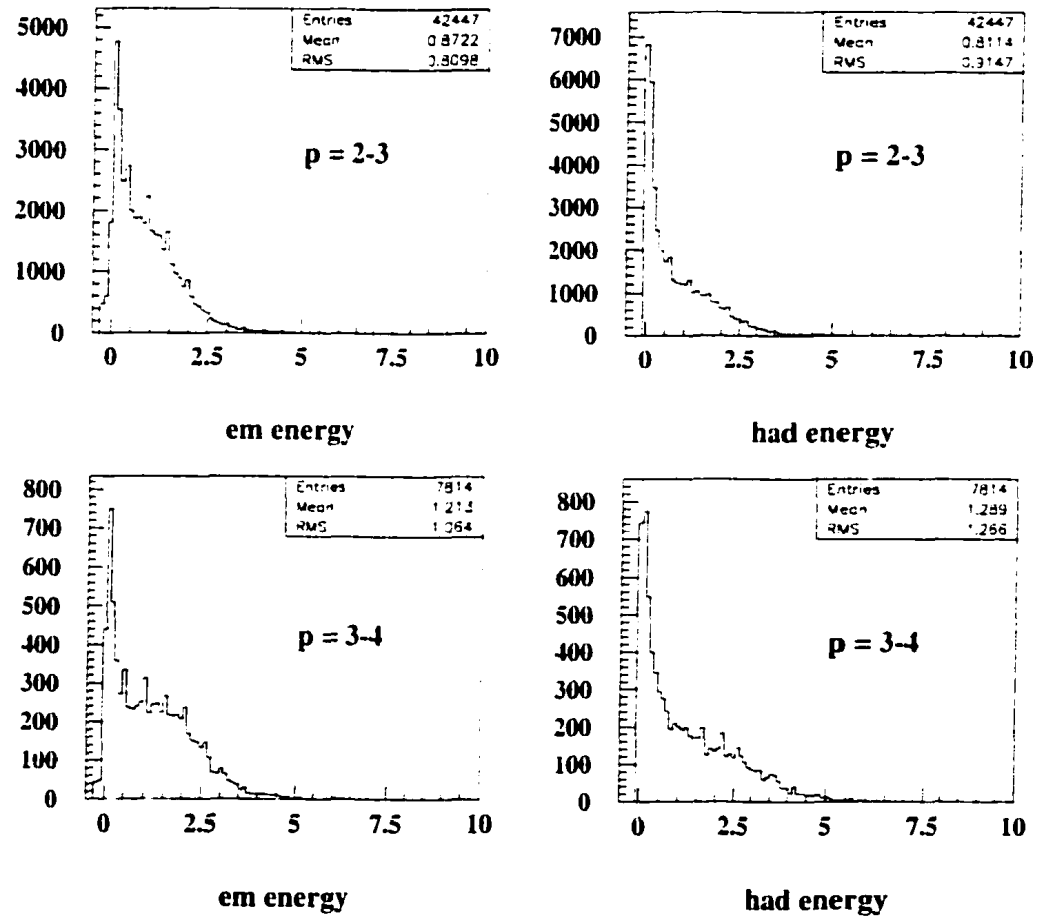


Figure 7.3: Signal distributions for the central electromagnetic calorimeter and the central hadronic calorimeter. Distributions were obtained from isolated tracks in Run IB minimum bias data and are shown for hadrons with $p = 2 - 3$ GeV/ c and $p = 3 - 4$ GeV/ c . See text for details.

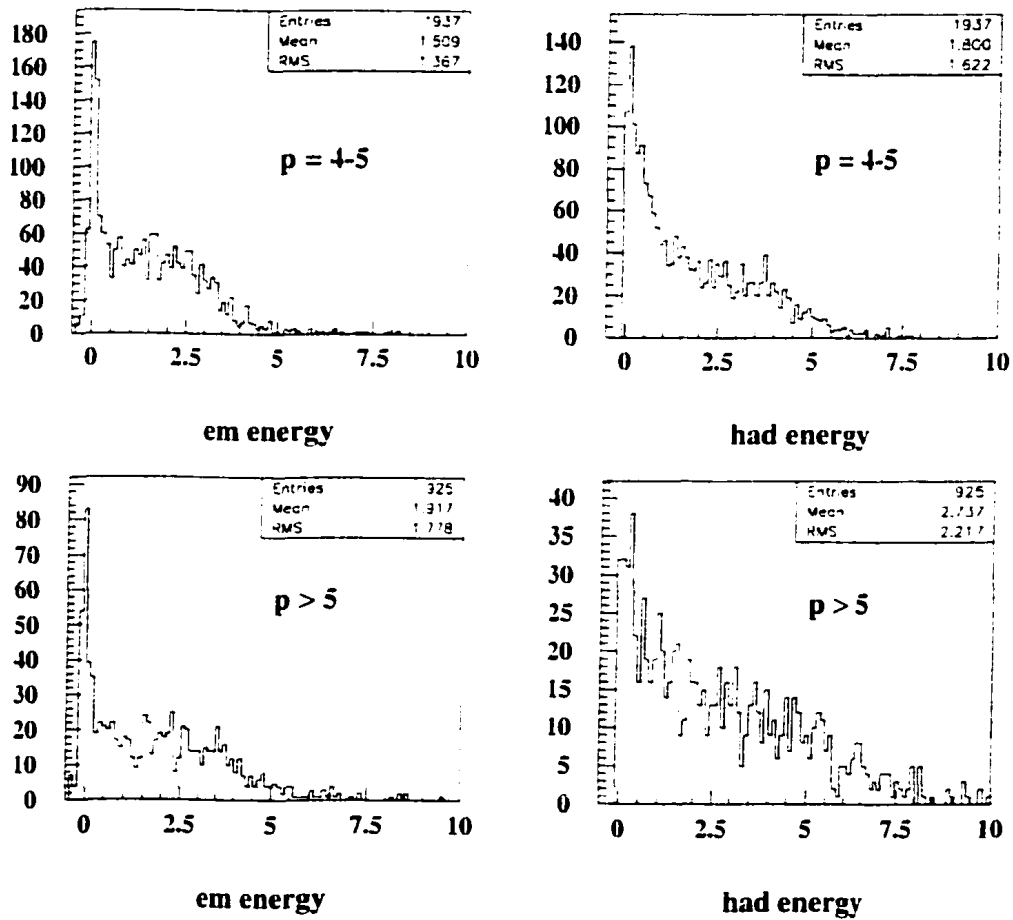


Figure 7.4: Central electromagnetic and hadronic calorimeter signal distributions obtained from isolated tracks in Run IB minimum bias data with $p = 4 - 5$ GeV and $p > 5$ GeV/c. See text for details.

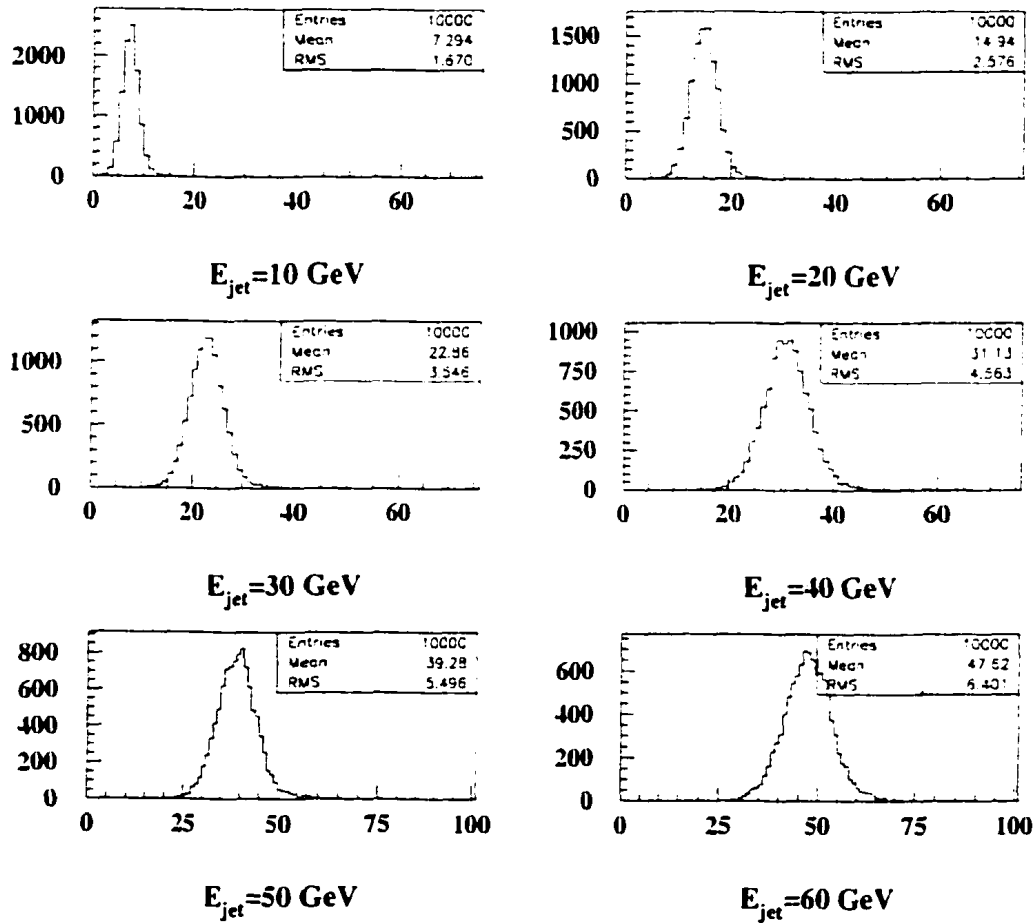


Figure 7.5: Jet signal distributions which result from simulations described in text. Here, Method III was used to set the energy scale of the central hadronic calorimeter. Distributions are shown for jet energies ranging from 10-60 GeV.

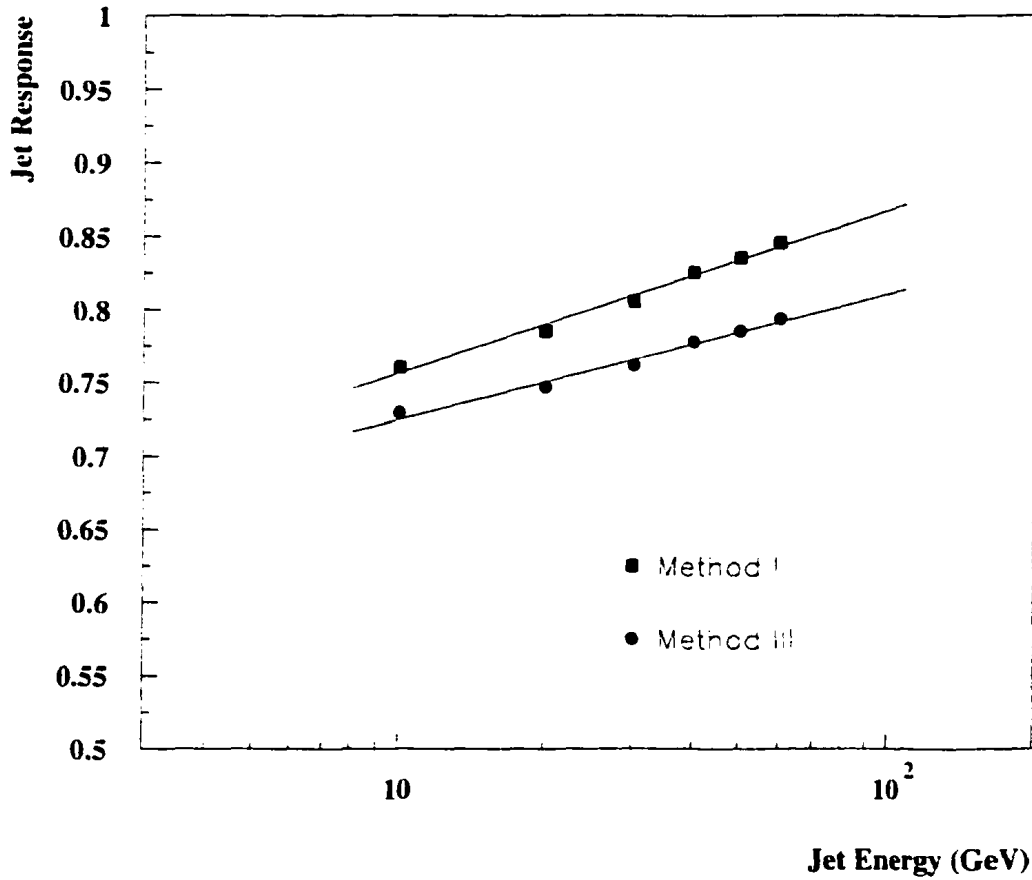


Figure 7.6: Jet response curves for CDF's traditional method of determining the energy scale of the hadronic calorimeter section (Method I) and a new method of setting the hadronic section energy scale (Method III). The response is normalized to that of electrons. The inverse of the response represents the correction factor for the absolute jet energy scale (see Equation 7.10).

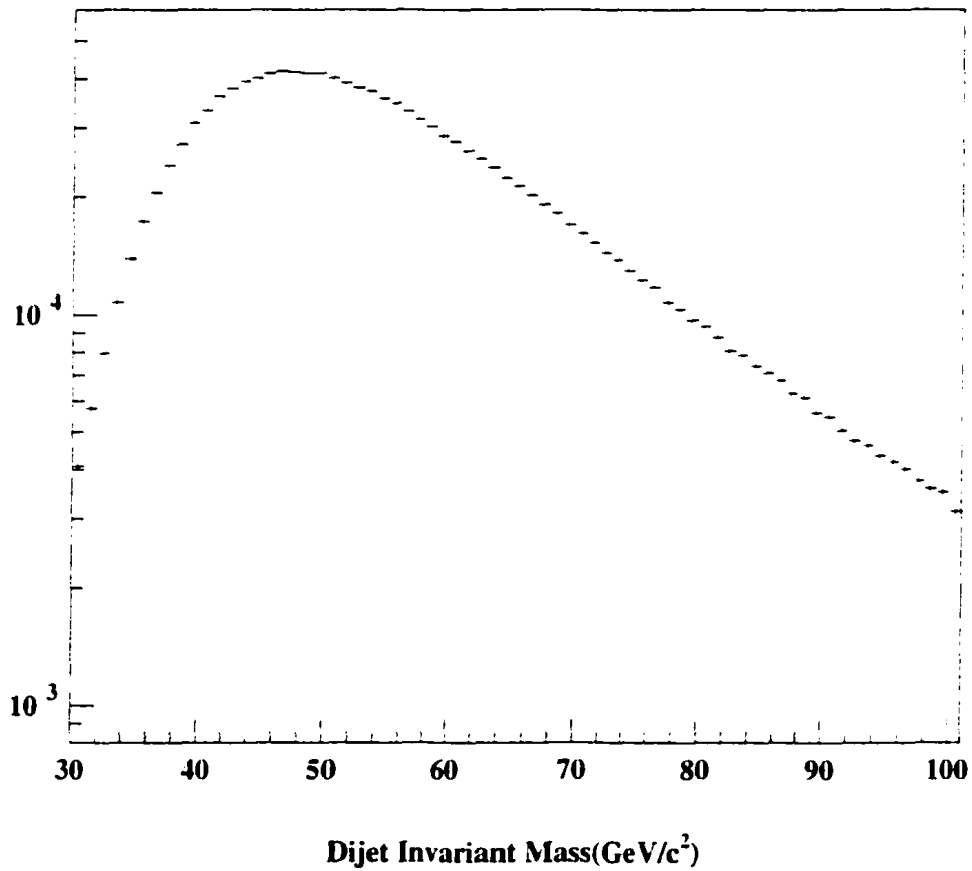


Figure 7.7: Raw dijet invariant mass spectrum. No energy corrections have been applied. The two jets were required to be back-to-back ($\cos \Phi < -0.4$) and events in which a third jet with $E_T > 15 \text{ GeV}$ was present were rejected. The steep falloff below $50 \text{ GeV}/c^2$ is a result of trigger inefficiencies.

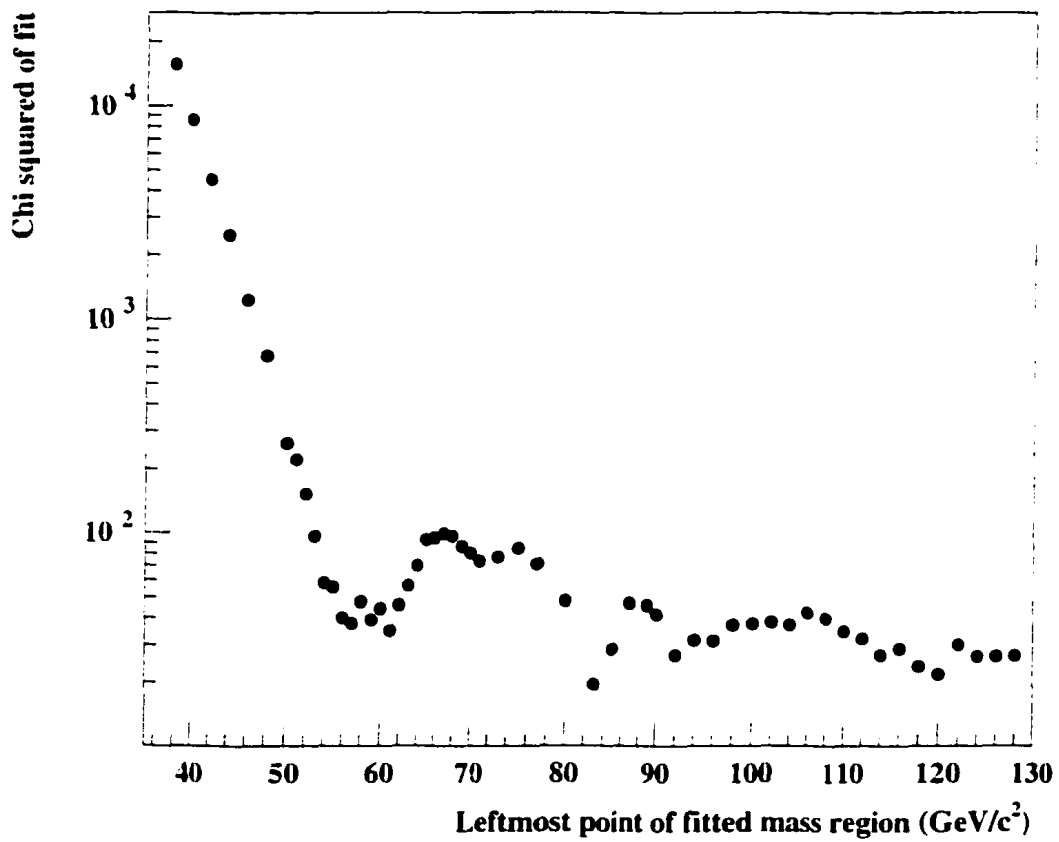
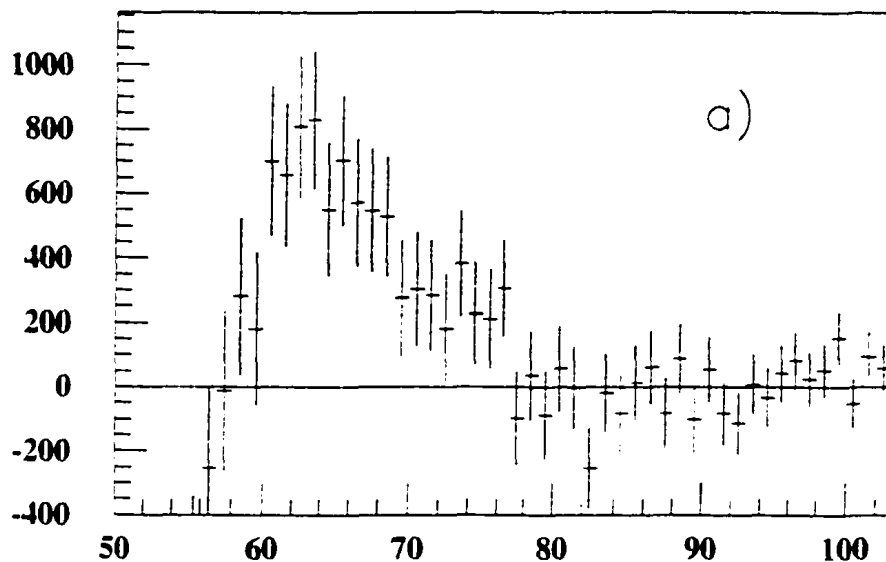
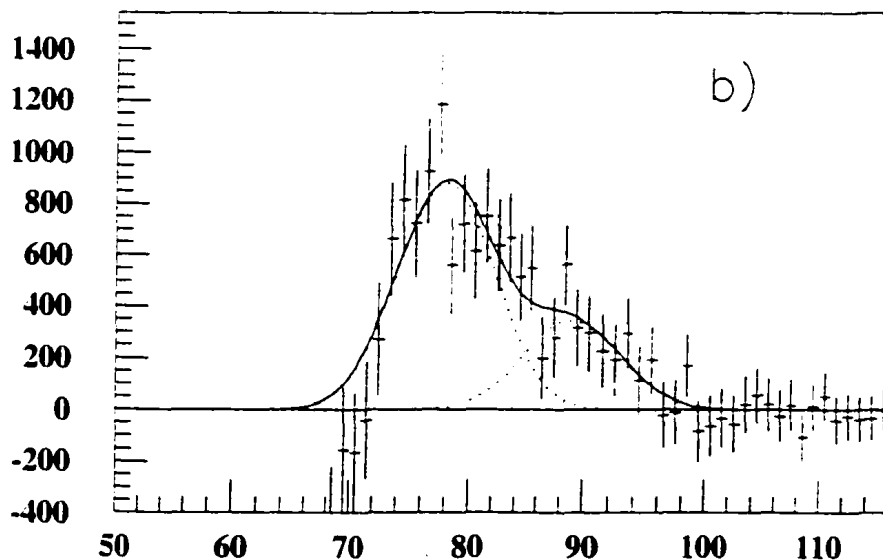


Figure 7.8: Quality of exponential fits to the dijet invariant mass spectrum over a limited mass range. Shown is the χ^2 (for 23 degrees of freedom) as a function of the lowest mass point of the 45 GeV/c^2 wide dijet mass region. See text for details.



Dijet Invariant Mass (GeV)



Dijet Invariant Mass (GeV)

Figure 7.9: Residuals when an exponential background is subtracted from the raw dijet mass spectrum (a) and from the dijet mass spectrum in which jets are corrected using Method III (b). The fit shown is the sum of two Gaussian distributions in which the difference between the two means and the ratio of the widths of the two gaussians were fixed, but all other parameters were left free. See text for details.

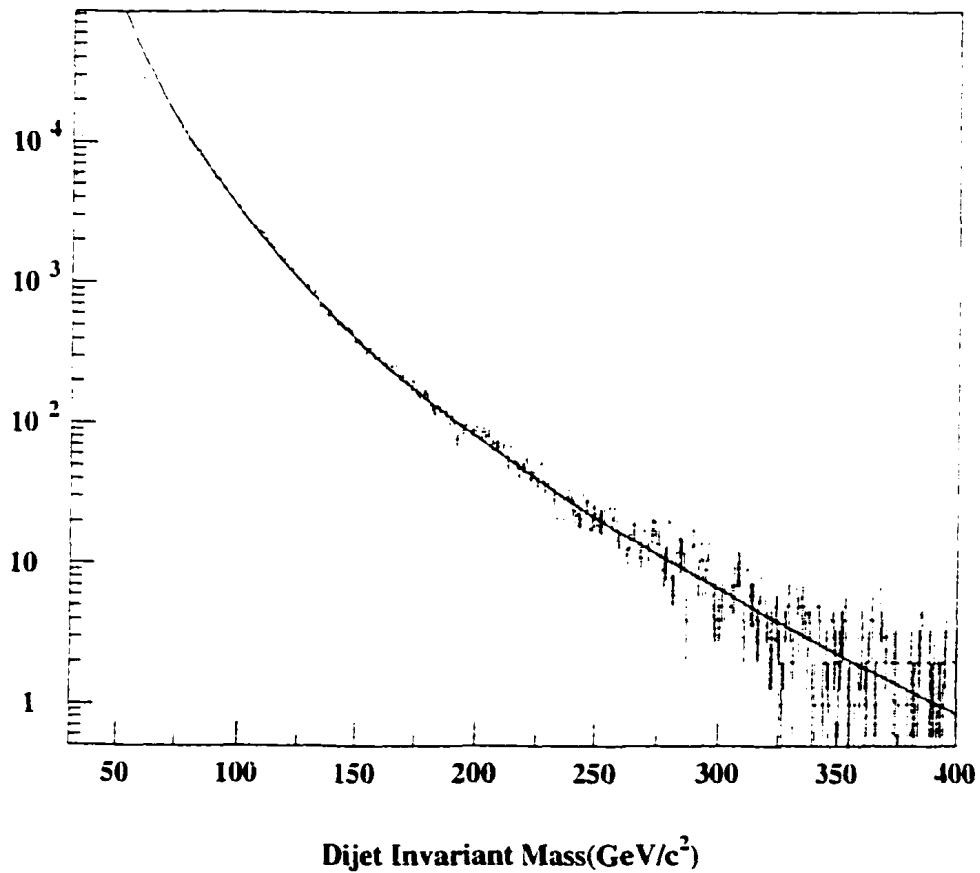


Figure 7.10: Raw dijet mass spectrum. Shown is a fit to the spectrum in the range 125-300 GeV/c^2 . The fit is extrapolated to lower values of dijet mass in order to extract a trigger efficiency vs dijet mass curve. See text for details.

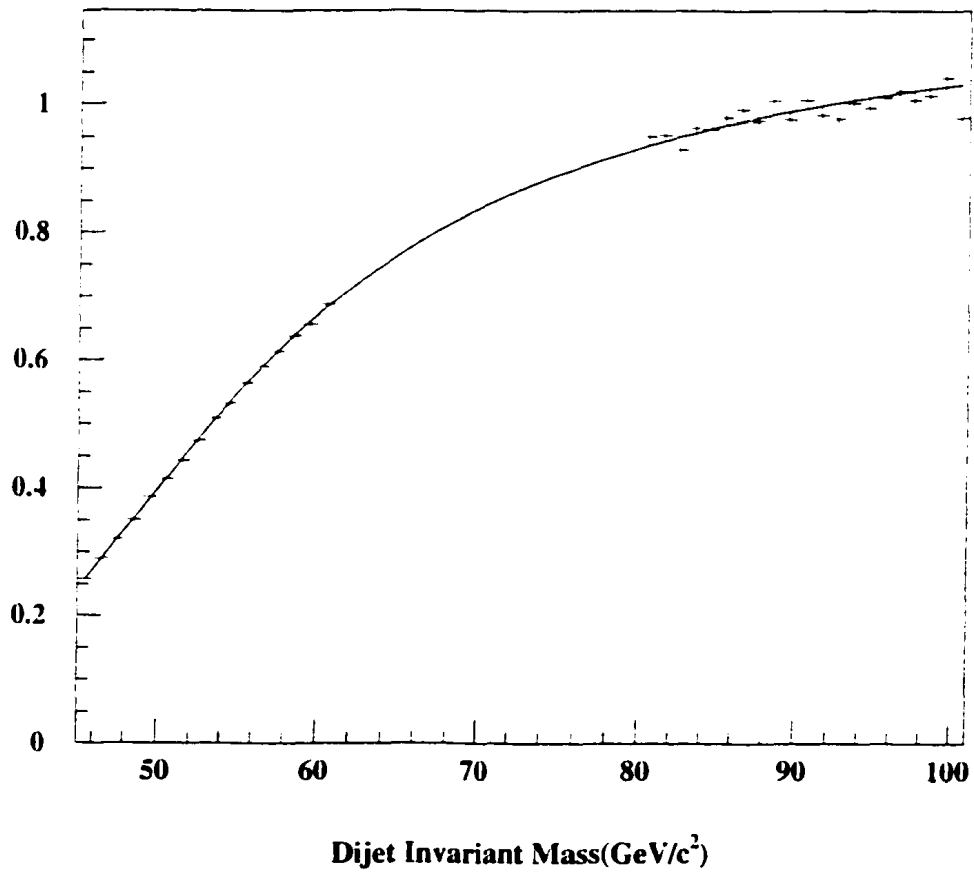


Figure 7.11: Trigger efficiency curve resulting from dividing the original dijet data (raw) by the extrapolated fit to the background region 125-300 GeV/c². Shown is a fit to the data with the function arctan. See text for details.

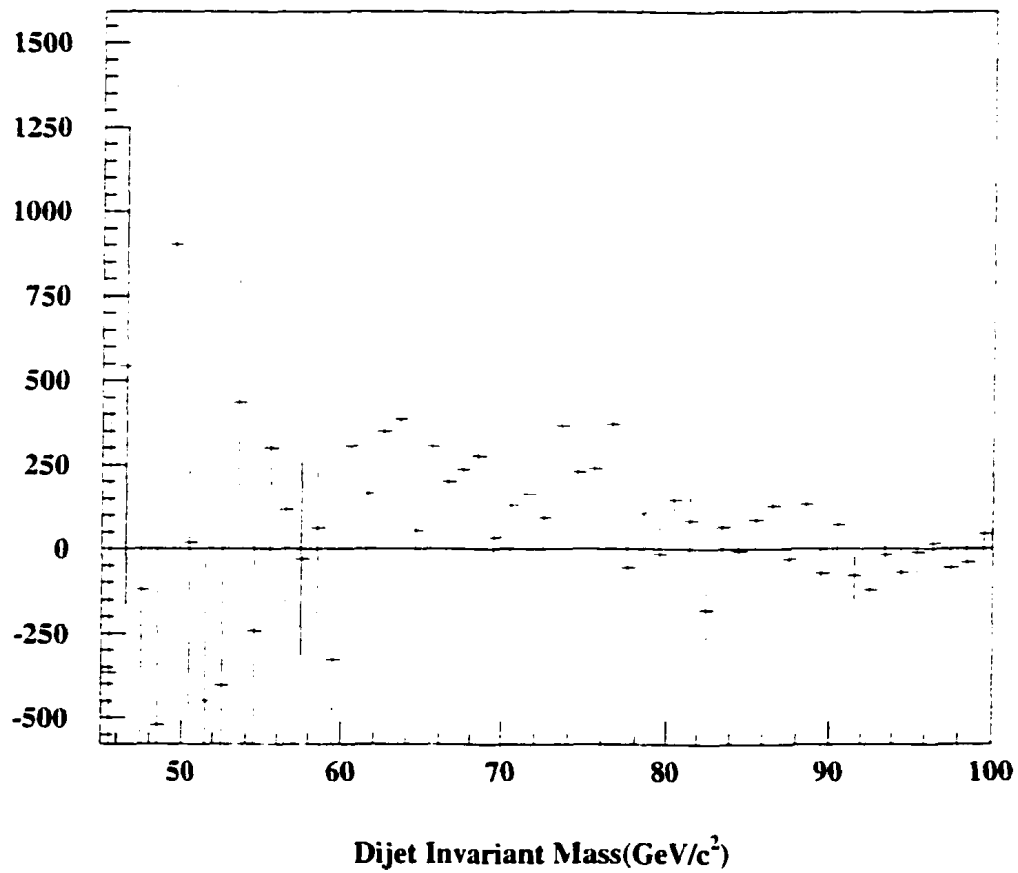


Figure 7.12: Resulting signal when the original data (raw) is divided by a fit to the trigger efficiency curve shown in Figure 7.11.

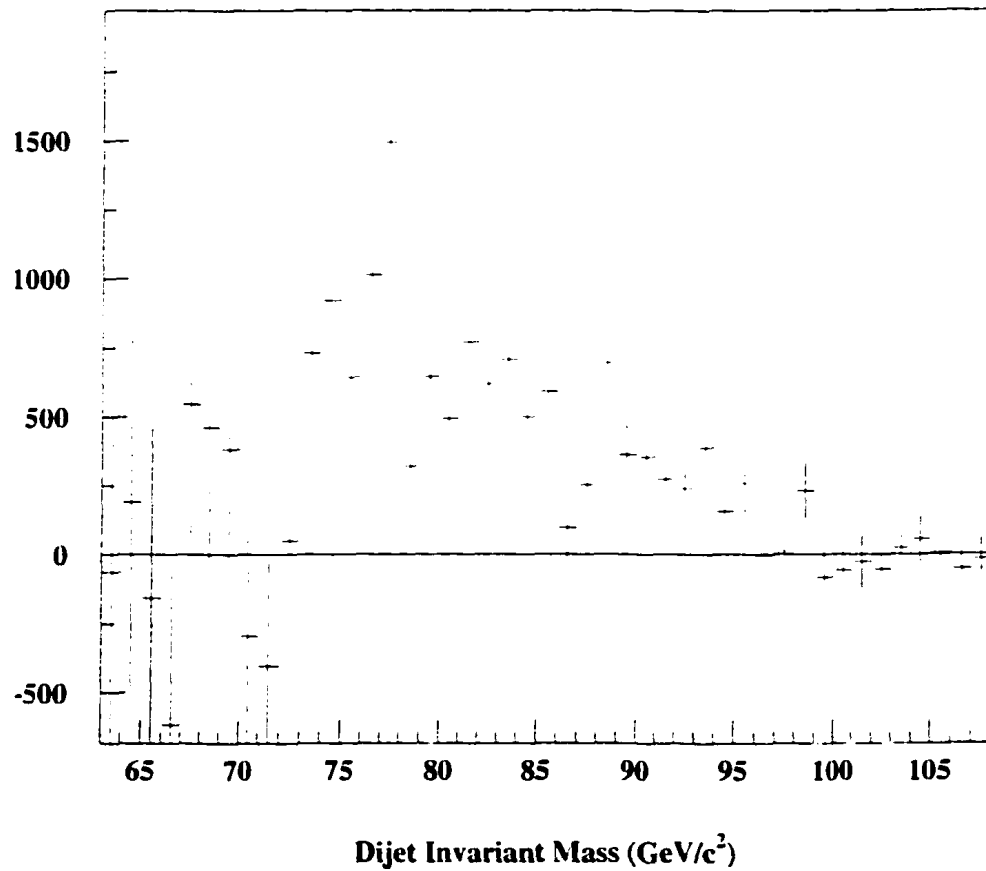


Figure 7.13: Resulting signal when the "Method III dijet mass spectrum" is divided by a fit to the trigger efficiency curve.

Table 7.8: Fits to the trigger efficiency curve derived from a χ^2 fit to the background region ($m_{jj} = 125 - 300 \text{ GeV}/c^2$) of the raw dijet mass spectrum (no jet energy corrections). Functions involving arctan and tanh (see Equations 7.13, 7.12) are used to fit the trigger efficiency curve in a region **where no signal is expected**, $m_{jj} = 90 - 110 \text{ GeV}/c^2$. Different numbers of points on the left and right sides of the signal region are included in the fit (to the trigger efficiency curve). All entries in the table correspond to fits (to the trigger efficiency curve) which had reduced χ^2 values less than 1.1. The mean value of the number of events for all fits is consistent with zero.

| Fit # | Trigger fit function | # pts left | # pts right | Signal | Error on signal |
|---------------|----------------------|------------|-------------|----------|-----------------|
| χ^2_{12} | atan | 4 | 5 | -166.302 | 260.8492 |
| χ^2_{12} | atan | 7 | 7 | 39.2971 | 261.6259 |
| χ^2_{12} | atan | 5 | 5 | 131.208 | 261.9403 |
| χ^2_{12} | atan | 9 | 15 | 190.911 | 262.2001 |
| χ^2_{12} | atan | 4 | 15 | 3.02246 | 261.4854 |
| χ^2_{12} | atan | 7 | 15 | 121.096 | 261.934 |
| χ^2_{12} | atan | 6 | 15 | 26.3574 | 261.575 |
| χ^2_{12} | atan | 5 | 15 | 209.351 | 262.269 |
| χ^2_{12} | atan | 4 | 15 | 208.201 | 262.264 |
| χ^2_{12} | atan | 7 | 10 | -34.1208 | 261.349 |
| χ^2_{12} | atan | 6 | 10 | -110.908 | 261.057 |
| χ^2_{12} | atan | 5 | 10 | 203.483 | 262.25 |
| χ^2_{12} | atan | 4 | 5 | -386.487 | 260.013 |
| χ^2_{12} | atan | 7 | 5 | -234.126 | 260.595 |
| χ^2_{12} | atan | 6 | 5 | -287.256 | 260.393 |
| χ^2_{12} | atan | 4 | 5 | 151.565 | 262.057 |
| χ^2_{12} | atan | 5 | 9 | 250.695 | 262.43 |
| χ^2_{12} | atan | 5 | 8 | 219.406 | 262.309 |
| χ^2_{12} | atan | 5 | 4 | 20.9641 | 261.566 |
| χ^2_{12} | tanh | 5 | 5 | 261.733 | 262.475 |
| χ^2_{12} | tanh | 10 | 15 | -360.405 | 260.11 |
| χ^2_{12} | tanh | 4 | 15 | -279.148 | 260.42 |
| χ^2_{12} | tanh | 5 | 15 | 714.364 | 264.181 |
| χ^2_{12} | tanh | 4 | 15 | 652.139 | 263.945 |
| χ^2_{12} | tanh | 9 | 10 | -452.167 | 259.763 |
| χ^2_{12} | tanh | 7 | 10 | -167.378 | 260.845 |
| χ^2_{12} | tanh | 6 | 10 | -215.253 | 260.663 |
| χ^2_{12} | tanh | 5 | 10 | 140.462 | 262.011 |
| χ^2_{12} | tanh | 8 | 5 | -634.431 | 259.075 |
| χ^2_{12} | tanh | 7 | 5 | 408.654 | 263.036 |
| χ^2_{12} | tanh | 6 | 5 | 369.624 | 262.883 |
| χ^2_{12} | tanh | 4 | 5 | 237.83 | 262.384 |
| χ^2_{12} | tanh | 5 | 9 | 457.84 | 263.214 |
| χ^2_{12} | tanh | 5 | 8 | 144.266 | 262.025 |
| χ^2_{12} | tanh | 5 | 4 | 109.115 | 261.9 |

CHAPTER 8

SUMMARY AND CONCLUSIONS

In this thesis, several studies involving the energy measurement of particles using calorimeters are presented. In Section 4.7, a study of the effects of radiation damage on the response of a prototype for the Compact Muon Solenoid (CMS) very forward calorimeter is described. We found that the effects of radiation damage on the calorimeter's response are dose dependent and that most of the damage will occur in the first year of running at the Large Hadron Collider (LHC). Based on our simulations, after 10 years of running, the energy resolution for 50 GeV photons will be degraded by 10% in the region of the detector that receives the most radiation.

In Section 6.4, an evaluation of the performance of an algorithm called the Energy Flow Method (EFM) is described. In this method, the information from the calorimeter system is combined with that from a high-resolution charged-particle tracker in an attempt to improve the energy resolution for jet measurements. We found that the Energy Flow Method provides at best a 30% improvement in energy resolution for the energy measurement of jets. The improvement decreases at high energies where the hadronic calorimeter resolution dominates the quality of the jet energy measurements.

Both studies described above have been published (or accepted for publication) in the scientific literature. Reprints of these papers can be found in Appendices A and C. I played a crucial role in both studies.

The main emphasis of this thesis is on a study described in Chapters 5 and 7. In Chapter 5, a study of three calibration methods for a longitudinally segmented calorimeter was presented. Testbeam data from the Collider Detector at Fermilab (CDF) Plug Upgrade calorimeter were used to study and evaluate the three methods. One method turned out to be particularly advantageous. This method has not traditionally been used for the CDF calorimeters. This work is described in more detail

in Appendix B, which is a reprint of a journal publication I wrote on this topic. This new method was applied to the Central CDF calorimeter in a search for hadronic decays of the W and Z bosons in the dijet mass spectrum (Chapter 7). A signal of $9873 \pm 3950(\text{sys}) \pm 1130$ events was found when the new calibration method was used. This corresponds to a cross section $\sigma \cdot B(W, Z \rightarrow jets) = 35.6 \pm 14.2(\text{sys}) \pm 4.1(\text{stat})$ nb. This result is 1.1 standard deviations larger than the Standard Model prediction. The large systematic uncertainty comes from the lack of precision with which the trigger efficiency is known.

The signal $W, Z \rightarrow jets$ serves as a one-of-a-kind check on the jet energy scale. Since the W and Z bosons have precisely known masses, the signal serves as a reference calibration signal for the energy measurement of jets in the same way that the signal $Z \rightarrow e^+e^-$ serves as a reference calibration signal for the energy measurement of electrons. The uncertainty of the jet energy scale is one of the most important sources of systematic uncertainty in determining the mass of the top quark or of any other new particle (e.g., the Higgs boson) in the 10^{11-12} eV range.

The Fermilab Tevatron is currently running with proton-antiproton collisions at $\sqrt{s} = 1.96$ GeV. With a well-designed trigger, a search for the hadronic decay of the W and Z bosons in the dijet mass spectrum could be performed in which the trigger is fully efficient at low dijet mass values. This would reduce the large systematic error present in this study. Such a signal could, as mentioned above, serve as a unique check of the jet energy scale. If the quantity $\sigma(p\bar{p} \rightarrow W, Z) \cdot B(W, Z \rightarrow jets)$ was measured with greater precision, it could also provide a check of the Standard Model.

BIBLIOGRAPHY

- [1] http://www-cdf.fnal.gov/grads/tips/thesis_tips.html#cdfpics.
- [2] S.D. Holmes FERMILAB-Conf-87/160 (unpublished).
- [3] F. Abe *et al.*, Nucl. Inst. Meth. A 271 (1988) 387.
- [4] D. Amidei *et al.*, Nucl. Inst. Meth. A 350. 73 (1994); D. Amidei *et al.*, Nucl. Inst. Meth. A 360. 137 (1995).
- [5] R. Wigmans, Rev. Sci. Instr. 69 (1998) 3723.
- [6] R. Wigmans. *Calorimetry - Energy Measurement in Particle Physics*. International Series of Monographs on Physics. vol. 107. Oxford University Press. Oxford (2000).
- [7] R. Wigmans. *Sampling calorimetry*. Nucl. Instr. and Meth. A. article in press.
- [8] N. Ackchurin *et al.*, Nucl. Inst. Meth. B 187 (2002) 66.
- [9] N. Akchurin *et al.*, Nucl. Inst. Meth. A 399 (1997) 202.
- [10] D. Acosta *et al.*, Nucl. Inst. Meth. B 62 (1991) 116.
- [11] CDF Collaboration, *The CDF II Technical Design Report*, Fermilab Internal Report 96/390-E (unpublished).
- [12] O. Ganel and R. Wigmans, Nucl. Instr. and Meth. A 409 (1998) 621.
- [13] R. Wigmans, Nucl. Instr. and Meth. A 259 (1987) 389.
- [14] T.A. Gabriel, *et al.*, Nucl. Instr. and Meth. A 338 (1994) 336.
- [15] O. Ganel and R. Wigmans, Nucl. Instr. and Meth. A 365 (1995) 104.

- [16] S. Behrends, M.D. Shapiro. E. Pare, *Single Pion Response in the Central Calorimeter*. CDF Note 1066 (1989).
- [17] M. Albrow, *et al.*, Nucl. Instr. and Meth. A 487 (2002) 381.
- [18] G. Hanson, *et al.*, Phys. Rev. Lett. 35. 1609 (1975).
- [19] D.P. Barber *et al.*, Phys. Rev. Lett. 43. 830 (1979).
- [20] UA2 Collab., M. Banner *et al.*, Phys. Lett. 118B. 203 (1982).
- [21] G. Drews *et al.*, Nucl. Instr. and Meth. A 290 (1990) 335.
- [22] O. Lobban, A. Sriharan, R. Wigmans, Nucl. Instr. and Meth. A 495 (2002) 107.
- [23] N. Eddy, *et al.*, "Observation of Hadronic W Decays in $t\bar{t}$ Events." CDF/ANAL/TOP/CDFR/3086 (1995).
 R. Wilkinson and R. Hollebeek, "Hadronic W Decays in b Tagged Top Candidates." CDF/ANAL/TOP/CDFR/3136 (1995); "Update to Hadronic W Decays in b Tagged Top Candidates," CDF/ANL/TOP/CDFR/3543 (1996).
 S. Aota, S. Kim, and K. Kondo, "A W mass peak in dijet invariant mass distribution for $W + 4$ -jet events," CDF/ANAL/TOP/CDFR/3034 (1995); "Update on a W mass peak in dijet invariant mass distribution for $W + \geq 4$ -jet events," CDF/ANAL/TOP/CDFR/3235 (1996).
- [24] T. Dorigo *et al.*, "Observation of Z Decays to b Quark Pairs in the Inclusive Muon Dataset," CDF/ANAL/EWK/CDFR/4320 (1997).
- [25] L. Galtieri *et al.*, "Jet P_T systematics studies using the $Z + \geq 1$ jet sample," CDF/PHYS/TOP/CDFR/3499 (1997).

- [26] S. Kim and S. Vejcik, "Jet E_T Scale from Momentum Balancing in $Z + 1$ Jet and Photon+1 Jet." CDF/ANAL/TOP/CDFR/3504 (1996).
- [27] L. Galtieri and J. Lys, "How well do we understand jets in Run I? Study of the Jet Energy Scale for Raw Jet $E_T \geq 8$ GeV." CDF/ANAL/TOP/CDFR/3983 (1997).
- [28] R. Wilkinson, R. Hollebeek, W. Wester, "Search for the Hadronic Decays $W/Z^0 \rightarrow jetjet$ Using Inclusive Dijets in Run IC." CDF/ANAL/JET/CDFR/4191 (1997).
- [29] J. Alitti *et al.*, Z. Phys. C-Particles and Fields 49. 17 (1991).
- [30] F. Abe, *et al.*, Phys. Rev. Lett. 76. 3070 (1996).
- [31] J. Dittmann, "Measurement of the $W + \geq 1$ Jet Cross Section in Proton-Antiproton Collisions at $\sqrt{s} = 1.8$ TeV." PhD Dissertation, Duke University, 1998.
- [32] S. Hauger, "Measurement of the $Z^0 \rightarrow e^+e^- + N$ Jet Cross Sections in $p\bar{p}$ Collisions at $\sqrt{s} = 1.8$ TeV." PhD Dissertation, Duke University, 1995.
- [33] L. Keeble and B. Flaugh, "New Jet Correction Function QDJSCO 2.0," /CDF/ANAL/JET/CDFR/1513 (1991).
- [34] CDF notes 583, 1066, 1286, 1344, 2838, 5600.
- [35] O. Lobban, R. Wigmans, "Calibration of the Central calorimeter using Run I minimum bias data," CDF/DOC/CALORIMETRY/PUBLIC/5848 (2002).
- [36] O. Lobban, R. Wigmans, "Intercalibration of the em and had sections of the Plug Upgrade Calorimeter: Part II," CDF/DOC/CALORIMETRY/PUBLIC/5586 (2001).

APPENDIX A
INTERCALIBRATION OF THE LONGITUDINAL SEGMENTS OF A
CALORIMETER SYSTEM (REPRINTED WITH PERMISSION FROM
NUCLEAR INSTRUMENTS AND METHODS, A487 (2002) 381)

Effects of radiation and their consequences for the performance of the forward calorimeters in the CMS experiment

N. Akchurin ^a, A.S. Ayan ^b, Gy.L. Bencze ^c, I. Dumanoglu ^d, E. Eskut ^d,
A. Fenyvesi ^e, A. Ferrando ^f, V. Gavrilov ^g, C. Hajdu ^c, M.I. Josa ^f, A. Kayis ^d,
V. Kolosov ^g, S. Kuleshov ^g, A. Kuzucu-Polatoz ^d, D. Litvintsev ^g, O. Lobban ^d,
J.-P. Merlo ^b, J. Molnár ^c, Y. Onel ^b, G. Önengüt ^d, D. Osborne ^h, N. Özdeş-Koca ^d,
V. Stolin ^g, L. Sulak ^b, A. Ulyanov ^g, S. Uzunian ^g, G. Vesztergombi ^c,
R. Wigmans ^{a,*}, D. Winn ⁱ, A. Yumashev ^g, P. Zalan ^c, M. Zeyrek ^{a,1}

^a Texas Tech University, Lubbock, U.S.A

^b University of Iowa, Iowa City, U.S.A

^c KFKI RMKI, Budapest, Hungary

^d Çukurova University, Adana, Turkey

^e ATOMKI, Debrecen, Hungary

^f CIEMAT, Madrid, Spain

^g ITEP, Moscow, Russia

^h Boston University, Boston, U.S.A

ⁱ Fairfield University, Fairfield, U.S.A

Received 28 June 2001

Abstract

The experiments at the Large Hadron Collider (LHC) will have to deal with unprecedented radiation levels. In the large-rapidity regions, close to the beam pipe, these levels reach megagrays per year. The detectors to be installed in these regions, the HF Calorimeters, are designed to operate under these conditions. In this paper, we describe the results of studies in which a prototype calorimeter was exposed to radiation of the type and intensity expected at the LHC. These studies made it possible to estimate the effects of this radiation on the response and the resolution of the calorimeter as a function of time during LHC operation. © 2002 Elsevier Science B.V. All rights reserved.

1. Introduction

Detectors in experiments at the future Large Hadron Collider (LHC) will have to operate at radiation levels that are considerably higher than in colliding-beam experiments at lower center-of-mass energies. Especially in the forward region, at

* Corresponding author. Tel.: +1-806-742-3779; fax: +1-806-742-1182.

E-mail address: wigmans@ttu.edu (R. Wigmans).

¹ On leave of absence. Permanent address: Middle East Technical University, Ankara, Turkey.

pseudorapidities $|\eta| = 3\text{--}6$, these radiation levels reach a domain that has remained an uncharted territory in particle physics experiments up to now: 1–10 MGy is expected to be accumulated during 10 years of LHC operation at design luminosity in this region.

Obviously, the design of detectors to be installed in this region is first and foremost guided by the necessity to survive in these harsh conditions. The CMS experiment [1] has chosen a calorimeter based on quartz fibers as active material for the high- η regions. High-purity quartz is known to be radiation-hard [2].

In previous publications, we have shown that this type of calorimeter, although primarily chosen because of its expected capability to operate under these difficult circumstances, possesses some very specific properties that are extremely valuable for calorimetry at high- η , where the particle density is very high in pp experiments: ultrafast signals and very narrow lateral shower profiles. These properties are a direct consequence of the fact that the signals in this calorimeter consist of Čerenkov light, primarily produced by the electrons and positrons from π^0 -induced electromagnetic shower components [3,4].

In this paper, we report the results of a dedicated study of the radiation effects, in which we focused our attention primarily on the consequences of degraded optical quality for relevant calorimetric properties such as the calorimeter response to showering particles of a given energy and the energy resolution with which such particles can be detected by this calorimeter. For these reasons, we irradiated an entire calorimeter module with particles of the type responsible for most of the absorbed radiation doses at LHC.

The paper is organized as follows. In Section 2, the calorimeter used in this study, the irradiation to which it was subjected, and the measurements carried out to assess the effects of this radiation are described. In Section 3, we present the experimental calorimeter data and the radiation dose profiles. These data are interpreted in the context of a simple model that describes the effects of increased light attenuation in the quartz fibers in terms of a parameter (α) that was first introduced in radiation hardness studies of scintillator-based

particle detectors. In Section 4, a Monte Carlo study is described that simulates the experimentally observed effects and predicts their impact on the calorimeter performance during LHC operation. Conclusions are given in Section 5.

2. Experimental setup

2.1. The detector

The calorimeter used for the studies described in this paper consisted of thin quartz fibers embedded in a copper matrix. The fibers were oriented along the direction traveled by the incoming particles. The showering particles generated Čerenkov light in the fibers. Photons emitted within the numerical aperture of the fibers were captured and transported through internal reflection to the fiber ends, where they were converted into photoelectrons in the photocathode of a photomultiplier tube (PMT). The digitized output of these PMTs comprised the calorimeter signals.

The quartz fibers consisted of a 0.30 mm diameter core surrounded by 0.015 mm thick cladding. The fibers were arranged in a hexagonal structure, each fiber equidistant (2.3 mm) from its

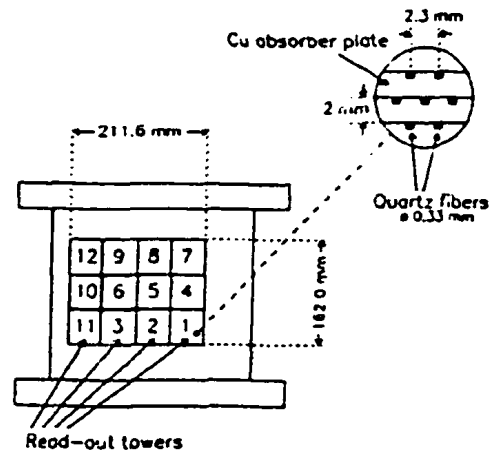


Fig. 1. The tower structure of the calorimeter. The inset shows the positioning of the quartz fibers.

six nearest neighbors. The fibers were embedded in 2.0 mm thick grooved copper plates. They occupied 1.8% of the detector volume (1.5% when excluding the cladding). The calorimeter contained in total ~ 6000 quartz fibers, which were grouped to form towers. Each tower measured 52.9×54 mm² and contained 598 fibers. The fibers extending out the back of each tower were bunched together, machined, polished and coupled through a hexagonal air light guide to a Philips XP2020 PMT.

The effective radiation length (X_0) of this detector was 1.49 cm, its nuclear interaction length (λ_{int}) 15.5 cm and its Molière radius (ρ_M) 1.55 cm. The calorimeter measured 33.75 cm in depth ($2.17 \lambda_{int}$, or $22.6X_0$) and was comprised of 12 towers (Fig. 1). The fibers were read out at one end, and were made reflective by aluminum deposition at the other end.

The calorimeter was equipped with two different types of fiber. The only difference between these fibers concerned the cladding. The central tower (#5) contained fibers of which the cladding consisted of fluorinated silica. The other towers contained fibers of which the quartz core was surrounded by hard-polymer cladding. In this paper, we limit ourselves to the study of radiation effects on the fibers with the fluorinated quartz cladding.

More details about this calorimeter, and the reasons for the design choices, are given in [3].

2.2. Test beam setup

The measurements were performed in the H4 beam line of the Super Proton Synchrotron at CERN. The detector was mounted on a platform that could be moved vertically and laterally with respect to the beam, so that the beam could be steered into any desired impact point on the calorimeter.

Upstream of the calorimeter, a trigger counter telescope was installed. It consisted of 5 scintillation counters of different sizes (from 2×2 mm² to 5×5 cm²), which allowed a choice of the beam spot size for the recorded events. Two drift chambers with x, y readout made it possible to determine the impact point of individual particles with a precision of ± 0.2 mm. Downstream of the calorimeter, two large scintillation counters were installed for muon identification.

The beam used for the tests described in this paper was a polarity and momentum selected secondary beam produced by 450 GeV protons incident on a target located about 550 m upstream of the calorimeter. For the tests described in this paper, we used these protons primarily to produce beams of electrons with energies of 80 or 150 GeV.

The crucial measurements for this particular study were performed with the detector rotated by 90° with respect to the normal operating position in CMS. In this setup, the detector signals could be measured as a function of the depth (z) at which

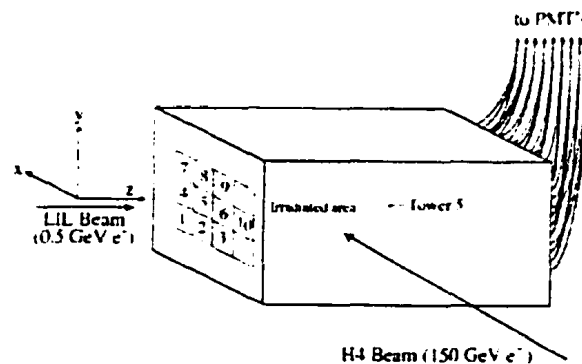


Fig. 2. Orientation of the quartz fiber calorimeter during the testbeam studies of the effects of radiation damage. The tower numbering is the same as in Fig. 1.

the Čerenkov light was generated. The beam particles traveled in the $-z$ direction (see Fig. 2).

During the measurements, the beam particle rates were such that typically a few thousand events per spill were recorded. The spills lasted 2.6 s and were repeated every 14 s. The widths of the collimators in the beam line were chosen such that the contribution of the momentum uncertainty of the beam particles was negligible, $\sim 0.5\%/\sqrt{E}$ (GeV).

2.3. Readout and calibration of the detector

The calorimeter signals were transported through 80 m long RG-58 cables to the counting room. The signals were fed into analog-to-digital converters (ADCs) with a dynamic range of 15 bits and a least count corresponding to 50 fC, which were operated at a gate width of 60 ns.

All individual cells of the calorimeter were calibrated with 80 GeV electrons incident on the cell center, i.e. traveling in the $-z$ direction (see Fig. 2). The PMT gains were chosen in such a way that the average signal for 80 GeV electrons entering the center of a calorimeter cell corresponded to about 500 ADC counts above the pedestal value in this cell. Since practically all the shower energy was deposited in one calorimeter cell, the PMT gain corresponded thus to ~ 0.3 pC/GeV (or 6 ADC counts per GeV).

The stability of the calibration was checked several times during the test periods (typically every 2 days) by sending an 80 GeV electron beam into the center of each and every calorimeter cell and measuring the signal distribution. The mean values of these distributions were reproduced to better than 2% in these measurements, for all channels.

2.4. The exposure to radiation at LIL

The radiation experienced by calorimeters operating at $3 < |\eta| < 5$ at the LHC originates primarily from the pp collisions themselves (as opposed to beam-gas interactions or losses that occur while filling the accelerator rings). The most abundant particles emerging from these interactions are soft (order 1 GeV) pions, both neutral

and charged ones, produced in the fragmentation of numerous quarks, diquarks and gluons that participate at the constituent level in the collision processes.

Since the entire energy of electromagnetic (em) showers is deposited in a region of limited depth, most of the effects of radiation damage on the calorimeter performance are the result of the production of em showers in the calorimeter itself, through the $\gamma\gamma$ decay of π^0 s. This process is responsible for the radiation doses received in the “hottest” regions of the experiment, located some $3-5$ radiation lengths inside the calorimeters that are installed near the beam pipe [1].

To mimic this situation in our radiation hardness studies, the calorimeter described above was exposed to an intense beam of 0.5 GeV electrons, produced by the linear injector for LEP (LIL). The beam intensity during this exposure was typically a few times 10^{11} electrons per second.

This beam was steered perpendicular to the mirrored fiber surface (i.e., in the $-z$ direction) into the central region of Tower 5 (see Fig. 2). In an exposure that lasted about 3 days, a total of 1.45×10^{16} electrons with an energy of 0.5 GeV each were sent into an area of a few cm^2 . The

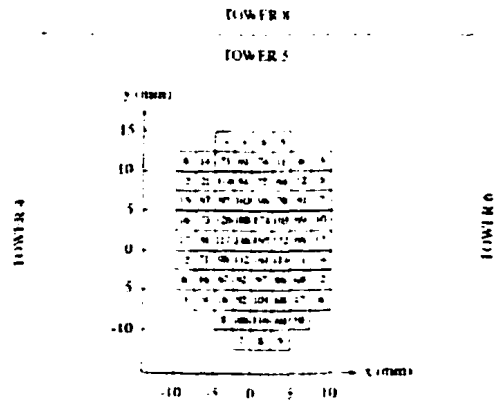


Fig. 3. Distribution of beam particles accumulated in Tower 5 during the exposure of the calorimeter at LIL. In total, 1.45×10^{16} electrons of 0.5 GeV were used for this purpose. The numbers are a measure for the particle fluxes in small ($2.5 \times 2.5 \text{ mm}^2$) dosimeters mounted on the calorimeter surface. They are expressed in units of megarads.

distribution of the impact points of the beam electrons in Tower 5 is indicated in Fig. 3, which shows the readings of an array of small ($2.5 \times 2.5 \text{ mm}^2$) dosimeters mounted on the calorimeter's front face.

The calorimeter became quite radioactive in this process. The dominant radioactive nuclide was ^{64}Cu , resulting from the reaction $^{63}\text{Cu}(\gamma, n)^{64}\text{Cu}$, initiated by γ s with energies of around 10 MeV (*giant-resonance production*), which are abundantly generated in em shower development. The half-life of this nuclide is 12.7 h and therefore the module had to cool down for about three days before it could be transported back to the H4 beam, where the tests to assess the effects of the radiation were performed.

3. Data analysis

3.1. Dose profiles

The three-dimensional dose profiles induced in the calorimeter module were determined with the help of EGS4 Monte Carlo simulations of the development of 0.5 GeV electron showers in copper [5]. It was recently shown that such simulations

give a good description of the relevant dose profiles [6]. The calorimeter module was described as a massive block of copper, subdivided into cells with dimensions of $5 \times 5 \times 5 \text{ mm}^3$. The EGS4 program simulated em shower development in this structure and yielded the energy deposited in each and every one of these cells. From this, the dose (in J/kg) could be determined in a straightforward way.

Some results of these simulations are shown in Figs. 4 and 5. These results concern longitudinal and lateral dose profiles induced by 1.45×10^{16} electrons of 0.5 GeV spread out over the front face of Tower 5 as indicated in Fig. 3.

In Fig. 4, the radiation dose induced by these particles is given as a function of the depth (z) inside the calorimeter, for the central axis ($x = y = 0$) and for a line located 2 cm above this axis ($x = 0, y = 2 \text{ cm}$, see Fig. 2). The maximum dose is reached at a depth of about 3 cm on the central axis and amounts to $\sim 6 \text{ MGy}$ (600 Mrad). The figure also shows that the calculated dose at the calorimeter's front face ($z = 0$) is in excellent agreement with the measured dosimeter value (195 Mrad).

The induced doses at $y = 2 \text{ cm}$ are smaller than those on the central detector axis. Also, the max-

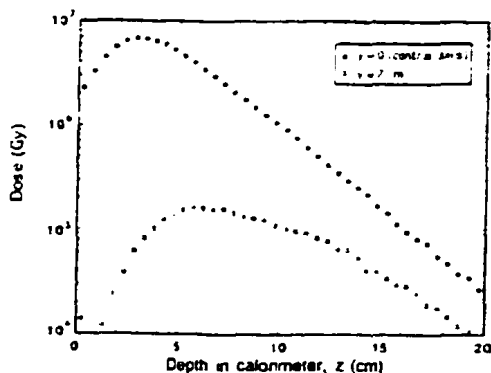


Fig. 4. The radiation dose induced in a block of copper by 1.45×10^{16} electrons of 0.5 GeV distributed as in the experimental exposure of the calorimeter module (see Fig. 3). Shown are the doses as a function of depth on the central axis of the exposed area and on a line 2 cm above this axis. Results of EGS4 simulations.

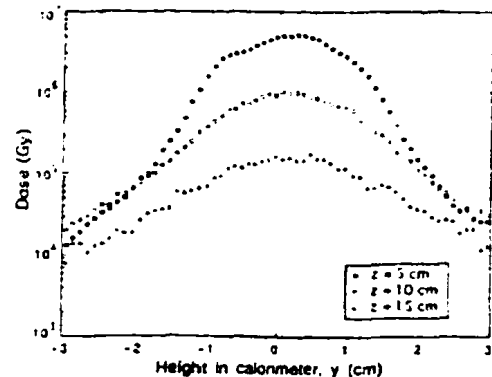


Fig. 5. The radiation dose induced in a block of copper by 1.45×10^{16} electrons of 0.5 GeV distributed as in the experimental exposure of the calorimeter module (see Fig. 3). Shown are the lateral distributions of the radiation dose, at three different depths inside the block: 5, 10 and 15 cm. Results of EGS4 simulations.

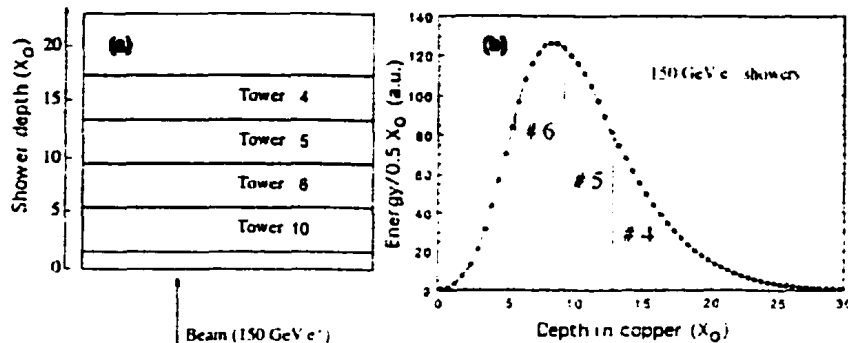


Fig. 6. Detector geometry in the z -scan with 150 GeV electrons (a) and the average (EGS4) profile of the energy deposited in the detector and in some of its towers by the showering electrons (b). See text for details.

imum occurs at a larger depth (6 cm versus 3 cm). This is a consequence of the lateral broadening of the profile as the showers develop in depth. The latter feature is illustrated in Fig. 5, which shows the lateral dose profiles at three different depths: 5, 10 and 15 cm.

The longitudinal dose profiles shown in Fig. 4 are a reasonable approximation of those that may be expected after 10 years of LHC operation at design luminosity for the $|\eta| = 4 - 5$ region of the CMS experiment (cf. Fig. 11).

3.2. Experimental detector data

After the calorimeter module was exposed to the 0.5 GeV LIL beam, it was moved to the H4 beam, where the effects on its performance were measured using a beam of 150 GeV electrons. This beam entered the detector sideways, i.e. perpendicular to the direction of the quartz fibers (Fig. 2). The calorimeter response was measured as a function of z , the distance between the impact point of the particles and the aluminized front face of the detector.

This z -scan was performed in steps of 1 cm, with the beam particles entering the detector at $y = 0$, probing the central region of the calorimeter, and at $y = 1.5$ cm, probing the boundary area between the central and top rows of towers. The beam spot was about 2×2 cm² in these measurements. Using

the information from the upstream beam chambers, the events could be subdivided into smaller (y, z) bins.

The 150 GeV electron showers deposited their energy primarily in Towers 6, 5 and 4 in these measurements. These towers probed the shower regions from 5.5–9.2 X_0 (Tower 6), 9.2–12.9 X_0 (Tower 5) and 12.9–16.6 X_0 (Tower 4), respectively, as shown in Fig. 6.

An example of the results of these measurements is shown in Fig. 7, where the average signal recorded in Tower 5 is plotted as a function of z , for events in which the electrons entered the detector at $y = 0 - 5$ mm (the open squares in Fig. 7(b)) and $y = 20 - 25$ mm (the full dots in Fig. 7(b)), respectively.

Before the irradiation, the signals recorded in scans of this type were practically independent of z . In a similar measurement made with a 1.5 m deep module, we observed that the signals varied by less than 5% over the entire depth. We concluded from this result that the attenuation length was larger than 20 m, at least for the Čerenkov light detected by a PMT with a glass window [3], as used in the present experiment.

However, in the measurements made *after* the described irradiation at LIL a clear reduction in the signals was observed. This reduction manifests itself in the *shape* of the z -distribution of the calorimeter response. This distribution exhibits a kink in the region $z = 15 - 20$ cm.

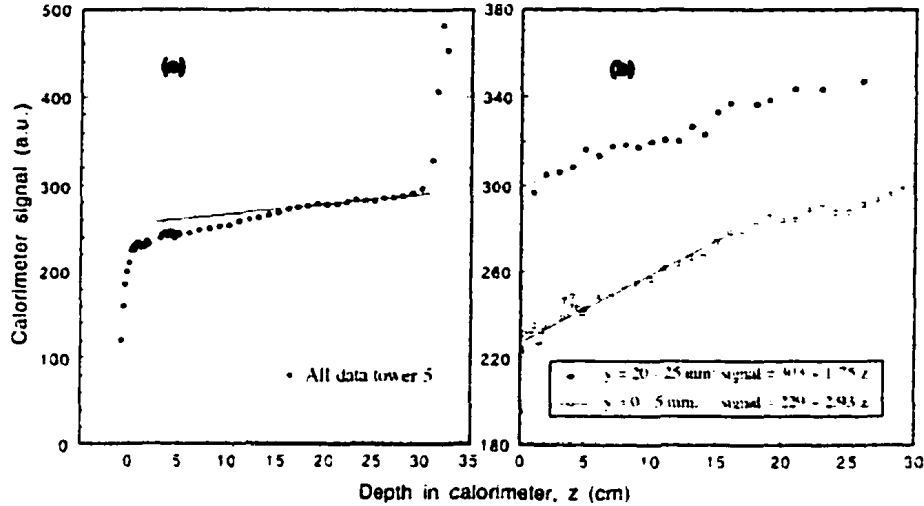


Fig. 7. The average signal in Tower 5 recorded in z -scans with electrons entering the detector in the regions $y = 0-5$ mm and $y = 20-25$ mm, respectively. The curves are drawn to guide the eye.

Fig. 4 shows that the radiation effects induced by the LIL beam were essentially limited to the area $z < 20$ cm. The z -scans with 150 GeV electrons revealed a clear z -dependence of the Tower-5 response for $z < 20$ cm. This dependence was stronger in the central region ($y = 0-5$ mm) than in the region located 20–25 mm above the center, which had received considerably less radiation.

In order to quantify this effect, we made a linear fit of the Tower-5 response, R_5 , in the region $z = 0-15$ cm, of the type

$$R_5(z) = p_1 + p_2 \cdot z. \quad (1)$$

The experimental data were subdivided into y -slices² of 5 mm, ranging from $y = -10$ mm to $y = 25$ mm. For each slice, the experimental z -distribution was fitted to Eq. (1). The value of p_2/p_1 , the normalized slope of the distribution in the region $z < 15$ cm, is shown as a function of y in Fig. 8(a).

² A y -slice is defined as a collection of events in which the H4 beam particles entered the calorimeter in the region $-10 \text{ mm} < y < -5 \text{ mm}$, $-5 \text{ mm} < y < 0 \text{ mm}$, etc., as determined by the upstream drift chambers.

The same figure also shows the integrated radiation dose in these y -slices, determined from the EGS4 simulations of the dose profiles. There is a clear correlation between the normalized slope of the response distribution and the radiation dose accumulated in the corresponding area. This clearly suggests that the observed change in the response distribution is a direct consequence of the induced radiation. However, it should also be pointed out that there is no one-to-one correspondence between the induced dose levels (Fig. 8(b)) and the value of p_2/p_1 (Fig. 8(a)). If induced radiation is indeed responsible for the change in the slope of the fiber's response curve, then relatively small doses (e.g., as induced in the region $y > 1.5$ cm) seem to have a disproportionately large effect. We will come back to this phenomenon in Section 3.3.

3.3. Simulations

3.3.1. A simple model

We have simulated the effects of the induced radiation on the measured experimental distribu-

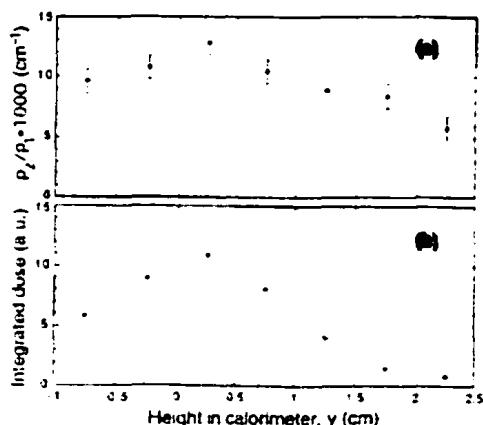


Fig. 8. The normalized slope of the z -distribution of the average calorimeter signals measured in Tower 5 (a) and the integrated radiation dose, determined from EGS simulations (b), as a function of the y value of the impact point of the electrons.

tions of the calorimeter response in the context of a simple model that was earlier developed to study radiation effects on the performance of scintillator-based fiber detectors [7,8]. In this model the local loss in light transmission is parameterized as

$$\frac{1}{l(z)} = \frac{1}{l_0} + \alpha D(z), \quad (2)$$

where $l(z)$ is the attenuation length at a depth z inside the calorimeter after the detector has received a radiation dose $D(z)$; l_0 represents the attenuation length in the absence of radiation. The radiation sensitivity of the detector is measured by the value of the parameter α . A small value of α corresponds to a small radiation sensitivity (i.e., a large radiation hardness). In radiation damage studies of plastic scintillators, α was typically found to be of the order of a few times 10^{-3} Mrad $^{-1}$ cm $^{-1}$ [8].

Eq. (2) neglects the wavelength dependence of radiation damage phenomena. It is well known that the attenuation length of quartz fibers depends on the wavelength of the light traveling through them and so does the deterioration of the transparency resulting from ionizing radiation. The shorter the wavelength, the more sensitive the fibers are.

However, in this study our primary interest is the extent to which the signals from this calorimeter are affected by the radiation. Therefore, our goal is to establish a value of α that applies to the Čerenkov light that is generated in our fibers and transformed in the PMTs into electric signals. A variety of factors such as the spectrum of the Čerenkov light, the wavelength dependent transmission through the glass window of the PMTs and the wavelength dependent quantum efficiency of these PMTs are thus implicitly folded into the value of α obtained in this study. Because of this, the sensitivity of our studies is limited to the wavelength interval from 400 to 600 nm.

Eq. (2) also assumes that the value of α is independent of the applied radiation dose. In the radiation hardness studies of plastic scintillators, for which this model was developed, this turned out to be a reasonable assumption. However, as will be shown in the following, it is an oversimplification which is not valid for the effects induced by ionizing radiation in the type of quartz fibers that are the subject of our study.

Using Eq. (2), the attenuation length of the quartz fibers can be calculated at any point inside the irradiated calorimeter once the value of α has been established. By choosing a value for α as a starting point, one may calculate the values of the attenuation length $l(z)$ and, from these, the z -distribution of the calorimeter response to electron showers. By comparing these response curves to the experimentally measured ones, the value of α may be determined empirically. This is the method we have used in practice.

The simulated response curves were obtained as follows. The Čerenkov light produced at a certain depth z and trapped inside the fibers was split into two components, with equal fractions going to the right ($+\hat{z}$, straight to the PMT) and to the left ($-\hat{z}$, to the aluminized front end of the fibers). The photons in both components were tracked in steps of 0.5 cm on their way through the fiber. In every step, the light intensity was diminished by a factor $\exp[-0.5/l(z)]$, with the local attenuation length $l(z)$ at depth z expressed in cm.

Light traveling to the left ($-\hat{z}$, see Fig. 2) was assumed to undergo an intensity loss of 20% upon reflection off the mirrored fiber end. The value of

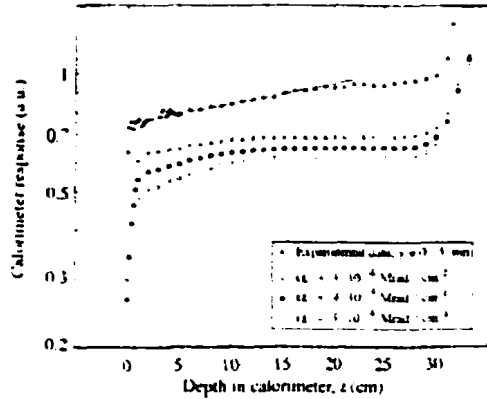


Fig. 9. Simulated response curves along the central axis of the irradiated calorimeter, for different values of the parameter α . For comparison, the experimentally measured curve, conveniently normalized, is shown as well. See text for details.

l_0 was taken as 20 m. Both assumptions were based on extensive z -scans with an unirradiated module of exactly the same composition [3].

In this way, the fraction of the Cerenkov light trapped in the fibers that reached the PMT was calculated. By repeating the described procedure for a large number of points at different depths (z), the simulated response curve was obtained.

Examples of simulated response curves obtained in this way are shown in Fig. 9. These curves were obtained on the basis of the dose profile $D(z)$ (and its consequences for the light attenuation characteristics of the fibers according to Eq. (2)) accumulated in the y interval 0–5 mm, averaged over the full x -width of Tower 5 (see Fig. 3). This was done to simulate the experimental conditions of the z -scan that was carried out along the central axis of the calorimeter. The simulated curves shown in Fig. 9 were obtained with α values ranging from 3×10^{-4} to 5×10^{-4} Mrad $^{-1}$ cm $^{-1}$. For comparison, the experimental z -response curve for $y = 0$ –5 mm, obtained from the Tower-5 calorimeter signals, is shown in the same figure.

The vertical scale of Fig. 9 has no absolute meaning. For the experimental data, the response was normalized to 1 for the region deep inside the calorimeter that was unaffected by radiation. For the simulated curves, the vertical scale denotes the

probability that light generated and trapped in the fibers at a certain depth z reaches the light detector.

The simulated curves exhibit the same characteristic features as the experimental data: a more or less flat response for z -values larger than 20 cm, where the radiation effects become negligibly small and a more or less logarithmic decline of the response for light produced in the affected region of the calorimeter ($z < 20$ cm). However, the kink separating these two sections of the response curve appears to be located deeper inside the detector than the simulations lead us to believe ($z \approx 20$ cm experimentally, versus $z \approx 10$ cm in the simulations).

In the context of this model, one would conclude from the observed z -dependence in the first 10 cm that α amounts to $(3$ – $4) \times 10^{-4}$ Mrad $^{-1}$ cm $^{-1}$. However, when we repeated this analysis for other regions in which z -scans had been performed (i.e., for different y -slices, where the induced doses were much smaller), we found that considerably larger α values were needed to describe the measured response curves. For example, in the y -slice around $y = 2$ cm, where the dose did not exceed 10 Mrad, α needed to be increased by an order of magnitude in order to get a reasonable description of the experimental response curve. And, as before, the simulations were only capable of reproducing the z -dependence in the first part of the detector, whereas the experimental effects of the induced radiation extended much deeper inside.

The parameter α is thus clearly dose dependent: relatively small doses of radiation cause relatively large effects of induced light attenuation. At doses of a few megarads, the radiation hardness is not much better than that of the best plastic scintillators [8], but at much higher doses the radiation hardness is considerably better. This dose dependence also explains some of the other experimental phenomena observed in this study, in particular:

- The absence of one-to-one correspondence between the measured slopes p_2/p_1 (Fig. 8(a)) and the calculated radiation doses in the various y -slices (Fig. 8(b)). Small doses produce a relatively large slope.

- The fact that the kink in the experimental z -scan is located deeper inside the calorimeter than in the simulated response functions (Fig. 9). The latter were calculated on the basis of a fixed value of α and thus tended to underestimate the relatively strong attenuation effects caused by the relatively small doses in the tails of the LIL-induced electron showers.

These effects suggest that a more detailed simulation of the experimental data, on the basis of a model in which the dose dependence of α is rigorously implemented, might improve the agreement with the experimental results.

3.3.2. Dose dependent modifications

Our experimental observations summarized at the end of the previous subsection qualitatively confirm the results of several other groups who have reported that the radiation-induced defects in glasses are well described by a power-law dependence on the dose levels [9]. In order to test the validity of such a dose dependence in more quantitative detail for our calorimeter, we repeated the

simulations of the fiber response curve described in the previous subsection with a dose dependent α value as follows:

$$\alpha(D) = \alpha_0 D^{-n} \tag{3}$$

This is equivalent to replacing the expression used to calculate the local light attenuation length $l(z)$ (Eq. (2)) by

$$\frac{1}{l(z)} = \frac{1}{l_0} + \alpha_0 D(z)^{-n} \tag{4}$$

We varied both the values of α_0 and n in order to obtain the best agreement with the experimental data. Some results of these simulations are shown in Fig. 10, together with the experimental response curve obtained from the Tower-5 signals in the z -scan along the central axis of the irradiated calorimeter (i.e., the 0–5 mm y -slice). Since we are only interested in the *shape* of the response curve, the data are plotted on a logarithmic vertical scale, the absolute value of which has been chosen arbitrarily, as in Fig. 9.

If we compare these results with those from Fig. 9, which were obtained with a constant value of α , we see a spectacular improvement in the reproduction of the experimental data. In particular, the kink in the response curve is now shifted back inside the calorimeter, in excellent agreement with the experimental observations. This reflects the fact that relatively small doses, such as those found beyond the shower maximum, still cause a noticeable increase in the light attenuation.

Not surprisingly, it turns out that the precise location of this kink is very sensitive to the choice of the parameter n . For a given choice of n , the value of α_0 can always be chosen such that the slope of the experimental response curve in the affected region is well reproduced. However, the *size* of this region, i.e. the depth at which the kink is located, depends on n . For example, for $n = 0.5$, the kink is located at $z \approx 13$ cm, while for $n = 0.82$ the kink is barely noticeable, which reflects the fact that even the extremely small doses deposited near the very end of the module contribute significantly to the light attenuation. The best reproduction of the position of the kink (at $z \approx 19$ cm) was found for $n = 0.7$, and the corresponding optimum value of α_0 was 0.010. The simulated response curve for

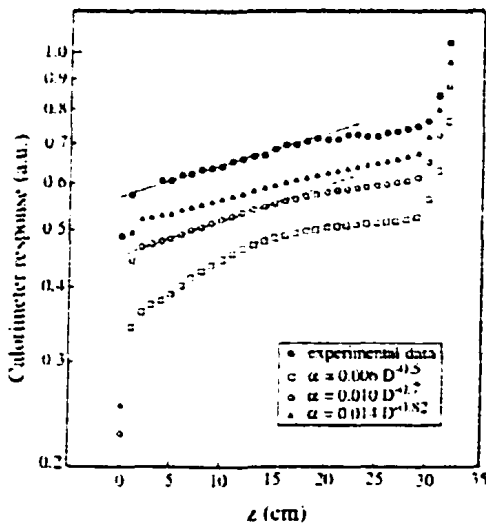


Fig. 10. Simulated response curves along the central axis of the irradiated calorimeter, for different choices of the (dose dependent) parameter α . For comparison, the experimentally measured curve is shown as well. See text for details.

$z = 0.010D^{-0.7}$, i.e. the curve obtained for an induced light attenuation described by

$$\frac{1}{l(z)} = \frac{1}{l_0} + 0.010D(z)^{0.7}, \quad (5)$$

is represented by the open circles in Fig. 10. It is remarkable that a direct measurement of the dose dependence of the *optical transparency* of the fibers yielded a very similar result in the wavelength region $\lambda \sim 450$ nm, where our PMTs reached their maximum sensitivity [10].

4. Consequences for operation at the LHC

In this section, we describe how the observed radiation damage effects will affect the performance of the quartz fiber calorimeter in the LHC era.

Once the relationship between the radiation dose and the resulting induced light attenuation has been established, the local attenuation length of the fibers can be calculated for any point inside the calorimeter, on the basis of the locally accumulated radiation dose (Eq. (5)). These doses have been calculated in great detail for the CMS experiment [1].

For example, Fig. 11 shows the dose profiles at $|\eta| = 3, 4$ and 5, as a function of depth inside the quartz fiber calorimeter, accumulated during 10 years of LHC operation. We assumed a total integrated luminosity of $\int \mathcal{L} dt = 1000 \text{ fb}^{-1}$ for these calculations.

As a typical object of interest in this kinematic region, we consider a 100 GeV π^0 , which shows up as two 50 GeV photon showers in the HF calorimeter. We have studied the calorimeter response and the energy resolution for such showers, at $|\eta| = 4$ and 5, as a function of time, assuming a constant luminosity.

The photon showers were simulated with EGS4. First, the response curve of the fibers was calculated as follows. On the basis of the applicable dose profile (see Fig. 11) and the dose dependent α values, the depth dependent attenuation length $l(z)$ was derived, using Eq. (5). Then, the response curve $R(z)$ was calculated in the same way as for the z -scans (see Section 3.3.2, Fig. 10), except that

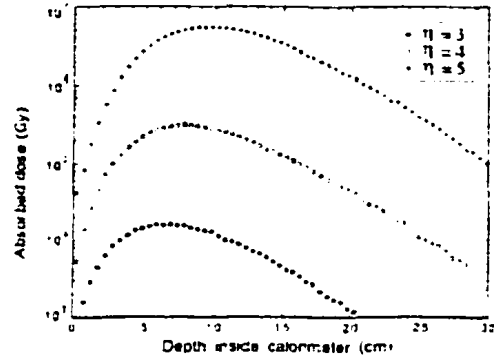


Fig. 11. Expected dose profiles in the HF calorimeter of CMS, accumulated in 10 years of running, for $|\eta| = 3, 4$ and 5.

in this case most of the Cerenkov light was assumed to be trapped in one direction ($\pm z$; see Fig. 2) and traveled directly to the PMTs. In other words, backward emitted Cerenkov light reflected against upstream mirrors was given a smaller weight than in the case of the z -scans. Direct and reflected light were assumed to account for 80% and 20% of the signals, respectively, in accordance with measurements performed on a different prototype calorimeter of the same composition [3].

In the EGS4 simulations of the 50 GeV γ shower development, energy deposited at a depth z inside the calorimeter was weighted by a factor $R(z)$, to account for the effects of light attenuation resulting from induced radiation. The calorimeter was considered a massive block of copper in these simulations, so that variations in the absorbed (weighted) energy were uniquely caused by the effects studied here (and not by the effects of sampling fluctuations and other factors determining the signals of real calorimeters).

Some results of this study are shown in Fig. 12. In Fig. 12(a), the average calorimeter signal from 50 GeV γ s is shown as a function of time (i.e., integrated radiation dose), for photons entering the quartz fiber calorimeter at $|\eta| = 4$ and 5, respectively. Fig. 12(b) shows the effects of the accumulating dose on the widths of these signal distributions. The horizontal axis is plotted on a scale linear in $N^{0.3}$, where N stands for the number of years of LHC operation. As may be expected,

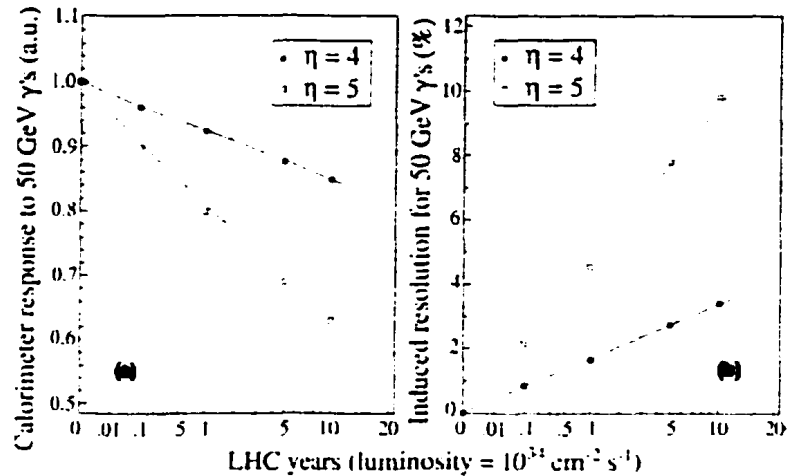


Fig. 12. The expected calorimeter response (a) and energy resolution (b) for 50 GeV γ s entering the calorimeter at $\eta = 4$ or 5, as a function of time during LHC operation at the nominal luminosity. The horizontal axis is plotted on a scale linear in $N^{0.1}$, where N stands for the time of LHC operation. See text for details.

the results scale with $N^{0.1}$, which is indicated by the fact that the data points are well described by straight lines in this figure.

Over the lifetime of the experiment, the calorimeter response to 50 GeV γ s may be expected to decrease by about 35% at $\eta = 5$ and by about 15% at $\eta = 4$, as a result of increased light attenuation in the quartz fibers caused by exposure to ionizing radiation. This radiation will also increase the energy resolution, by inducing an extra term which in first approximation is independent of energy. This term amounts to 10% for $\eta = 5$ and 3.5% for $\eta = 4$, after 10 years of LHC operation, and adds in quadrature to the resolution of the unirradiated instrument.

It is important to realize that about half of the mentioned effects occurs during the first year of operation, one-quarter even occurs during the first month. This is a direct consequence of the dose dependence of the radiation hardness parameter α . The relatively small integrated doses received in the first year have a disproportionately large effect on the calorimeter performance.

In the simulations described in this section, we have assumed that the effects observed in our irradiation studies of the calorimeter prototype are

the only ones to play a role. However, in practice there will also be other effects that contribute to radiation damage and its consequences for the CMS measurements. We mention two such effects:

- We have assumed that only the em showers generated by π^0 s and other electromagnetically decaying particles generated in the LHC interactions contribute to the radiation damage profiles. In practice also charged hadrons contribute. Since the energy carried by these particles is typically deposited in an area that is much larger than that in which em showers deposit their energy, the dose levels in the hadronic calorimeter section are correspondingly smaller. However, light generated in the em calorimeter section will also have to traverse this hadronic section before it reaches the PMTs and some additional absorption will inevitably occur.
- We have ignored recovery effects in the irradiated fibers or at least the recovery that occurs on a time-scale longer than a few days. Recovery from irradiation is a complicated process, details of which depend on the type and duration of the irradiation. The effects are also strongly wavelength dependent.

These effects work in opposite directions. By leaving out the irradiation of the hadronic calorimeter section, our simulations *underestimate* the total impact of the irradiation in the LHC environment, while by ignoring recovery effects we have *overestimated* the consequences of radiation. A detailed study of effects such as those mentioned above might lead to some corrections of our results (as summarized in Fig. 12), but would not change the essence of our conclusions.

5. Conclusions

In this study, we have tried to quantify the effects of the very large radiation doses that are expected to be accumulated in the forward (HF) calorimeters of the CMS experiment. The ionizing radiation increases the light attenuation in the quartz fibers. The more the radiation received, the shorter the attenuation length becomes. As a result, the calorimeter response decreases over time, and the energy resolution deteriorates. The latter effect is the result of event-to-event fluctuations in the depth profile of the energy deposited by the showering particles. We have measured that the signal reduction for 50 GeV γ showers amounts to $\sim 35\%$ in the “hottest” area, $\eta = 5$. The energy resolution for such photons was found to increase by $\sim 10\%$ in this region, over the lifetime of the experiment.

Most of the radiation damage effects occur during the first year of operation. This is a consequence of the dose dependent characteristics of the radiation damage in this type of detector. Therefore, the best way to deal with these effects in practice is to carefully monitor the calorimeter performance during operation and apply appropriate corrections to the experimental data.

The radiation damage process causing the mentioned effects is distinctly different from that in plastic scintillators. The radiation hardness parameter α , which is more or less constant for the latter, was found to depend strongly on the radiation dose levels in the quartz fibers used in this study. This effect is studied in more detail, e.g., as a function of the wavelength of the Čerenkov light,

in a future publication, in which also a variety of candidate fibers for the CMS detector are compared in terms of their radiation hardness characteristics.

Acknowledgements

We would like to thank our colleagues from CMS, and in particular J. Bourotte and M. Haguenaue, for their interest and assistance in the various tests described in this paper. We are grateful to N. Doble, who provided us with particle beams of excellent quality. This project was carried out with financial support from CERN, the US Department of Energy, RMKI-KFKI (Hungary, OTKA grant T 016823), the Scientific and Technical Research Council of Turkey (TÜBİTAK), CICYT (Spain, grant AEN96-2051-E), the International Science Foundation (grants M82000 and M82300), the State Committee of the Russian Federation for Science and Technologies, and the Russian Research Foundation (grant 95-02-04815). We gratefully acknowledge the legacy of Nelson, Hirayama and Rogers [5], whose EGS4 program continues to prove invaluable in planning, preparing for and analyzing data of almost every experiment in high-energy particle physics these days.

References

- [1] CMS Collaboration, report CERN/LHCC 97-31, CERN, Geneva, Switzerland, 1997.
- [2] P. Gorodetzky, *Rad. Phys. Chem.* 41 (1993) 253.
- [3] N. Akchurin et al., *Nucl. Instr. and Meth. A* 399 (1997) 202.
- [4] N. Akchurin et al., *Nucl. Instr. and Meth. A* 408 (1998) 380.
- [5] W.R. Nelson, H. Hirayama, D.W.O. Rogers, EGS 4, SLAC Report 165, 1978, Stanford.
- [6] N. Akchurin et al., *Nucl. Instr. and Meth. A* 471 (2001) 303.
- [7] U. Holm, K. Wick, *IEEE Trans. Nucl. Sci.* 36 (1989) 579.
- [8] D. Acosta et al., *Nucl. Instr. and Meth. B* 62 (1991) 116.
- [9] See for example D.L. Griscorn et al., *Phys. Rev. Lett.* 71 (1993) 1019, and references therein.
- [10] I. Dumanoglu et al., Internal Note CMS 2001/20, CERN, Geneva, Switzerland, 2001.

APPENDIX B

EFFECTS OF RADIATION AND THEIR CONSEQUENCES FOR THE
PERFORMANCE OF THE FORWARD CALORIMETERS IN THE CMS
EXPERIMENT (REPRINTED WITH PERMISSION FROM NUCLEAR
INSTRUMENTS AND METHODS, B187 (2002) 66)



ELSEVIER

Nuclear Instruments and Methods in Physics Research A 487 (2002) 381–395

**NUCLEAR
INSTRUMENTS
& METHODS
IN PHYSICS
RESEARCH**
Section A

www.elsevier.com/locate/nima

Intercalibration of the longitudinal segments of a calorimeter system

M. Albrow^a, S. Aota^b, G. Apollinari^a, T. Asakawa^b, M. Bailey^c, P. de Barbaro^d,
V. Barnes^e, D. Benjamin^f, S. Blusk^d, A. Bodek^d, G. Bolla^e, H. Budd^d, D. Cauz^g,
L. Demortier^h, Y. Fukuiⁱ, Y. Gotra^j, S. Hahn^h, T. Handa^k, K. Hatakeyama^h,
H. Ikeda^b, G. Introzzi^l, J. Iwai^m, S.H. Kim^b, A. Königterⁿ, W. Kowald^o,
A. Laasanen^c, J. Lamoureux^p, M. Lindgren^q, J. Liu^d, O. Lobban^{r,*}, P. Melese^h,
H. Minato^b, S. Murgia^f, H. Nakada^b, J. Patrick^a, G. Pauletta^g, W. Sakumoto^d,
L. Santi^g, Y. Seiya^b, A. Solodsky^h, L. Spiegel^a, T. Thomas^c, R. Vilar^s,
A.M. Walsh^t, R. Wigmans^f

^a Fermi National Accelerator Laboratory, Batavia, IL, USA

^b University of Tsukuba, Japan

^c University of New Mexico, Albuquerque, NM, USA

^d University of Rochester, Rochester, USA

^e Purdue University, Lafayette, USA

^f Texas Tech University, Lubbock, USA

^g Università di Udine e Sezione INFN di Trieste, Italy

^h Rockefeller University, New York, USA

ⁱ KEK, Tsukuba, Japan

^j University of Pittsburgh, Pittsburgh, USA

^k Hiroshima University, Hiroshima, Japan

^l Università e Sezione INFN di Pavia, Italy

^m Waseda University, Tokyo, Japan

ⁿ Universität Karlsruhe, Germany

^o Duke University, Durham, USA

^p Brunel University, Uxbridge, USA

^q University of California at Los Angeles, USA

^r Michigan State University, East Lansing, USA

^s Universidad de Cantabria, Santander, Spain

^t Rutgers University, Piscataway, USA

Received 15 August 2001; received in revised form 30 October 2001; accepted 14 November 2001

Abstract

Three different methods of setting the hadronic energy scale of a longitudinally segmented calorimeter system are compared with each other. The merits of these methods have been studied with testbeam data from the CDF Plug

*Corresponding author. CDF-Texas Tech University, Fermilab, M.S. 318, P.O. Box 500, Batavia, IL 60510, USA. Tel.: +1-630-844-2114.

E-mail address: olobban@fnal.gov (O. Lobban).

0168-9002/02/\$ - see front matter © 2002 Elsevier Science B.V. All rights reserved.
PII: S0168-9002(01)02190-3

Upgrade Calorimeter. It turns out that one of the (commonly used) calibration methods introduces a number of undesirable side effects, such as an increased hadronic signal nonlinearity and trigger biases resulting from the fact that the reconstructed energy of hadrons depends on the starting point of their showers. These problems can be avoided when a different calibration method is used. The results of this study are applied to determine the e/h values of the calorimeter and its segments. © 2002 Elsevier Science B.V. All rights reserved.

PACS: 29.40.Mc; 29.40.Vj

Keywords: Calorimetry; Calibration; Jets; Linearity; Compensation

1. Introduction

The calibration of calorimeters is a crucial ingredient in the commissioning of detectors in modern particle physics experiments. The calibration constants, which define the relationship between the calorimeter signals and the energy of the particles that produced these signals, are typically determined by exposing (some fraction of) the calorimeter modules to particle beams of known composition and energy.

When the calorimeter is longitudinally segmented, e.g., in two sections, this procedure is subject to complications, which are the subject of the present study. The complications encountered when particle showers develop across the boundaries between calorimeter modules derive from two factors:

1. Noncompensation, i.e. the calorimeter responds differently to electromagnetic and nonelectromagnetic energy deposit ($e/h \neq 1$).
2. The calorimeter response, which we define as the average signal divided by the deposited shower energy, varies with the shower age, i.e. with the depth inside the absorber. This is a consequence of the fact that the sampling fraction for different types of shower particles may be very different and the fact that the composition of the shower changes considerably as it develops [1]. This effect plays a role in all types of showers.

The present study was carried out with testbeam data from the new endplug calorimeter of the Collider Detector at Fermilab (CDF). This calorimeter system was recently modified as part of the

upgrade program in preparation for Tevatron Collider Run II, and it was therefore appropriate to evaluate the calibration procedures. In doing so, we took advantage of insights gained during previous studies that were carried out in the context of the SSC LHC detector R&D [2].

This paper is organized as follows. In Section 2, the different calibration methods we have studied are described in some detail. In Section 3, the detector and the testbeam data that were used to investigate the merits of these methods are described. The different procedures that were used to set the energy scale of the calorimeter sections are described in Section 4. Experimental consequences of the different calibration methods are discussed in Section 5. The experimentally observed hadronic response nonlinearities may be used to determine the degree of noncompensation of the calorimeter and its components. This is the topic of Section 6, in which these e/h values are also compared to those of calorimeters with a similar structure. Conclusions are given in Section 7.

2. The calibration methods

In this section, we discuss three methods to calibrate a longitudinally subdivided calorimeter system. Each method is based on a certain philosophy, which we will mention, as well as the resulting problems.

2.1. Method 1

In this method, which is the basis for calibrating several calorimeter systems, the longitudinal

segments are *individually* calibrated. For the towers of the EM section, electrons with precisely known energies are used, while the HAD section is calibrated with hadrons that penetrate the EM section without undergoing a strong interaction¹.

The philosophy behind this method is to establish the calibration constants for each section with the type of particles that are in practice producing the signals in that section: electrons for the EM compartment, hadrons for the hadronic compartment. In this way, one hopes to eliminate the problems arising from the fact that the calorimeter response to these particles is different in noncompensating calorimeters. In most calorimeters, the response to hadrons is smaller than that to electrons of the same energy ($e, h > 1$). Therefore, if electrons were sent into the hadronic section of a calorimeter calibrated in this way, their energy would be measured, on average, too high.

This calibration method works fine for the hadrons that penetrate the EM section without interacting. However, this sample usually represent only a small fraction of all hadrons. Most hadrons undergo their first nuclear interaction in the EM calorimeter section. They deposit part of their energy in the EM section and the remainder in the HAD section. For these events, this calibration method does not produce correct results.

2.2. Method II

In this method, the calibration constants of both calorimeter sections are established with the same type of particles. The underlying philosophy of this method is that the relationship between deposited energy and resulting calorimeter signal should be established in the same way for all segments of the calorimeter system. This principle is applied in a variety of experiments. In practice, one uses muons [3], radioactive sources [4] or discharging capacitors (in the case of liquid-argon calorimeters) for this purpose.

In our case, we used a beam of high-energy electrons, sent directly into the hadronic calorimeter section, to test the merits of this method.

This has the advantage that the method used to set the energy scale for the EM section is essentially copied for the HAD section. In practice, this method is usually impossible to implement in an experiment, since the HAD section is shielded from the particle source (i.e., the interaction region) by the EM section. However, in our testbeam setup we could study this method thanks to the fact that part of the tested calorimeter was *not* equipped with an EM section.

2.3. Method III

In this method, which to our knowledge has not yet been applied in any experiment, pions with a well-defined energy are used to intercalibrate the EM and HAD calorimeter sections. The calibration constant for the EM section is, as usual, determined with electrons of known energy, while the calibration constant for the HAD section is chosen such that the average energy reconstructed for penetrating pions is equal to that for non-penetrating pions.

The underlying philosophy of this method is to avoid any dependence of the reconstructed (hadronic) energy on the starting point of the showers. As we will see later, such a dependence, and the associated trigger biases, are an inevitable consequence of the application of Method I. Unlike Method II, this method has the advantage that it can be implemented in practice and that it can be applied *in situ* using reconstructed tracks of isolated particles produced in the interactions studied by the experiment.

3. Experimental data

3.1. The CDF Plug Upgrade calorimeter

The CDF Plug Upgrade calorimeter is a new detector that has recently been installed for Tevatron Run II. It covers the pseudorapidity range from 1.1 to 3.6 and replaces the original gas-based calorimeter. The new detector consists of a $0.75\lambda_{\text{int}}$ deep EM section and a $7.4\lambda_{\text{int}}$ deep HAD section (at $\theta = 23^\circ$). The EM section has a lead,

¹ We will refer to such particles in the following as *penetrating pions*. Nonpenetrating pions start showering in the electromagnetic section of the calorimeter.

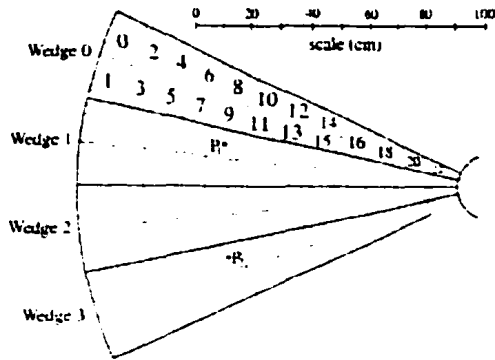


Fig. 1. Tower structure of the Plug Upgrade testbeam module. Wedge 3 was built without an EM section. The numbers inside the tower boundaries correspond to those used in the text. The testbeam particles traveled perpendicular to the plane of this page. They entered the calorimeter typically in point P_+ , except for Method II, when they were sent into point P_- .

scintillator sandwich structure, with 4.5 mm thick lead plates alternated by 4.0 mm thick plastic scintillator plates. In the HAD section, 6.0 mm thick scintillator plates are sandwiched between 50.8 mm thick iron absorber plates. The signals are read out by means of wavelength shifting optical fibers, which are embedded in the scintillator plates. More details about this device are given in Ref. [5].

In this study we have used experimental data taken with a special module that was built for testbeam purposes. This module consists of four 15° sections which are replicas of the actual Plug Upgrade calorimeter (see Fig. 1). One of these four wedges was built without an EM compartment. It is this feature that made it possible to study calibration Method II.

3.2. Testbeam setup

The calorimeter module described in the previous subsection was tested in the MT6 beamline at Fermilab. It was exposed to beams of electrons, pions and muons with energies ranging from 5 to 170 GeV. The momenta of the beam particles were determined event-by-event by means of Single Wire Drift Chambers located upstream and down-

stream of the last dipole magnet, ~ 30 m upstream of the test calorimeter. The relative precision of this momentum measurement ($\Delta p/p$) varied between 1.8% at 5 GeV/c and 1.1% at 150 GeV/c.

Several auxiliary detectors in the beamline were used to ensure clean event samples. These included

- A *Preshower Detector*, consisting of a 1X₀ thick lead plate followed by a plastic scintillator tile. This device was very effective in rejecting electron contamination from pion beams, which was essential at low energies.
- *Muon counters* located downstream of the test module, behind 82_{cm} of steel absorber. These detectors were crucial for removing muon contamination from electron and pion beams, and were also used to ensure pure muon event samples.
- A *veto counter* was used to eliminate events in which the beam particle had started to shower upstream of the calorimeter. This detector was also used to identify and reject events in which more than one beam particle entered the calorimeter simultaneously, i.e. within the time resolution of the detector.

More details about the characteristics of these and other beamline elements and about the quality of the MT6 particle beams are given in Ref. [6].

3.3. Data acquisition

The calorimeter data were read out with a custom designed front-end electronics system described in Ref. [7]. The ADCs had a full range of 750 pC and a sensitivity of 11.4 fC/count. They were operated at a gate width of 2.2 μ s. The particle signals were determined by subtracting "in-spill" pedestals from the raw numbers of ADC counts. Pedestal fluctuations were typically of the order of a few ADC counts (40 fC).

3.4. Gain equalization

When a shower develops in this calorimeter, the total signal consists typically of a large contribution from the tower in which the particle entered the detector, plus significant contributions from a number of neighboring towers. The relative

contributions from these neighbors depend on the energy, the impact point and the type of beam particle. In order to determine the total signal, it is crucial that the gains of all the towers contributing to the signal be equal.

When electrons were steered into the center of a calorimeter tower, they deposited typically more than 90% of their energy in that tower. Electrons would therefore be well suited to equalize the gains of the EM calorimeter towers. However, during the beam tests only a limited number of towers were exposed to electron beams. Not all calorimeter towers could therefore be calibrated this way.

The only type of particles that were sent into each and every tower of the calorimeter were muons. Since these muons deposit an equal amount of energy in every tower (after taking into account the effects coming from differences in path length), they can be used to equalize the gains of the towers. We fit the signal distributions (in ADC counts) from muons in each EM and each HAD calorimeter tower with a Landau function and determined the most probable signal value for each distribution. All PMT gains were normalized to those of Wedge 1, Tower 8 (see Fig. 1). This was done separately for the EM and the HAD towers. The most probable value of the signal distribution from EM tower i was multiplied by a "tower gain constant tg_i ," so that all EM towers responded to muons like the EM section of the reference tower. The same procedure was followed for the towers from the hadronic calorimeter section, which thus all responded to muons in the same way as the HAD section of Wedge 1, Tower 8.

We verified the validity of this procedure for those towers that had been exposed to electrons. Fig. 2 shows the tg_i values found with muons plotted versus the tg_i values found with electrons, for all EM calorimeter towers that had been exposed to both types of particles. Because of the strong correlation between these two sets of constants, we conclude that the gain constants found with muons (which deposit typically only 0.3 GeV in the EM calorimeter towers) are also valid for the signals from showering electrons, whose energy deposit is typically two orders of magnitude larger. Throughout the remainder of

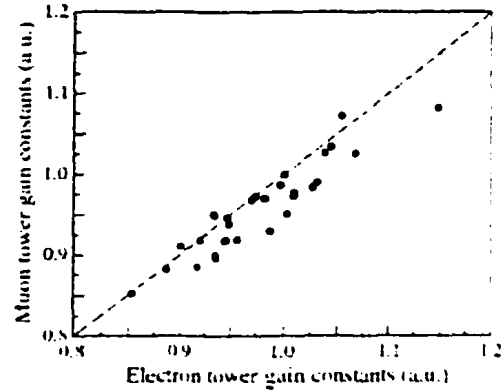


Fig. 2. Tower gain constants found from muon runs versus those found from electron runs. Each point represents one EM calorimeter tower. The gains are normalized with respect to Tower 8 of Wedge 1.

this analysis, we have applied the tg_i values found with muons to equalize the gains of the calorimeter towers, both in the EM and the HAD section.

4. Determination of the energy scales

4.1. The energy scale of the EM section

We determined the energy scale of the EM calorimeter section, A , as

$$A = \frac{\langle \sum_i (em_i - ped_i^{em}) tg_i^{em} \rangle}{E_e} \quad (1)$$

where em_i , ped_i^{em} and tg_i^{em} are the measured signal, the pedestal and the tower gain constant for tower i of the EM calorimeter section, respectively, and E_e is the energy of the electron beam. Electrons with energies ranging from 8 to 180 GeV were used for this purpose, and we summed the signals over a 5×5 matrix of calorimeter towers surrounding the tower hit by the beam particles.

Fig. 3 shows the value of A as a function of the electron beam energy. The error bars in this figure, as well as in the figures showing the hadronic calibration constants, are dominated by the effect of a systematic uncertainty in the gains of the

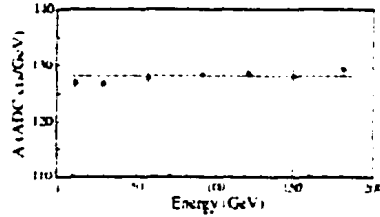


Fig. 3. The energy scale for the EM calorimeter section, A , as a function of energy.

PMTs during the beam tests, which was estimated at 1%. Other sources of uncertainty include statistical errors and errors deriving from the gain equalization procedure (see Section 3.4, Fig. 2). However, since all neighboring towers combined generate typically only $\sim 10\%$ of the signals from electron showers, the effect of the latter source of uncertainty is negligibly small. Our results show that the value of A is constant within the experimental uncertainties, over a wide range of electron energies. The weighted average was found to be: $A = 128.1 \pm 0.5 \text{ cts/GeV}$ ($A^{-1} = 7.81 \pm 0.03 \text{ MeV per ADC count}$).

4.2. The energy scale of the HAD section

4.2.1. Method I

In this method, we used pions sent into the EM section of the calorimeter as the basis for determining the energy scale of the HAD section. The particle beams were steered into the center of Tower 8, Wedge 1 (point P_1 in Fig. 1), and only pions which penetrated the EM section without undergoing a nuclear reaction (i.e., without starting a shower) were selected for this purpose. The energy scale of the HAD section, B_I , was then defined as

$$B_I = \frac{\langle \sum_i (\text{had}_i - \text{ped}_i^{\text{had}}) (g_i^{\text{had}}) \rangle}{\langle E_\pi - E_{\text{em}} - E_{\text{leak}} \rangle} \quad (2)$$

where had_i , $\text{ped}_i^{\text{had}}$ and g_i^{had} are the measured signal, the pedestal and the tower gain constant for tower i of the HAD calorimeter section, respectively. E_π is the energy carried by the pions, while E_{em} and E_{leak} denote the energy deposited by the mip-like pion in the EM calorimeter section and

the energy leaking out the back of the calorimeter, respectively. The latter term is energy dependent.

We obtained E_{em} from the signals produced by the penetrating pions in the EM calorimeter section. The average values are listed in Table 1 for the various pion runs that were used in this context. These covered an energy range from 8 to 170 GeV. The calorimeter module is about $8\lambda_{\text{int}}$ deep at Tower 8. This is not deep enough to fully contain the high-energy pion showers. In order to estimate the energy leaking out from the back of the calorimeter, we used experimental data taken by the WA1 Collaboration at CERN [8]. They measured the average energy fraction deposited by showering pions in each of 14 consecutive iron plastic-scintillator segments, for pions with energies ranging from 10 to 137 GeV. On the basis of these data, we estimated the (E_{leak}) values listed in Table 1.

The last column of Table 1 lists the resulting values of the calibration constant for the hadronic calorimeter section, B_I .

Fig. 4 shows the value of B_I obtained in this way as a function of the energy deposited in the hadronic calorimeter section by the penetrating pions. Note the logarithmic scale of the horizontal axis. The value of B_I increases with energy, which means that the (hadronic section of the) calorimeter is intrinsically nonlinear for pion detection. This nonlinearity amounts to $\sim 10\%$ when comparing the lowest and highest pion energies used for our tests.

4.2.2. Method II

In this method, we used electrons which were directly sent into the HAD section of the calorimeter to establish the energy scale for this section. Wedge 3 of the calorimeter testbeam module was built without an EM section, and thus made it possible to use this calibration method. The electron beams were steered into the center of Tower 8, Wedge 3 (point P_2 in Fig. 1). The energy scale of the HAD section determined with this method, B_{II} , was then found as

$$B_{II} = \frac{\langle \sum_i (\text{had}_i - \text{ped}_i^{\text{had}}) (g_i^{\text{had}}) \rangle}{E_e} \quad (3)$$

Table 1

The average energy deposited in the EM calorimeter section, the average energy leaking out the back of the calorimeter and the average energy deposited in the hadronic calorimeter section are listed for penetrating pions of different energies. All energies are given in units of GeV. The resulting value of the calibration constant for the hadronic calorimeter section, B_{II} , is listed in the last column.

| Pion energy | $\langle E_{em} \rangle$ | $\langle E_{leak} \rangle$ | $\langle E_{\pi} - E_{em} - E_{leak} \rangle$ | B_{II} (cts./GeV) |
|-------------|--------------------------|----------------------------|---|---------------------|
| 3.64 | 0.3 ± 0.1 | 0 | 3.3 ± 0.1 | 144.1 |
| 12.2 | 0.3 ± 0.1 | 0 | 11.9 ± 0.1 | 145.5 |
| 28.7 | 0.3 ± 0.1 | 0.4 ± 0.1 | 28.0 ± 0.1 | 147.3 |
| 57.0 | 0.3 ± 0.1 | 1.6 ± 0.3 | 56.0 ± 0.3 | 151.4 |
| 90.3 | 0.3 ± 0.1 | 3.8 ± 0.8 | 86.2 ± 0.8 | 156.1 |
| 177.0 | 0.3 ± 0.1 | 10.2 ± 2.0 | 166.4 ± 2.0 | 158.5 |

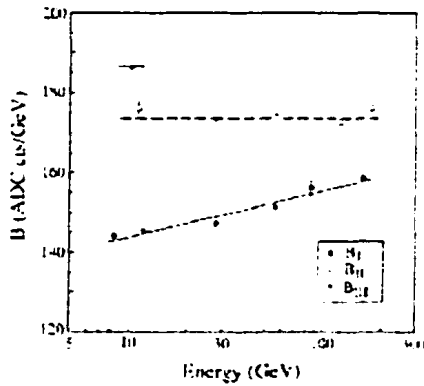


Fig. 4. The energy scale for the hadronic calorimeter section, B , as a function of energy, for the three calibration methods used in this analysis. The lines through the experimental points are drawn to guide the eye. See text for details.

where had_i , ped_i^{had} and tg_i^{had} are the measured signal, the pedestal and the tower gain constant for tower i of the HAD calorimeter section, respectively, and E_{π} is the energy of the electron beam.

Electrons with energies ranging from 11 to 177 GeV were used to determine the value of B_{II} , which is shown as a function of the electron energy in Fig. 4. The value of B_{II} was found to be constant within experimental errors ($\pm 2\%$) for a wide range of energies. This reflects the intrinsic linearity of the HAD section for electromagnetic shower detection. The average value was found to be significantly higher than the values

found with Method I: $B_{II} = 173.5$ cts./GeV ($B_{II}^{-1} = 5.76$ ADC cts./GeV).

4.2.3. Method III

As in Method I, pions sent into (point P_1) of the EM calorimeter section were used to determine the energy scale of the hadronic calorimeter section. However, this time the calibration constant, B_{III} , was chosen such that the energy reconstructed for penetrating pions would be equal to the energy reconstructed for nonpenetrating pions. In order to avoid the effects of shower leakage, which would primarily affect the results for the penetrating pions and thus bias the results, we only used low-energy (< 20 GeV) pion runs to find the value of B_{III} , which needed to satisfy the condition

$$\begin{aligned}
 B_{III}^{pen} &= \frac{\langle \sum_i (had_i - ped_i^{had}) tg_i^{had} \rangle}{E_{\pi} - E_{em}} \\
 &= B_{III}^{nonpen} \\
 &= \frac{\langle \sum_i (em_i - ped_i^{em}) (tg_i^{em} - (had_i - ped_i^{had}) tg_i^{had}) \rangle}{E_{\pi}}
 \end{aligned} \quad (4)$$

The average value for which this condition was fulfilled was found to be: $B_{III} = 186.5$ cts./GeV ($B_{III}^{-1} = 5.36$ ADC cts./GeV). This result is also included in Fig. 4.

4.3. Reconstructed energy for hadrons and jets

Having discussed the various methods to set the energy scale of the hadronic calorimeter section,

we can now define the reconstructed energy for a given hadron or jet as

$$E_{\text{reco}} = \sum_i \frac{(em_i - ped_i^{\text{em}})t_{\text{tr}}^{\text{em}}}{A} - \frac{(\text{had}_i - ped_i^{\text{had}})t_{\text{tr}}^{\text{had}}}{B_{\text{I,II,III}}} \quad (5)$$

where all symbols have the same meaning as before. If we chose Method I to set the energy scale of the HAD section, we would need to specify the energy at which the calibration constant B_I was determined, since this value is energy dependent. Depending on the energy, the value of B_I may change by as much as 10% (see Table 1, Fig. 4). The other two methods are based on energy-independent calibration constants. In practice, we used a value $B_I = 151.4 \text{ cts/GeV}$ for our studies of the implications of Method I, i.e. the value obtained for the 56 GeV point and an approximate average of all the values obtained over the energy range we studied.

5. Experimental consequences of (mis)calibration

In order to evaluate the merits of the different calibration methods, we concentrated on two aspects:

1. Biases based on the starting point of the showers.

In experiments with highly selective triggers such biases are an undesirable feature. Many variables that involve the reconstructed hadronic energy (e.g., the total transverse energy or the missing transverse energy) exhibit a steeply falling distribution. If one triggers on the value of such a variable, most of the selected events are thus located near the trigger threshold. Biases of the type mentioned here would lead to event samples that are predominantly populated by events that were actually below the trigger threshold, but which have a *topology* that brings them above that threshold. As examples of such topologies we mention events with pions that start to shower deep in the detector, or jets in which an anomalously large energy fraction is carried by γ 's from π^0 decay. If the energy of such events were systematically

overestimated at the trigger level, then the collected event samples would be biased.

2. *Hadronic signal nonlinearity.* This is an undesirable feature for any detector, since it may also lead to systematic energy mismeasurement for certain categories of events. Hadronic signal nonlinearity means, for example, that the calorimeter signal from a jet containing one 50 GeV pion is systematically larger than that of a jet in which the 50 GeV is shared by several lower-energy pions. In practice, the difference between these topologies is not always evident from the experimental data. And at the trigger level, such effects may cause the same kind of biases as discussed above.

It turned out that the calorimeter performance in this respect is quite sensitive to the choice of the calibration method.

5.1 Single hadrons

5.1.1. Dependence on the starting point of the showers

We studied the implications of the various calibration methods with events collected in the 8.6 GeV pion beam. We split these events into two samples, based on the starting point of the showers: The penetrating and the nonpenetrating events.

Fig. 5 shows the reconstructed energy distributions for these two event samples, obtained on the basis of Method I, using $B_I = 151.4 \text{ cts/GeV}$. The mean values of these two distributions differ by 15%. Had we used a smaller value for B_I , e.g., 144 cts/GeV as suggested by Table 1, then the difference between these two mean values would have been even larger.

Fig. 6 shows the signal distributions for the same event samples, but this time Method III has been used to calculate the reconstructed energy ($B_{\text{III}} = 186.5 \text{ cts/GeV}$). In this case, the mean values of the reconstructed energies of the penetrating and the nonpenetrating pions were found to be equal within the experimental uncertainties (a small fraction of 1%). When Method II was used, the mean values differed by $\sim 5\%$.

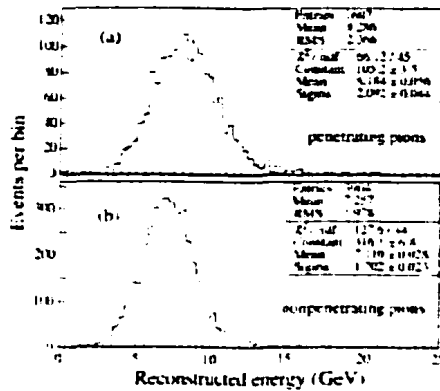


Fig. 5. The reconstructed energy distributions for penetrating (a) and non-penetrating (b) pions of 8.6 GeV, obtained on the basis of Method I, using $B_{II} = 151.4$ ets/GeV.

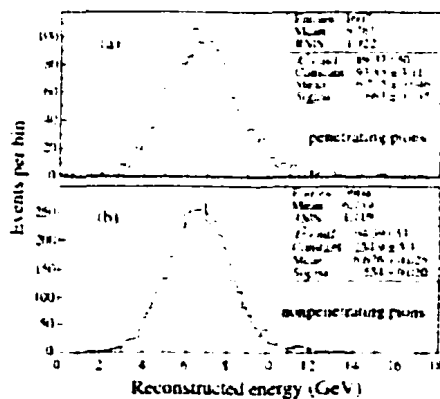


Fig. 6. The reconstructed energy distributions for penetrating (a) and non-penetrating (b) pions of 8.6 GeV, obtained on the basis of Method III, using $B_{III} = 186.5$ ets/GeV.

Method II does not produce the same results as Method III, because the EM and HAD sections of the Plug Upgrade calorimeter have a different composition, which translates into different e/h and e/mip ratios. Therefore, even though the energy scale of both sections is determined with the same particles (electrons in this case), the response to other particles (hadrons, muons) of the two calorimeter sections may be different. And this

results, among other things, in different response functions for penetrating and nonpenetrating pions. If the EM and HAD calorimeter sections had exactly the same structure and composition, then Methods II and III would be completely equivalent and should lead to the same results.

The results described above clearly demonstrate that using Method I to set the energy scale of the HAD section introduces a dependence of the reconstructed pion energy on the starting point of the shower. As a matter of fact, the main motivation to develop Method III was to eliminate this effect.

5.1.2. Signal nonlinearity

For hadron showers, the average energy fraction carried by π^0 's and other particles developing electromagnetic showers (e.g., η 's) increases as a function of energy [1,9]. This causes an *intrinsic* signal nonlinearity for hadrons in *all* noncompensating calorimeters. This intrinsic nonlinearity appears when the pion energy is reconstructed using the calibration constant B_{III} for the signals from the hadronic calorimeter section.

This is shown in Fig. 7, where the ratio of the reconstructed energy and the deposited energy is

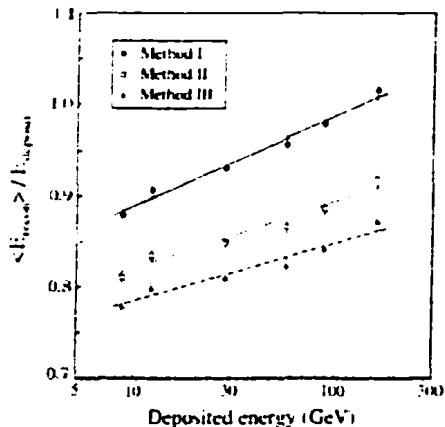


Fig. 7. The ratio of the reconstructed energy and the deposited energy as a function of the energy deposited by pions showering in the CDF Plug Upgrade calorimeter. Results are given for the three calibration methods discussed in the text. The curves through the points are fits to the function in Eq. (7).

plotted as a function of the energy deposited by pions showering in the calorimeter. For a linear calorimeter, this ratio would have to be energy independent. The deposited energy is $E_{\text{depos}} - E_{\text{leak}}$, where E_{leak} is the average energy that all pions (penetrating and nonpenetrating) leak out the back of the calorimeter. This leakage energy was estimated on the basis of the WA1 data [8], in the same way as was done for penetrating pions in Section 4.2.1.

In the following, we will quantify the hadronic signal nonlinearity (ΔR) as the relative change in the calorimeter response between 10 and 100 GeV:

$$\Delta R = \frac{R(100)}{R(10)} - 1 \quad (6)$$

where $R(100)$ is the calorimeter response (i.e. the average signal per GeV, in arbitrary units) for 100 GeV pions and $R(10)$ the response to 10 GeV pions. Based on this definition, the intrinsic nonlinearity of the CDF Plug Upgrade calorimeter was found to be 7.8%.

If we used the calibration constants from Method I to reconstruct the pion energy, then a larger nonlinearity was observed: 11.1% over the energy range from 10 to 100 GeV. This can be understood from the fact that as the energy of the pion shower increases, more and more energy is deposited in the hadronic section of the calorimeter. In Method I, the signals from this calorimeter section are “boosted” with respect to the signals from the EM calorimeter section.

Fig. 7 shows the ratio of the reconstructed energy and the deposited energy as a function of the latter for all three different calibration methods. Each data point represents the mean value of the distribution of E_{recon} (Eq. (5)), where all pions, penetrating and nonpenetrating, have been taken into account. Each data set was fit with the function

$$\frac{\langle E_{\text{recon}} \rangle}{E_{\text{depos}}} = k_1 + k_2 \ln E_{\text{depos}} \quad (7)$$

Table 2 lists the values of the parameters k_1 and k_2 for the different calibration methods, as well as k_2/k_1 , which is a measure of the signal nonlinear-

Table 2

Values of the parameters k_1 and k_2 , from the fit of the experimental data to Eq. (7) which describes the hadronic signal nonlinearity, for each of the three calibration methods described in the text.

| Calibration | k_1 | k_2 | k_2/k_1 |
|-------------|-------|-------|-----------|
| Method I | 0.79 | 0.043 | 0.0544 |
| Method II | 0.74 | 0.033 | 0.0446 |
| Method III | 0.72 | 0.028 | 0.0389 |

ity. The table shows that this nonlinearity is $\sim 40\%$, larger when Method I is used as compared to Method III.

5.2. Consequences for jets

In many modern particle physics experiments, the detection of jets and a proper measurement of their energies is of primary concern. Therefore, we also studied the effects of the different calorimeter calibration methods on the response to jets. Unfortunately, nature does not provide test beams with jets of precisely known energies and, therefore, we had to rely on Monte Carlo simulations for this purpose.

We used a Monte Carlo simulation program that was previously developed as part of calorimeter R&D studies in the context of the SSC-LHC [10]. The intent was to simulate the response of the calorimeter to jets making maximum use of experimental calorimeter signal distributions to individual particles of known energy. In this approach, a jet is treated as a collection of varying number of particles, each with a varying energy and a varying charge. The energy of each jet particle is selected randomly according to a fragmentation function

$$D(z) = (z+1) \frac{(1-z)^z}{z} \quad (8)$$

which well describes a variety of experimental data sets [11]. Here, $D(z)$ denotes the probability that a jet fragment will end up with a fraction z of the jet energy, and z is a parameter. Fragmentation functions measured in the CDF energy range favor a value $z = 6$, which we therefore used in our

simulations. The charge of each jet fragment was chosen randomly so that $\frac{1}{3}$ of the time the fragment was a π^0 and $\frac{2}{3}$ of the time it was a charged pion. For a jet of energy E_{jet} , we randomly pulled n particles from the distribution described by fragmentation function (8) such that $E_{\text{jet}} = \sum_{i=1}^n E_i$, where E_i indicates the energy of the i th fragment. For each jet fragment, we used the measured signal distribution for testbeam pions or electrons of the nearest energy in order to determine what the calorimeter signal would have been had that fragment actually deposited its energy E_i in the calorimeter.

For each jet fragment with energy E_i , we randomly pulled an EM signal, S_i^{em} , and a HAD signal, S_i^{had} , from the corresponding signal distributions for a testbeam run of electrons (if the fragment was neutral) or pions (if the fragment was charged) whose energy was closest to the energy carried by the jet fragment. For instance, for a 10 GeV charged jet fragment, we used the experimental signal distributions for an 8.6 GeV pion testbeam run for that purpose. This jet fragment was then attributed an EM signal $S_i^{\text{em}} = (10/8.6)S_i^{\text{em}}$ and a HAD signal $S_i^{\text{had}} = (10/8.6)S_i^{\text{had}}$, respectively. For a 10 GeV neutral fragment, the same procedure would be followed, but the signals would be taken from an electron run rather than a pion run.

This process was repeated for each of the n fragments that made up the jet of energy E_{jet} . The energy the calorimeter would have reconstructed for this particular jet then is simply

$$E_{\text{reco}} = \sum_{i=1}^n \left[\frac{S_i^{\text{em}}}{A} + \frac{S_i^{\text{had}}}{B_{\text{HAD}}} \right] \quad (9)$$

where the definition of the calibration constants A and B is the same as before.

Fig. 8 shows the response of the calorimeter to jets as a function of energy for the three different calibration methods discussed in the text. For each point, 10000 jets were generated and the calorimeter signal was calculated as described above. The points in Fig. 8 represent the average values of the 10000 signals accumulated this way, normalized to the jet energy.

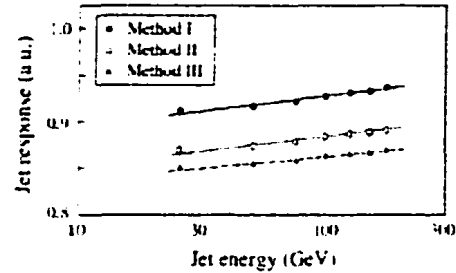


Fig. 8. The jet energy response of the CDF Plug Upgrade calorimeter as found with the Monte Carlo program described in the text. The curves through the points are fits to the function in Eq. (7).

The nonlinearity for jets is clearly smaller than for single pions (c.f. Fig. 7). This is due to two factors:

1. Part of the jet signal, on average one-third, comes from photons which develop electromagnetic showers. The calorimeter is linear for that component of the jet signal. The nonlinearity affects only the remaining portion of the jet fragments.
2. The nonlinearity is not determined by the jet energy itself, but by the *average energy of the jet fragments*. Since the multiplicity increases with energy, this average energy of the fragments rises much more slowly than the jet energy itself.

In spite of this, Fig. 8 exhibits characteristics that are very similar to those observed for single pions. In particular, the slope of the curve for Method III is somewhat smaller than the slope of the curve for Method I. This indicates that the nonlinearity effects described in Section 5.1.2 for single pions propagate into the energy measurements of jets.

The trigger biases discussed in Section 5.1.1 for single pions also have certain consequences for jets. These are spelled out in the next subsection.

5.3. The final energy reconstruction

As can be seen from Fig. 7, the value of the reconstructed energy does not equal the value of

the deposited energy, regardless of which method is used to set the energy scales. In order to arrive at the correct value of the energy deposited by a pion in the calorimeter, one must multiply the reconstructed energy, found according to Eq. (5), by an energy-dependent correction factor, which is simply the inverse of the curves shown in Fig. 7.

Since the correction factor is energy dependent, the final pion energy must be reconstructed in an iterative way:

$$E_{n+1} = (p_1 - p_2 \ln E_n) / E_{\text{recon}} \quad (10)$$

with $E = \langle E_{\text{recon}} \rangle$. The calculation converges very rapidly and typically no more than three iterations are needed.

If this procedure is applied to a sample of pions which includes penetrating and non-penetrating pions in the *same* ratio as in the sample that was used to make Fig. 7 (and the correction factors derived from that sample), then this procedure yields the correct energy for all three calibration methods. If, on the other hand, the procedure is applied to a sample which includes penetrating and non-penetrating pions in a *different* ratio, then it results *only* in the correct energy values when the calorimeter calibration was carried out on the basis of Method III.

This is illustrated in Table 3 for the most extreme case, i.e. separate samples of penetrating and nonpenetrating events. The table shows that Method I leads to a systematic underestimation of the energy of nonpenetrating pions, whereas the energy of penetrating pions is systematically overestimated, by as much as 10% at low energies.

This effect is also important for the energy reconstruction of jets. A jet is essentially a collection of γ 's (from π^0 decay) and hadrons, mostly pions. Most of the jet fragments are very soft, with energies well below 10 GeV, i.e. in the energy range where the effects of systematic energy mismeasurement as a result of miscalibration are largest. Because of the effect discussed above, jets in which a large fraction of the energy is carried by hadronic fragments will, on average, be reconstructed with a systematically lower energy than jets in which most of the energy is carried by γ 's. Soft, early showering hadrons are of less consequence for the total energy reconstruction of the

Table 3

The final energy of pions showering in the CDF Plug Upgrade calorimeter, calculated on the basis of Eq. (10). Results are given for all pions combined and for subsamples of pions that started to shower in the EM or HAD section of the calorimeter

| | 8.6 GeV π beam | 12.2 GeV π beam |
|---|--------------------|---------------------|
| Deposited energy (GeV) | 8.6 | 12.2 |
| E_{HAD} Method I | | |
| All pions | 8.6 \pm 0.1 | 12.3 \pm 0.1 |
| Penetrating | 9.3 \pm 0.1 | 13.2 \pm 0.1 |
| Nonpenetrating | 8.2 \pm 0.1 | 11.9 \pm 0.1 |
| E_{EM} Method II | | |
| All pions | 8.6 \pm 0.1 | 12.3 \pm 0.1 |
| Penetrating | 8.9 \pm 0.1 | 12.6 \pm 0.1 |
| Nonpenetrating | 8.5 \pm 0.1 | 12.2 \pm 0.1 |
| E_{HAD} Method III | | |
| All pions | 8.6 \pm 0.1 | 12.3 \pm 0.1 |
| Penetrating | 8.7 \pm 0.1 | 12.3 \pm 0.1 |
| Nonpenetrating | 8.6 \pm 0.1 | 12.3 \pm 0.1 |

latter type of jets. This problem would be avoided if Method III was used to intercalibrate the EM and HAD calorimeter sections.

6. Determination of the calorimeter's e/h value

All noncompensating calorimeters are intrinsically nonlinear for hadron energy measurements. This is a consequence of the fact that the average fraction of the energy carried by π^0 's produced in the shower development, f_{em} , increases with energy. This energy dependence is well described by

$$f_{\text{em}} = 1 - \left(\frac{E}{E_0} \right)^{k-1} \quad (11)$$

where E_0 is the average energy needed for the production of one pion, and k is related to the average multiplicity per nuclear reaction. Experimental data indicate that $E_0 = 0.7$ and 1.3 GeV for iron and lead, respectively, while $k = 0.82$ gives a good description for both elements [9].

If e and h represent the calorimeter responses to electromagnetic showers and to the nonelectromagnetic component of hadron showers,

respectively, then the response to a pion shower, π , can be written as

$$\pi = f_{em}e + [1 - f_{em}]h \quad (12)$$

so that the π/e signal ratio becomes

$$\frac{\pi}{e} = f_{em} + [1 - f_{em}] \frac{h}{e} \quad (13)$$

Therefore, if the calorimeter is linear for the detection of electromagnetic showers, it can only be linear for pions if $h/e = 1$, i.e. if the calorimeter is compensating.

Knowing the e/h value of the calorimeter, the pion nonlinearity can be calculated in a straightforward way. In this context, we define the nonlinearity through the response ratio of 100 and 10 GeV pions. Fig. 9 shows the relationship between this ratio and the e/h value for sampling calorimeters based on iron or lead as absorber material. For example, an iron calorimeter with $e/h = 1.6$ will exhibit a nonlinearity of 10% (response 100/10 GeV = 1.10).

We can use the measured hadronic nonlinearity to estimate the e/h values of the CDF calorimeters. We have tried to do this separately for the (lead scintillator) EM and (iron scintillator) HAD sections. The nonlinearity of the hadronic compartment follows from the energy dependence of the calibration constant B_1 , which was obtained for showers that deposited their entire energy in this compartment. It was found to be $7.6 \pm 1.3\%$ (see Table 1, Fig. 4). Fig. 9 indicates that the latter

value corresponds to $e/h = 1.44 \pm 0.08$, for the Fe scintillator hadronic calorimeter section.

In Section 5.1.2, we showed that the intrinsic nonlinearity for the entire calorimeter (i.e., EM + HAD sections) was found to be $7.3 \pm 1.1\%$. On average, the energy fraction deposited by the showering hadrons in the electromagnetic Pb scintillator section varied between $\sim 40\%$ at 10 GeV and $\sim 30\%$ at 100 GeV. From this, one can estimate the nonlinearity for an entire calorimeter with the same Pb scintillator structure as this EM section to be $8.3 \pm 4.6\%$. This translates into an e/h value of 1.43 ± 0.27 (see Fig. 9).

Traditionally, the e/h value is determined from the energy dependence of measured e/π signal ratios. We have also used this method as an independent way to check our results. The e/π signal ratios for the iron scintillator calorimeter can be directly derived by comparing the values B_1 and B_H (see Section 4.2). As a matter of fact, the ratio B_H/B_1 is by definition the e/π signal ratio of the hadronic calorimeter section.

Fig. 10 shows this ratio as a function of energy. The curves in this figure represent the expected energy dependence of the e/π signal ratio, for different choices of the e/h value. These curves are the graphical equivalent of Eqs. (11) and (13). From this study, we found the best agreement with the experimental results for $e/h = 1.36$, with a standard deviation of 0.05. Since this experimental result is based on more aspects of the experimental data, it is somewhat more precise than the value derived from the hadronic signal nonlinearity alone. However, both results are within experimental uncertainties equal. In the following, we will use the more precise value derived from the energy dependence of the e/π signal ratios for the iron scintillator section of the calorimeter.

We may compare the e/h values of the CDF Plug Upgrade calorimeter with those of other calorimeters that have the same structure. This is done in Fig. 11, which shows the e/h value of several Fe scintillator (Fig. 11a) and Pb scintillator (Fig. 11b) structures as a function of the sampling fraction.² On the bottom axis, this

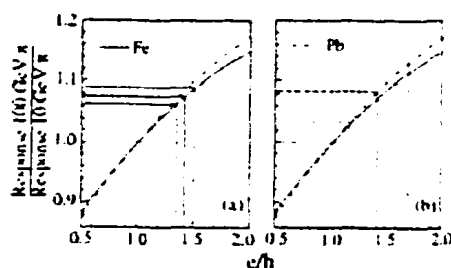


Fig. 9. The ratio of the calorimeter responses to 100 and 10 GeV pions, as a function of the e/h value (12). Experimental data are given for the iron-based HAD section (a) and the lead-based EM section (b) of the CDF Plug Upgrade calorimeter.

²The e/h values displayed in this figure come from Refs. [13,8,14].

sampling fraction is expressed as the volume ratio of the passive and active calorimeter components, R_d . In both cases, the e/h ratio clearly decreases with the sampling fraction (i.e., with increasing R_d), and in the case of Pb/scintillator calorimeters, compensation has even been achieved, for a sampling fraction (for mips) of $\sim 3.5\%$ ($R_d \sim 4.5$) [14].

The R_d values of the CDF Plug Upgrade calorimeter are 1.13 for the electromagnetic lead scintillator section and 8.47 for the hadronic iron-scintillator section. The e/h values of 1.43 ± 0.27 (Pb) and 1.36 ± 0.05 (Fe) are in good agreement with the experimental trend apparent from Fig. 11.

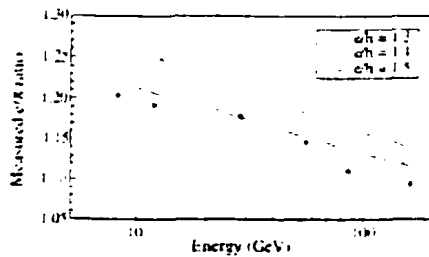


Fig. 10. The experimental e/h signal ratio as a function of energy for the iron-scintillator section of the CDF calorimeter. The curves represent the expected behavior for different values of e/h . See text for details.

The Central CDF calorimeters, although composed of the same structure as the Plug Upgrade, have very different sampling fractions, with R_d values of 0.64 (EM, Pb) and 2.5 (HAD, Fe), respectively. Their e/h values, expected on the basis of the experimental trend, are indicated by dotted lines in Fig. 11. They are considerably more noncompensating than the Plug Upgrade calorimeter. Therefore, the consequences of using calibration Method I should be expected to be correspondingly larger in these Central calorimeters.

7. Conclusions

In this paper, we compare three different methods of setting the hadronic energy scale of a longitudinally segmented calorimeter. The merits of these methods have been studied with testbeam data from the CDF Plug Upgrade calorimeter. It turns out that one of the (commonly used) calibration methods introduces a number of undesirable side effects, such as an increased hadronic signal nonlinearity and trigger biases resulting from the fact that the reconstructed energy depends on the starting point of the hadron showers. These problems are a direct consequence of the noncompensating nature of

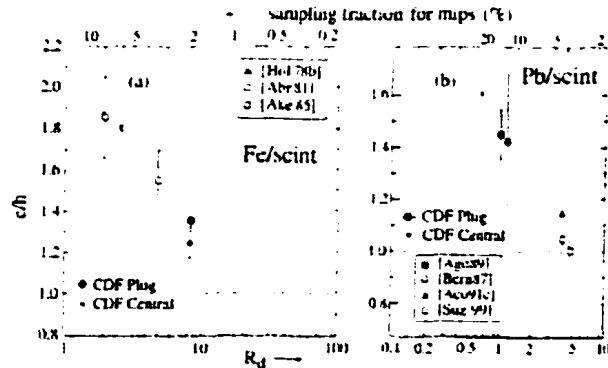


Fig. 11. The e/h value of several Fe scintillator and Pb scintillator calorimeters as a function of the sampling fraction for mips (top axis), or of the volume ratio of passive and active material, R_d (bottom axis) [1]. The dashed line represents the compensation condition ($e/h = 1.0$).

the calorimeters. They can be avoided when a different calibration method is used.

We used the results of this study to determine the e/h values of the calorimeter and its segments. These turned out to be 1.43 ± 0.27 for the EM section and 1.36 ± 0.05 for the HAD section, respectively. We compared these values with those of other Pb scintillator and Fe scintillator calorimeters and found that they were in good agreement with the values expected on the basis of the sampling fraction.

References

- [1] R. Wigmans, Nucl. Instr. and Meth. A 259 (1987) 389.
- [2] O. Ganel, R. Wigmans, Nucl. Instr. and Meth. A 409 (1998) 621.
- [3] T. Åkeson, et al., Nucl. Instr. and Meth. A 262 (1987) 243.
- [4] U. Behrens, et al., Nucl. Instr. and Meth. A 289 (1990) 115.
- [5] CDF Collaboration, The CDF II Technical Design Report, Fermilab Internal Report 96-390-E, unpublished; M. Albrow et al., The CDF Plug Upgrade electromagnetic calorimeter: test beam results, Nucl. Instr. and Meth. A 480 (2002) 524.
- [6] M. Frautschi et al., Yields, composition and particle identification in the 1996 CDF test beam, CDF Internal Note 3195, 1996; P. de Barbaro et al., Particle composition of the MT6 beam tubes for the 1997 CDF test beam, CDF Internal Note 4065, 1997.
- [7] G. Drake, et al., Nucl. Instr. and Meth. A 269 (1988) 68.
- [8] H. Abramowicz, et al., Nucl. Instr. and Meth. A 180 (1981) 429.
- [9] T.A. Gabriel, et al., Nucl. Instr. and Meth. A 338 (1994) 136.
- [10] O. Ganel, R. Wigmans, Nucl. Instr. and Meth. A 365 (1995) 104.
- [11] D. Green, Dijet spectroscopy at high luminosity, Fermilab Report Fermilab-Conf-90-151, 1990.
- [12] R. Wigmans, Calorimetry—Energy Measurement in Particle Physics, International Series of Monographs on Physics, Vol. 107, Oxford University Press, 2000, p. 433 ff.
- [13] M. Hoyer, et al., Nucl. Instr. and Meth. 151 (1978) 69; T. Åkeson, et al., Nucl. Instr. and Meth. A 241 (1985) 17; G. d’Agostini, et al., Nucl. Instr. and Meth. A 274 (1989) 134; E. Bernardi, et al., Nucl. Instr. and Meth. A 262 (1987) 229; D. Acosta, et al., Nucl. Instr. and Meth. A 308 (1991) 481.
- [14] T. Suzuki, et al., Nucl. Instr. and Meth. A 432 (1999) 48.

APPENDIX C
ON THE ENERGY MEASUREMENT OF HADRON JETS (ACCEPTED FOR
PUBLICATION IN NUCLEAR INSTRUMENTS AND METHODS A)



ELSEVIER

Available online at www.sciencedirect.com



Nuclear Instruments and Methods in Physics Research A 495 (2002) 107–120

**NUCLEAR
INSTRUMENTS
& METHODS
IN PHYSICS
RESEARCH**
Section A

www.elsevier.com/locate/nucinst

On the energy measurement of hadron jets

Olga Lobban, Aravindhan Sriharan, Richard Wigmans*

Department of Physics, Texas TECH University, Box 81051, Lubbock, TX 79409-1051, USA

Received 15 July 2002; received in revised form 25 August 2002; accepted 29 August 2002

Abstract

The elementary constituents of hadronic matter (quarks, anti-quarks, gluons) manifest themselves experimentally in the form of jets of particles. We investigate the precision with which the energy of these fragmenting objects can be measured. The relative importance of the instrumental measurement precision and of the jet algorithm is assessed. We also evaluate the “energy flow” method, in which the information from a charged-particle tracker is combined with that from a calorimeter in order to improve the jet energy resolution.

© 2002 Published by Elsevier Science B.V.

PACS: 02.30.Gg, 29.40.Vj

Keywords: Calorimetry; Fluctuations; Jets; Energy flow

1. Introduction

Matter as we know it consists of leptons and quarks. Whereas the properties of leptons such as electrons or muons can usually be measured with a very high degree of precision, the same is not true for quarks. Quarks are “locked up” inside mesons or (anti-)baryons and any attempt to isolate them creates more such particles. In high-energy scattering experiments aimed at studying their properties, quarks, diquarks or anti-quarks fragment into *jets* of hadrons.

The precision with which the properties of the fragmenting object can be measured depends on two factors: The jet-defining algorithm and the

detector quality. Usually, a jet is defined as the collection of particles that fall within a cone with opening angle R emerging from the interaction vertex. Typical values of R , when expressed in terms of an interval in η, ϕ space ($R = \sqrt{\Delta\eta^2 + \Delta\phi^2}$), range from 0.3 to 0.7. If the chosen R value is large, the cone may be contaminated with particles that have nothing to do with the fragmenting object, if R is small, some jet fragments may be located outside the cone. Fluctuations in the jet energy contained within the jet-defining cone form an irreducible component of the jet energy resolution.

At energies below 100 GeV, the contributions of this irreducible component are substantial and in practical experiments they are the main factor limiting the jet energy resolution. However, at higher energies, jets become more and more collimated and the effects of the jet algorithm on

*Corresponding author. Tel.: +1-806-742-3779; fax: +1-806-742-1132.

E-mail address: wigmans@ttu.edu (R. Wigmans).

the energy resolution diminish correspondingly. In Section 2 of this paper, we investigate the energy dependence of these effects.

One of the problems in designing calorimeter systems for modern experiments is the fact that the requirements for excellent energy resolution for single hadrons and jets are orthogonal to those for high-resolution electromagnetic (em) calorimetry [1]. High-resolution hadronic shower measurements require compensating calorimeters. And compensation (i.e. equal calorimeter response to the em and non-em components of hadron showers, $e/h = 1.0$) is only achieved in sampling calorimeters with a very small sampling fraction, e.g. 2.3% in lead plastic-scintillator structures. On the other hand, high-resolution em shower detection requires an instrument with a large sampling fraction, e.g. 100% in crystals or $> 40\%$ in detectors such as the NA48 LKr calorimeter [2].

In order to solve this dilemma, it has been proposed that one could significantly improve the performance of a poor-resolution hadronic calorimeter system by combining its information with that of an upstream tracker system. In this approach, sometimes referred to as the *Energy Flow Method*, the momenta of the charged jet fragments measured with high precision by the tracker serve as a first-order estimate of the jet energy. Second-order corrections, intended to account for the neutral jet component, are derived from the calorimeter signals. Of course, the contributions of showering charged particles to the calorimeter signals have to be discounted properly for this method to work. Methods of this type have been successfully used to improve the resolution of jets from Z -decay at LEP [3]. In Section 3 of this paper, we investigate the prospects of such methods at higher energies. Concluding remarks are given in Section 4.

2. Effects of the jet algorithm

We have studied the effect of a jet-defining algorithm on the energy resolution for fragmenting quarks with a Monte Carlo program that we developed for this purpose. This Monte Carlo program is based on a highly simplified

representation of the physics processes taking place in practice. However, it does contain the essential elements necessary to evaluate the energy dependence of the contributions of the jet algorithm to the resolution. In our program, the fragmentation process is governed by a fragmentation function

$$D(z) = (z-1) \frac{(1-z)^2}{z} \quad (1)$$

in which $D(z)$ denotes the probability that a jet fragment carries a fraction z of the energy of the fragmenting object [4]. The parameter z can be chosen as desired. It has been demonstrated that a function of this type gives a reasonable description of the fragmentation processes measured at LEP and at the Tevatron, for parameter values $z = 3$ and 6, respectively [5].

In our Monte Carlo program, jet fragments are generated with energies zE_{jet} , with the values of z chosen from a distribution representing Eq. (1). Each fragment is assigned a mass m , a charge and a transverse momentum p_{\perp} . Ten percent of the particles are assumed to be kaons and ninety percent pions. One-third of the particles are electrically neutral, the rest are charged. The transverse momentum is chosen from an exponentially falling distribution with a mean value of 0.3 GeV/ c . If the chosen parameters yield an unphysical result, e.g. if the chosen mass is larger than the fragment's energy zE_{jet} , or if the transverse momentum is larger than the total momentum $\sqrt{(zE_{jet})^2 - m^2}$, the fragment is discarded and a new one is selected. The selection of jet fragments is continued until the jet energy is exceeded. In that case, the energy of the last fragment is reduced so that the total energy of all fragments combined equals the jet energy.

We used this program to generate jets with fixed energies, ranging from 10 to 1000 GeV. For each energy, 10 000 jets were generated for two different values of the fragmentation function parameter: $z = 3$ and $z = 6$. First, we show some general results that give an impression of the characteristics of the generated jets. Fig. 1 shows the energy distribution for the particles that constitute a 100 GeV jet, fragmenting according to $z = 3$ or $z = 6$. In Fig. 2, the distribution of the jet

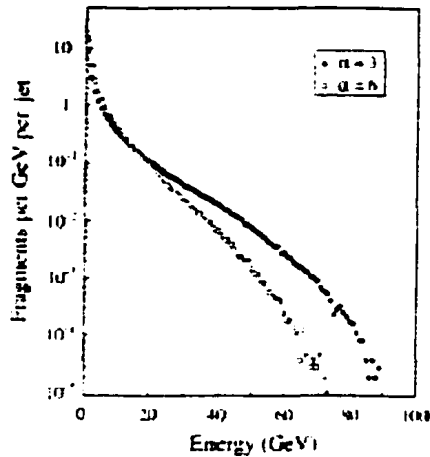


Fig. 1. Energy distribution of particles generated in the fragmentation of a 100 GeV jet according to Eq. (1), with $\alpha = 3$ and 6, respectively.

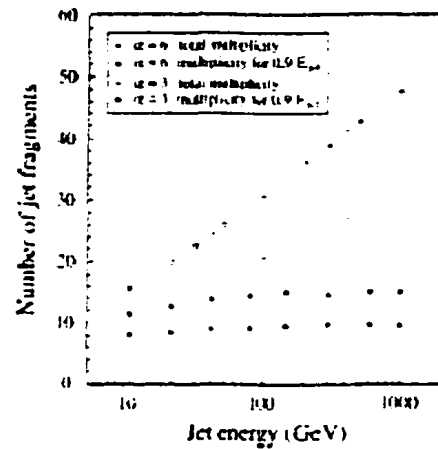


Fig. 3. The average fragment multiplicity and the average number of fragments that account for 90% of the jet's energy as a function of the jet energy, for two different values of the fragmentation function parameter α .

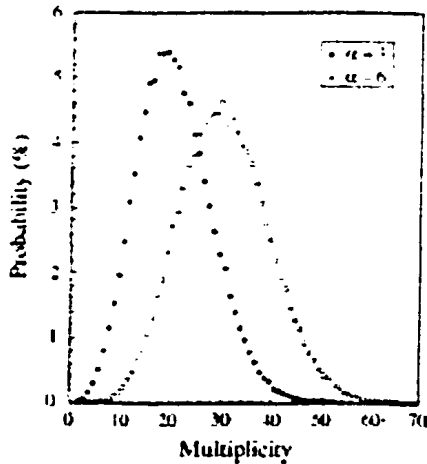


Fig. 2. Multiplicity distribution of fragments from 100 GeV jets, fragmenting according to Eq. (1), with $\alpha = 3$ and $\alpha = 6$, respectively.

fragment multiplicity is given for 100 GeV jets and the average multiplicity is shown as a function of the jet energy in Fig. 3.

In spite of the large numbers of particles constituting the jets, only relatively few particles contribute substantially to the total energy. This is also shown in Fig. 3. For example, in

$\alpha = 3$ jets the 10 most energetic particles carry 90% of the total jet energy. For $\alpha = 6$ jets, that takes 15 particles, on average. This is true at all energies, which is of course a direct consequence of the very concept of a fragmentation function that depends only on z .

We defined the cone parameter R that formed the basis of the applied jet algorithm as

$$R = \sqrt{(\Delta\phi)^2 + (\Delta\eta)^2} \quad (2)$$

where $\Delta\phi$ and $\Delta\eta$ denote the spread around the nominal direction of the fragmenting object in the azimuthal and polar angles, respectively. The fate of a jet fragment was decided on the basis of the ratio of its transverse and longitudinal momenta, p_\perp/p_\parallel . If

$$\arctan(p_\perp/p_\parallel) > R/2$$

then the fragment fell outside the cone, otherwise it was considered to contribute to the measured jet characteristics (energy, momentum, composition). We thus implicitly ignored the effects of an eventual magnetic field, which has the tendency to sweep soft charged particles out of the cone. Therefore, the results to be presented are

somewhat too optimistic, especially for low jet energies. At the high energies which are the focus of our study, jet fragments that are susceptible to the sweeping effects of a magnetic field represent only a small fraction of the total jet energy. The effects of a magnetic field are discussed in more detail in the context of the Energy Flow Method, in Section 3.3.

Fig. 4 shows the average fraction of the jet energy that was found to be contained in a jet-defining cone, as a function of the jet energy. We used two different cone sizes, $R = 0.3$ and 0.5 , respectively. We also used two fragmentation functions which differed in the value for the parameter α , as before: $\alpha = 3$ and $\alpha = 6$. The error bars on the data points in Fig. 4 indicate the spread in the jet containment resulting from this degree of freedom.

These data show that for jets of about 20 GeV, on average some 30% of the energy was carried by fragments that travelled outside the cone. However, as the jet energy increases, the containment rapidly improves. For energies above 100 GeV, typically less than 10% of the energy is unaccounted for when the chosen jet algorithms are applied.

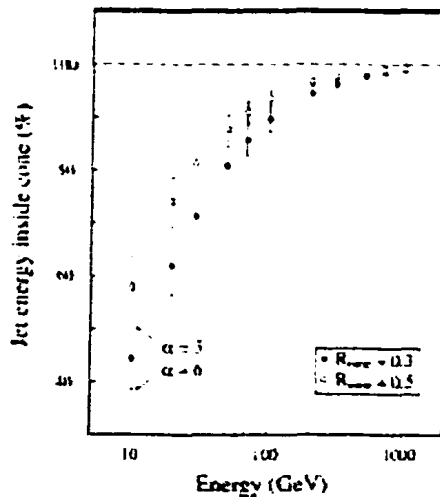


Fig. 4. The average fraction of the jet energy contained in the jet-defining cone as a function of the jet energy. Results are given for cones with $R = 0.3$ and $R = 0.5$. The error bars indicate the spread in the results caused by the choice of the value of the fragmentation function parameter α .

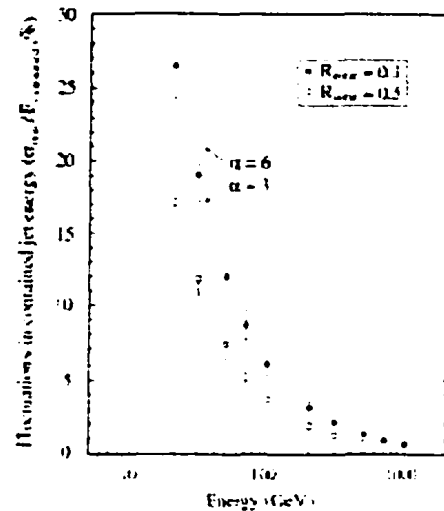


Fig. 5. The contribution of fluctuations in the total energy carried by particles escaping the jet-defining cone to the jet energy resolution, as a function of the jet energy. Results are given for cones with $R = 0.3$ and $R = 0.5$. The error bars indicate the spread in the results caused by the choice of the value of the fragmentation function parameter α .

The energy resolution caused by *fluctuations* in the energy carried by particles travelling outside the cone is shown in Fig. 5. For jet energies of 45 GeV, as found in the decay of Z^0 bosons produced at the e^+e^- collider LEP, the contribution to the energy resolution from jet algorithms such as those discussed here amounts to $\sim 10\%$. Therefore, there was no compelling reason to install detectors measuring hadrons with a precision better than that in the LEP experiments. However, as the energy increases, the situation changes. The jets become more and more collimated and, as a result, fluctuations in the energy contained inside the jet-defining cone are reduced. For jets of 500 GeV and higher, the contribution of the jet algorithm to the jet energy resolution is of the order of 1%, smaller than the instrumental energy resolution achieved with any hadron calorimeter that has ever been tested. Therefore, a high-resolution hadron calorimeter would in practice make a crucial difference for the precision with which high-energy jets can be measured.

This is illustrated in Fig. 6, which shows the contribution from the “irreducible” fluctuations for a cone with $R = 0.3$ as a function of the jet energy, which is plotted here on a scale linear in $E^{-1.2}$ (the solid curve). For comparison, the measured hadronic energy resolutions are given for two experiments at the future LHC at CERN (ATLAS [6] and CMS [7]) and for the SPACAL calorimeter [8], which currently holds the world record in terms of hadronic energy resolution. The latter calorimeter would represent a significant advantage (compared to the LHC ones) for the detection of jets with energies above 100 GeV, but at lower energies the quality of the measurements is dominated by the jet algorithm.

It should be emphasized that in this analysis we have deliberately ignored the effects of particles that do not belong to the fragmenting object but migrate into the jet-defining cone. Of course, these effects tend to extend the importance of the contributions of the jet algorithm to the jet energy resolution. They are extremely dependent on the type of experiment (e^+e^- or pp colliders, fixed target experiments) and also on factors such as the luminosity and the kinematic region under study.

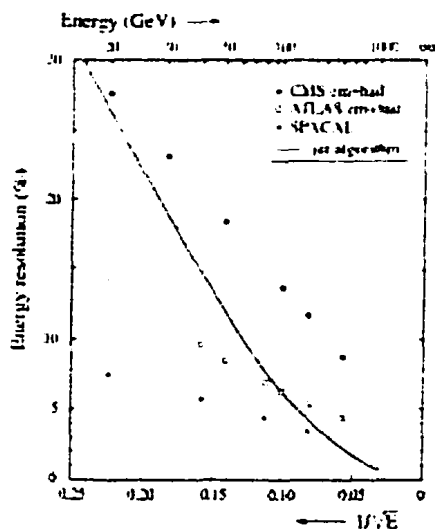


Fig. 6. The hadronic energy resolution of three calorimeter systems and the contribution of a jet-defining cone with $R = 0.3$ to the jet energy resolution, as a function of energy.

These underlying event effects are largest in the high- η regions of high-luminosity pp collider experiments, such as those planned for the future LHC at CERN, where every interesting event is accompanied by ~ 25 other events taking place in the same bunch crossing. On the other hand, in high-energy e^+e^- colliders disturbances of this type are not very important. The conclusions derived from Fig. 6 are thus primarily valid for the latter type of experiments.

3. The energy flow method

3.1. The basic idea

In the previous section, we have shown that as the high-energy frontier of particle physics is pushed to higher and higher values, high-resolution measurements of fragmenting hadronic constituents such as quarks, anti-quarks, diquarks and gluons becomes increasingly possible, since the limitations imposed by jet-defining algorithms become less of an issue. Therefore, the intrinsic qualities of the instruments with which the jet energies are being measured become the determining factor in this respect.

The techniques that have been used until now in calorimetry make high-resolution em and hadron shower detection mutually exclusive propositions [1]. High-resolution hadronic shower measurements require compensating calorimeters. And compensation (i.e. equal calorimeter response to the em and non-em components of hadron showers, $e/h = 1.0$) is only achieved in sampling calorimeters with a very small sampling fraction, e.g., 2.3% in lead-plastic-scintillator structures. On the other hand, high-resolution em shower detection requires an instrument with a very large sampling fraction. The ZEUS Collaboration, which currently operates the highest-resolution hadron calorimeter in the world [9], pays a price for that in the form of a rather mediocre performance for em shower detection: $\sigma/E = 18\%/\sqrt{E}$. Calorimeters such as the ones that will be used in the LHC experiments emphasize excellent electromagnetic resolution, at the expense of hadronic resolution, as is illustrated in Fig. 6.

In future experiments, e.g., at a proposed linear e^+e^- collider in the 0.5–1 TeV range, which was recently defined as the most desirable future machine for particle physics research [10], one will want to be able to measure *all* constituents of matter with resolutions at the 1% level. The question is how that can be achieved.

One of the solutions pursued in this context involves the so-called *Energy Flow Method* (EFM), in which the information from the calorimeter system is combined with that from an upstream tracker system. The momenta of the charged jet fragments, measured with high precision by the magnetic tracking system, serve as a first-order estimate of the jet energy. The calorimeter signals are used to obtain second-order corrections to that energy, caused by the neutral jet component (γ s, K^0 s and neutrons). With methods of this type, several LEP experiments improved the resolution of jets from Z -decay from $\sim 12\%$ to $\sim 9\%$. We have studied the merits of such methods, and in particular the energy dependence of these merits, with the same Monte Carlo program that was used to investigate the contributions of jet algorithms to the jet energy resolution (Section 2).

3.2. No calorimeter

The Energy Flow Method exploits the fact that the charged fragments of jets can be measured much more precisely with a tracker than with a

calorimeter. However, the calorimeter information is still needed to account for the contributions of neutral particles, mainly γ s from π^0 decay, but also K^0 s and neutrons. In the absence of calorimeter information, based on tracker information alone, the jet resolution would be determined by the fluctuations in the fraction of the total jet energy that is carried by the charged fragments. Table 1 lists these fluctuations for jet energies ranging from 10 GeV to 1 TeV, for simulated jets with $z = 3$ and $z = 6$, respectively.

The average energy carried by the charged jet fragments is $\frac{1}{z}$ of the jet energy. However, the event-to-event fluctuations are large, the σ_{rms} amounts to 30% of the average value for $z = 3$ jets and 24% for $z = 6$, independent of the jet energy. One may wonder why these fluctuations do not become smaller at higher energies, given the fact that the number of jet fragments increases. The reason for this is that the observed increase in multiplicity is uniquely caused by the addition of more *soft* particles. The bulk of the jet energy is invariably carried by a small number of the most energetic particles (cf. Fig. 3). This means that the fraction of the jet energy carried by charged particles is strongly dependent on the extent to which these particles participate in the “leading” component of the jet. Therefore, the event-to-event fluctuations in this fraction are large and do *not* significantly improve with energy.

Table 1

The total energy carried by the charged fragments of jets and the fluctuations in this energy ($\sigma_{\text{rms}}/E_{\text{charged}}$) are listed for jet energies ranging from 10–1000 GeV. Results are given for two different values of the fragmentation function parameter z .

| Jet energy (GeV) | $z = 3$ | | $z = 6$ | |
|------------------|-------------------|------------------|-------------------|------------------|
| | Charged fragments | Fluctuations (%) | Charged fragments | Fluctuations (%) |
| 10 | 6.33 \pm 2.66 | 30.1 | 6.23 \pm 1.68 | 24.1 |
| 20 | 13.2 \pm 4.13 | 33.6 | 13.0 \pm 3.27 | 24.2 |
| 30 | 19.3 \pm 6.13 | 32.6 | 20.2 \pm 4.89 | 24.2 |
| 40 | 26.5 \pm 8.10 | 30.6 | 28.9 \pm 6.46 | 24.0 |
| 50 | 33.4 \pm 10.0 | 30.0 | 33.5 \pm 8.10 | 24.2 |
| 100 | 66.6 \pm 19.9 | 30.4 | 66.6 \pm 16.3 | 24.4 |
| 200 | 133 \pm 40.1 | 30.2 | 133 \pm 32.0 | 24.1 |
| 300 | 200 \pm 59.8 | 29.9 | 200 \pm 48.4 | 24.2 |
| 400 | 266 \pm 80.4 | 30.3 | 266 \pm 64.2 | 24.2 |
| 500 | 332 \pm 99.9 | 30.1 | 332 \pm 80.5 | 24.2 |
| 1000 | 663 \pm 201 | 30.3 | 665 \pm 160 | 23.1 |

As an aside, we mention that the same thus necessarily applies for the event-to-event fluctuations in the fraction of electromagnetically interacting particles (mainly π^0 's). These fluctuations are responsible for the poor jet energy resolution of non-compensating calorimeters, especially at high energy [1], since the response of such calorimeters is usually considerably larger for em showers than for non-em ones.

In the absence of a calorimeter, one should therefore not expect to be able to measure jet energy resolutions better than 25–30% on the basis of tracker information alone, at any energy. And since the contributions of showering charged particles to the calorimeter signals have to be discounted properly for the EFM to work, the quality of the calorimeter information is in practice important.

3.3. Magnetic field effects

The proponents of this method claim that the key to its success in a Linear-Collider experiment is determined by the *granularity* of the detector. A high granularity would make it possible to recognize and eliminate all contributions of the charged particles to the overall calorimeter signal. The remaining calorimeter signal could then be attributed to the neutral jet components [11].

However, the question arises whether the jet fragments, by the time they reach the front face of the calorimeter, are sufficiently separated from each other in order to individually recognize their showers. The lateral development of the showers is governed by the Molière radius (ρ_M) for the fragments that develop em showers and by the nuclear interaction length (λ_{int}) for the fragments that develop hadronic showers. If there is significant overlap between the showers initiated by the various jet fragments, then even the finest detector granularity would not make it possible to disentangle the different shower profiles.

The problem one faces may be illustrated with Fig. 7, which shows an event display of the SPACAL calorimeter [12]. A beam of pions was sent onto a thin target placed 1.5 m upstream of the calorimeter. Interacting pions were selected and the reaction products were recorded in the calorimeter. SPACAL was a fine-grained calorimeter, the effective radius of each readout cell was $0.19\lambda_{int}$ ($2.0\rho_M$). Readout cells of hadron calorimeters used in most experiments are typically 20–30 times larger. The figure shows several individual reaction products that can be clearly distinguished. However, there is also considerable overlap between the showers initiated by these particles. Making the granularity smaller would not help to resolve the energy deposit pattern.

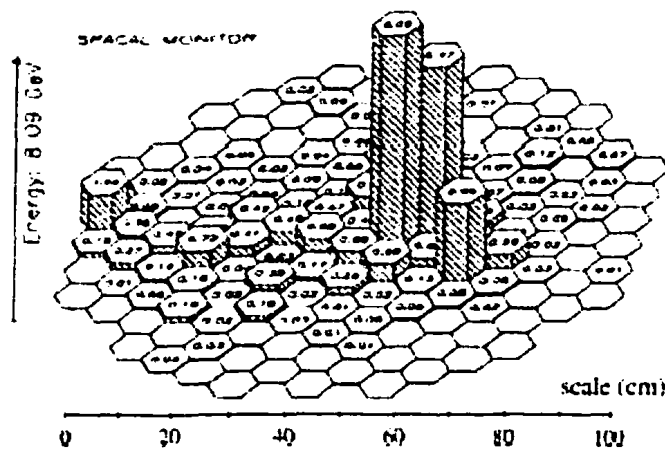


Fig. 7. A SPACAL event display of the reaction products from a pion interaction in an upstream target. The numbers denote the energy (in GeV) deposited in the individual calorimeter cells [12].

since the cell size is such that even electromagnetic showers usually ended up sharing their energy among several cells in this detector.

The question whether or not the jet fragments are sufficiently separated is mainly determined by two factors:

- (1) The distance between the calorimeter's front face and the beam line, where the fragmentation takes place, and
- (2) The strength of the magnetic field that is used to separate the charged jet fragments from each other.

In addition, the jet energy and the type of jet (fragmenting quark, diquark or gluon) may play a role. We investigated this issue for the proposed TESLA experiment [13], which is equipped with a 4 T magnetic field, while the calorimeter front face is located at a distance of 1.68 m from the beam line.

According to Fig. 3, a particle produced in the fragmentation of a 100 GeV quark carries typically 9 GeV (90%) of the energy is carried by the 10

most energetic particles). If this particle is electrically charged, it will deviate from a straight path by 19 cm before reaching the TESLA calorimeter, as a result of this magnetic field. That is 3 times as much as the *average* deviation from the jet axis resulting from the intrinsic transverse momentum of the jet fragment.

For the softer jet fragments, the effect of the magnetic field, compared to that of the intrinsic p_{\perp} , increases further. For example, a 3 GeV/c π^{-} travelling in a plane perpendicular to the magnetic field will deviate by 65 cm from its original direction upon arrival at the calorimeter's front face, 4 times as much as the effect of the intrinsic p_{\perp} . And pions with a momentum < 2 GeV/c will not reach the calorimeter at all.

An example of an event in which the LFM might work as anticipated is shown in Fig. 3. This is an event with a leading π^0 meson. The charged fragments are bent away by the magnetic field, to such an extent that their showers do not interfere with the (most energetic) photon ones. The circles indicate the characteristic size of the showers

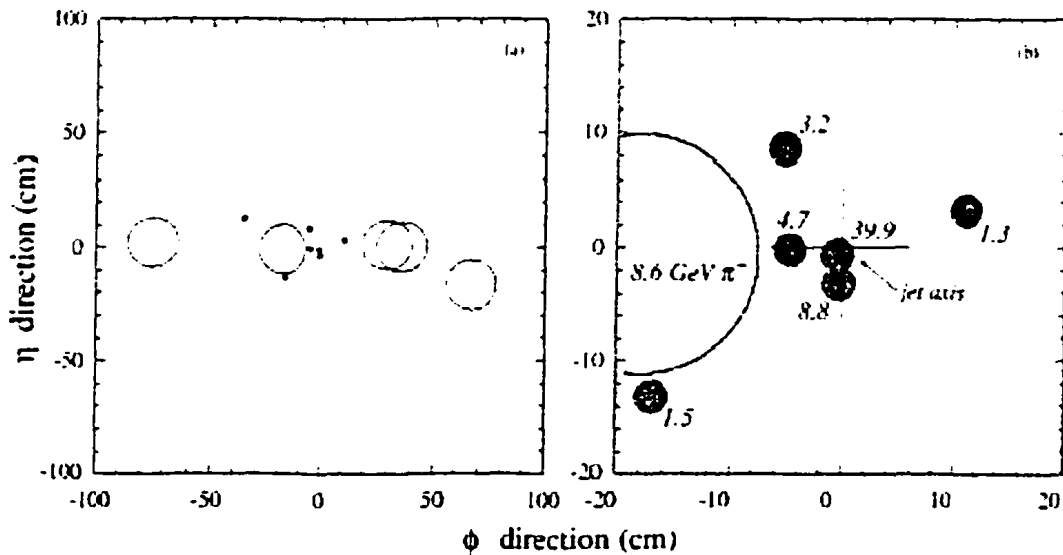


Fig. 3. Fragmentation of a 100 GeV quark jet with a leading π^- in the calorimeter of the TESLA experiment. The circles indicate the characteristic lateral dimensions of the showers developed by the fragments, and the numbers represent the energies of the fragments, in GeV. The point (0,0) corresponds to the direction of the fragmenting quark. See text for more details.

initiated by the jet fragments, i.e. ρ_M for em showers, λ_{int} for hadronic ones. We have assumed a calorimeter with the highest possible density, i.e. with the smallest possible values of ρ_M and λ_{int} , 1 and 10 cm, respectively. The showers from hadronic fragments are indicated by open circles, the electromagnetic ones are represented by the shaded circles. The energies of the fragments (in GeV) are indicated in the figure. Only particles carrying more than 1 GeV are shown in this display, which concerns a jet at $\eta = 0$ (perpendicular to the beam line). Quarks travelling in other directions will develop jets that are somewhat broader in the η direction. Fig. 8b shows a close-up of the central 40×40 cm² area surrounding the (0,0) point, which represents the jet axis.

However, the problems with this method arise for jets with energetic charged jet fragments. Compared to soft charged fragments, the effect of the magnetic field on these particles is small and, therefore, they enter the calorimeter in the same region where also the (γ s from) π^0 s deposit most of their energy. The most energetic particle in our 100 GeV quark jet carries, on average, 29 GeV. If it is charged, it reaches the calorimeter's front face at a distance of 6 cm from its straight-line-extrapolated original momentum vector. The distance between the impact point and the jet axis is, on average, 7 cm.

Fig. 9 shows 4 examples of events which pose serious problems for the EFM. In all cases, one or several energetic em showers fall within the region covered by showers generated by electrically charged jet fragments. One might argue that the longitudinal shower development of these two types of jet fragments is very different and that one could use this information to disentangle the energy deposit profiles. However, it is important to keep in mind that hadron showers typically deposit one third to one half of their energy in the first nuclear interaction length, which constitutes usually the electromagnetic calorimeter section of the detector. It is, therefore, very likely that it is impossible to disentangle the detector hit patterns for events of this type into contributions from the charged jet fragments and from the other components. It should be emphasized that the depicted events were not specially selected to illustrate this

point, 70% of all high-energy jet events resemble those shown in Fig. 9, which were taken from the sample of the first 10 events generated in our Monte Carlo simulations.

3.4. Importance of the calorimeter quality

For reasons described in the previous subsection, the calorimeter system needs other qualities besides a high granularity. In particular, it needs a good hadron energy resolution in order to measure jet energies with good precision. This resolution will determine how well one can determine the contribution of the precisely measured charged jet fragments to the total calorimeter signal and, therefore, the precision of the neutral energy obtained after subtracting this contribution.

3.4.1. Monte Carlo simulations

In order to quantify the above statements, we have studied the merits of the EFM for a calorimeter system with a hadronic energy resolution $\sigma/E = 70\%/\sqrt{E} - 5\%$ and an e/h value of 1.5. These parameters are typical for the calorimeters that were used in the LEP experiments. The jet resolution that could be expected on the basis of the Energy Flow Method applied to such a calorimeter system was evaluated in the following way.

We distinguish three types of jet fragments:

- Particles that develop em showers in the calorimeter (mainly γ s from z^0 decay)
- Soft hadrons that do not interfere with the calorimetric jet measurements as a result of the magnetic field. This field either prevents them from reaching the calorimeter at all or bends them to such an extent that they end up outside the jet-defining cone.
- Hadrons that do contribute to the calorimetric jet signals.

If the jet consisted only of particles of types (a) and (b), then the EFM would be a perfect tool to determine its energy. It would be no problem at all to get sub-1% energy resolutions for jets with energies in excess of 100 GeV. However, the contributions of these particles to a realistic jet resolution may, for all practical purposes, be

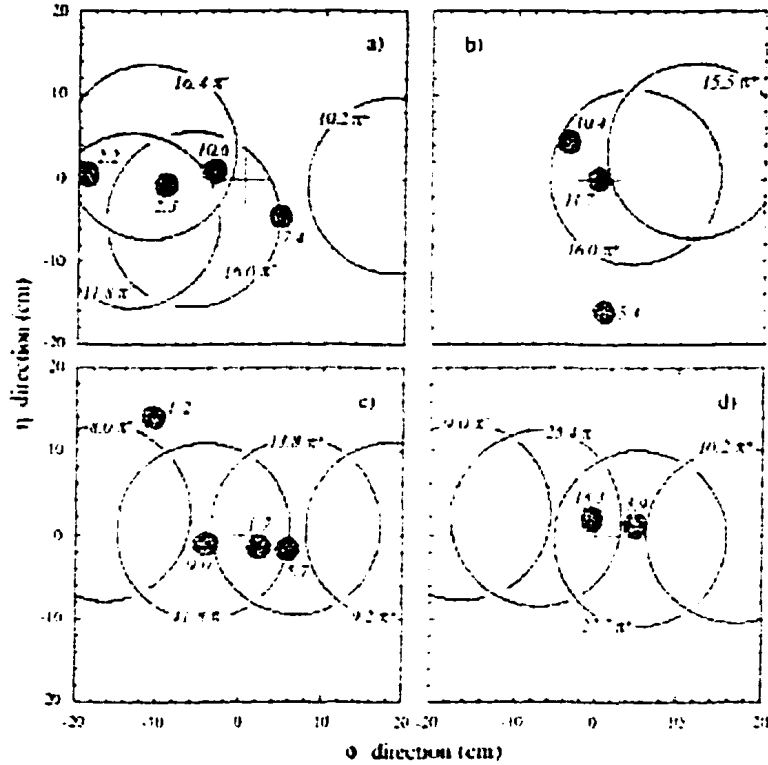


Fig. 9. Four examples of 100 GeV quark jets with energetic charged fragments, detected in the calorimeter of the TESLA experiment. The circles indicate the characteristic lateral dimensions of the showers developed by the fragments, and the numbers represent the energies of the fragments, in GeV. The point (0,0) corresponds to the direction of the fragmenting quark. Only showers initiated by particles carrying at least 1 GeV and developing in the region of $20 \times 20 \text{ cm}^2$ surrounding the jet axis are depicted. See text for more details.

considered negligible. This resolution will be completely determined by the particles of type (c) and, more in particular, by the fluctuations in the signals they generate in the calorimeter. Therefore, in our Monte Carlo simulations, we determined the "EFM" signal for a given jet by smearing the energies from the fragments of type (c) with the hadronic calorimeter resolution and adding to these the exact energies of the particles of type (a) and (b).

Jet fragments were selected as before according to a fragmentation function of type (1). The distinction between hadrons of types (b) and (c) was made on the basis of the momentum of the

particles. Usually, we considered hadrons with momenta $< 1 \text{ GeV}/c$ particles of type (b), and the rest particles of type (c), but we also varied this threshold to study its effect. For each hadron of type (c), we drew a random entry (E_c) from a Gaussian distribution with a central value given by the fragment's energy (E_c) and a width given by the resolution function, e.g., $\sigma = 2.7 \text{ GeV}$ for a 10 GeV hadronic fragment. Then, the contribution of this fragment to the calorimeter signal was determined taking into account the effect of the e/h value. The em shower fraction was taken to be $f_{em} = 1 - E_c^{-0.18}$ and the signal was calculated as $S_c = E_c [f_{em} - (1 - f_{em})h/e]$ [1]. The total "EFM"

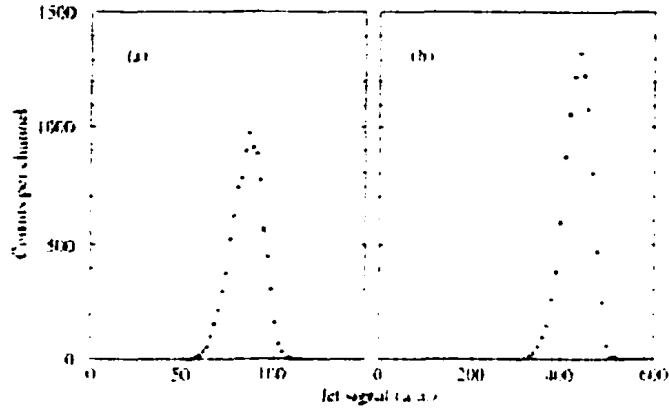


Fig. 10. Signal distributions for 100 GeV (a) and 500 GeV (b) jets in a LEP detector, after application of the Energy Flow Method. Results of simulations described in detail in the text.

signal was found by summing over all fragments, as follows.

$$S_{jet} = \sum_{i=1}^n E_i - E_0 - S_c \quad (13)$$

Examples of the resulting signal distributions are shown in Fig. 10. For $n = 6$ jets, the resolution was found to be 9.3% at 100 GeV and 6.6% at 500 GeV. Compared to the resolution that may be expected from the calorimeter system alone, this represents a relative improvement of 23% and 19%, respectively.

We have studied the effects of the EFM over a wide range of energies. We also varied the parameter that defines the jet type (n), as well as the momentum threshold for the distinction between hadrons of types (b) and (c) (p_{bc}). The results are summarized in Figs. 11 and 12.

Fig. 11 shows the calorimetric jet resolution of the generic LEP detector (the dashed line), as well as the jet resolution one might expect when applying the EFM to jets measured with this detector, assuming the momenta of the charged jet fragment are precisely known. The results are shown as a function of the jet energy. At low energies, the EFM is seen to improve the jet resolution by ~35%. As the energy increases, the relative improvement slowly decreases, to ~18% at 1000 GeV. The main reason for this is the fact

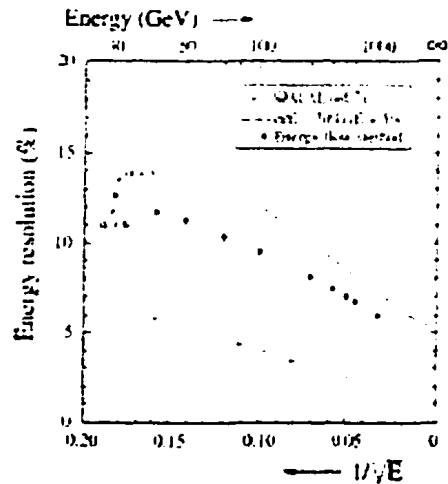


Fig. 11. The jet energy resolution as a function of energy, obtained after applying the Energy Flow Method (the black dots), using simulated data from a calorimeter with a jet resolution given by the dashed curve. For comparison, the jet resolution of a compensating calorimeter is given (SPACAL [8], the dotted curve).

that the jets become increasingly collimated at higher energies, the slow hadronic fragments that are swept away by the magnetic field represent a decreasing fraction of the jet energy. This may also be illustrated by the fact that the relative resolution improvement achieved with the EFM

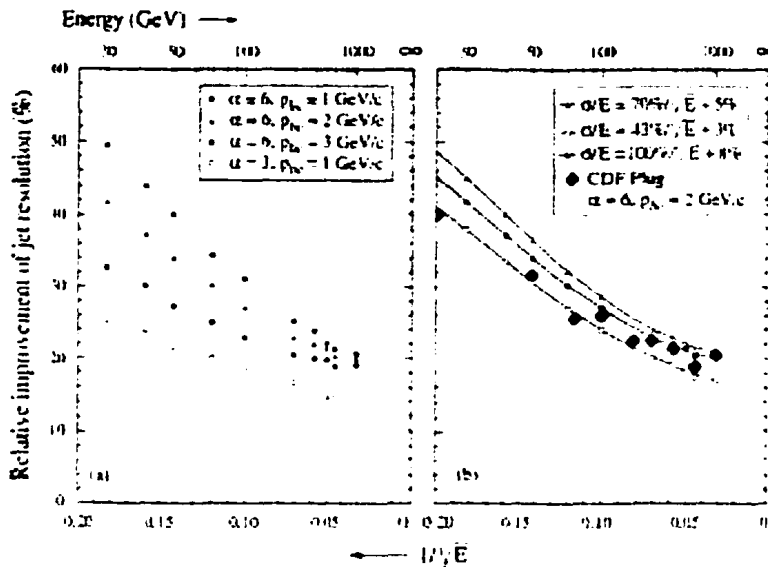


Fig. 12. Relative improvement of the jet resolution by using the Energy Flow Method, as a function of the jet energy. Results of Monte Carlo simulations with different parameter choices. The black diamonds were obtained using testbeam data from the CDF Plug Upgrade calorimeter. See text for details.

increased with the momentum threshold p_{th} , and with the value of α ($\alpha = 6$ jets contain more soft particles than $\alpha = 3$ ones). The error bars in Fig. 11 indicate the effect of the choice of the α parameter on the results, and p_{th} was $1 \text{ GeV}/c$ in these simulations.

Fig. 12 shows how the improvement of the energy resolution that can be achieved with a tracker that measures the momenta of the charged jet fragments depends on the various parameters used in the simulations. This improvement clearly benefits from a stronger magnetic field, which is equivalent to a larger value of p_{th} (Fig. 12a). The benefits of the EFM also have a tendency to decrease when a better calorimeter system is used. We concluded this from simulations, in which we replaced the calorimeter by one with a hadronic resolution of $43\%/ \sqrt{E} + 3\%$ and $e/h = 1.3$. On the other hand, they increase when a more inferior calorimeter system is used. We checked that by simulating a calorimeter with a hadronic resolution of $100\%/ \sqrt{E} + 8\%$ and $e/h = 2.0$. These tendencies can be understood by considering

the extreme cases: For a perfect calorimeter, there is nothing left for a tracker to improve upon, while for no calorimeter at all, the tracker still gives a 30% resolution for the jets (Section 3.2). However, as can be seen from Fig. 12b, for the three systems we simulated the differences are relatively small.

3.4.2. Experimental data

In order not to rely exclusively on Monte Carlo simulations, we also analyzed some testbeam data taken with the CDF Plug Upgrade calorimeter [14]. This calorimeter consists of two sections, which we will label EM and HAD. We used these data to build "libraries" of jet signal distributions for jets of a variety of energies, ranging from 30–1000 GeV. This was done as follows [15].

Jet fragments were selected as before according to a fragmentation function of type (1) with $\alpha = 6$, which is favored by the CDF data. For each jet fragment, we used the measured signal distribution for testbeam pions or electrons of the nearest energy in order to determine what the calorimeter

signal would have been had that fragment actually deposited its energy in the calorimeter.

For each jet fragment i with energy E_i , we randomly pulled an EM signal, S_i^{em} , and a HAD signal, S_i^{had} , from the corresponding signal distributions for a testbeam run of electrons (if the fragment was neutral) or pions (if the fragment was charged) whose energy was closest to the energy carried by the jet fragment. For instance, for a 10 GeV charged jet fragment, we used the experimental signal distributions for an 8.6 GeV pion testbeam run for that purpose. This jet fragment was then attributed an EM signal $S_i^{\text{em}} = (10/8.6)S_i^{\text{em}}$ and a HAD signal $S_i^{\text{had}} = (10/8.6)S_i^{\text{had}}$, respectively. For a 10 GeV neutral fragment, the same procedure would be followed, but the signals would be taken from an electron run rather than a pion run. Charged hadrons with energies below 2 GeV were assumed not to reach the calorimeter and, therefore, they did not contribute to the calorimeter signals.

The described process was repeated for each of the n fragments that made up the jet of energy E_{jet} . The energy the calorimeter would have reconstructed for this particular jet then is simply

$$S_{\text{jet}} = \sum_{i=1}^n \left[\frac{S_i^{\text{em}}}{A} + \frac{S_i^{\text{had}}}{B} \right] \quad (4)$$

where A and B denote the calibration constants used to convert the signals from the EM and HAD calorimeter sections into energies. Such S_{jet} signal libraries were generated for each of the chosen jet energies.

For a given jet of a certain fixed energy, e.g., 100 GeV, the experimental pion signal distributions were used to determine the calorimeter signals S_i^{em} and S_i^{had} (in the EM and HAD sections) for individual charged jet fragments i , following the same procedure. These signals were also converted into energy units using the calibration constants A and B . The total calorimeter signal from the m charged components of a given 100 GeV jet was thus found as

$$E_{\text{charged}} = \sum_{i=1}^m \left[\frac{S_i^{\text{em}}}{A} + \frac{S_i^{\text{had}}}{B} \right] \quad (5)$$

and the calorimeter signal (or rather its energy equivalent) representing the neutral jet components of our 100 GeV jet (E_{neutral}) was found by subtracting E_{charged} from the average value of the S_{jet} distribution for 100 GeV jets. Finally, the energy found with the EFM for this particular jet was calculated as

$$E_{\text{EFM}} = \sum_{i=1}^m E_i - E_{\text{neutral}} \quad (6)$$

where E_i ($i = 1, 2, \dots, m$) represent the exact energies of the chosen *charged* jet fragments, including the soft ones swept away by the magnetic field.

The relative effect of the EFM on the jet energy resolution was determined by comparing the fractional widths of the S_{jet} and E_{EFM} distributions. The improvement of the jet energy resolution found this way is included in Fig. 12b. The data agree well with the results of our simulations for a calorimeter system with the properties of the CDF one.

Both our simulations and the experimental data show that the EFM does offer a beneficial effect. However, this effect should not be exaggerated. The improvement in the energy resolution is typically 30%. Poor calorimeter systems benefit more than good calorimeter systems, and a strong magnetic field also helps. It is important to note that the EFM does not work as well at high energies as at low energies. Therefore, the 30% improvement in the mass resolution obtained for hadronically decaying Z^0 's at LEP is probably an upper limit for what may be expected from this technique at a high-energy Linear-Collider experiment. At high energies, the hadronic calorimeter resolution is dominated by fluctuations that result from the different calorimeter response to em and non-em energy deposit. These fluctuations are not addressed, nor cured by the EFM.

For comparison, we show in Fig. 11 the jet resolution measured with the SPACAL calorimeter [8]. Thanks to the compensating character of this device, the jet resolution scales very well with $E^{-1/2}$. This feature, combined with the diminishing resolution improvement achieved with the EFM at high energies, is responsible for the much better performance that may be expected in the high-energy region.

4. Conclusions

In this paper, we have studied some of the factors that limit the precision with which the energy of fragmenting quarks may be measured. We found that at energies below ~ 100 GeV, a dominating role is played by the algorithm that is used to identify the components of the fragmenting quark (the jet algorithm). However, at higher energies, the jets are increasingly collimated and the precision with which the quark's properties may be measured is increasingly dominated by the quality of the experimental equipment.

We have shown that the so-called Energy Flow Method, in which the momenta of the charged fragments form the basis of the jet energy measurement, provides a modest improvement of the resolution that can be obtained with stand-alone calorimeter systems. The relative improvement is about 30% for jets from decaying W,Z bosons and decreases at higher energies. Claims that much better results may be achieved for highly granular calorimeter systems, in which the showers generated by the individual jet fragments may be recognized and separated from each other are unsubstantiated. We have shown that for most of the showers in practical detectors, the overlap between the shower profiles rather than the detector granularity is the factor that limits the benefits of this method.

A better solution for high-precision measurements of fragmenting quarks is a high-resolution calorimeter system. Traditional compensating calorimeters, which allow for high-resolution jet measurements, are limited in their electromagnetic resolution. An optimal solution might be a dual-readout calorimeter [16], in which the em shower fraction is measured event-by-event and which does not require the small sampling fraction needed for compensating devices.

Acknowledgements

This study was carried out with financial support of the United States Department of Energy, under contract DE-FG03-95ER40938, and of Texas Tech University's Clark Scholars program.

References

- [1] R. Wigmans, *Calorimetry—energy measurement in particle physics*, in International Series of Monographs on Physics, Vol. 107, Oxford University Press, Oxford, 2000.
- [2] G.D. Barr, et al., Nucl. Instr. and Meth. A 370 (1996) 413.
- [3] D. Buskulic, et al., Nucl. Instr. and Meth. A 360 (1995) 481.
- [4] F. Halzen, A.D. Martin, *Quarks & Leptons*, Wiley, New York, 1984, p. 231.
- [5] D. Green, *Dijet spectroscopy at high luminosity*, Fermilab Report Fermilab-Conf-96-151, 1996.
- [6] S. Akhmadaliev, et al., Nucl. Instr. and Meth. A 449 (2000) 461.
- [7] V.V. Abramo, et al., Nucl. Instr. and Meth. A 457 (2001) 75.
- [8] D. Acosta, et al., Nucl. Instr. and Meth. A 369 (1996) 461.
- [9] G. Drewe, et al., Nucl. Instr. and Meth. A 290 (1990) 335.
- [10] Press release after the 2001 APS Workshop on the Future of Particle Physics, Snowmass, CO, July 21, 2001.
- [11] V.L. Morgunov, *Calorimetry Design with Energy-Flow Concept*, Talk presented at the 10th International Conference on Calorimetry in High Energy Physics, Pasadena, March 25–29, 2002.
- [12] D. Acosta, et al., Nucl. Instr. and Meth. A 305 (1991) 55.
- [13] TESLA Technical Design Report, report DESY 2001-021, DESY, Hamburg, Germany, 2001.
- [14] M. Albrow, et al., Nucl. Instr. and Meth. A 480 (2002) 524.
- [15] M. Albrow, et al., Intercalibration of the longitudinal segments of a calorimeter system, Nucl. Instr. and Meth. A 487 (2002) 381.
- [16] R. Wigmans, *Quartz Fibers and the Prospects for Hadron Calorimetry at the 1% Resolution Level*, Proceedings of the Seventh International Conference on Calorimetry in High Energy Physics, Tucson, 1997, World Scientific, Singapore, 1998, pp. 182–193.